UNIVERSITÀ DEGLI STUDI DI PAVIA
DOTTORATO DI RICERCA IN FISICA – XXVII CICLO

Exploiting Nuclear and Electronic Magnetism Out-of-equilibrium

Filippo Caracciolo

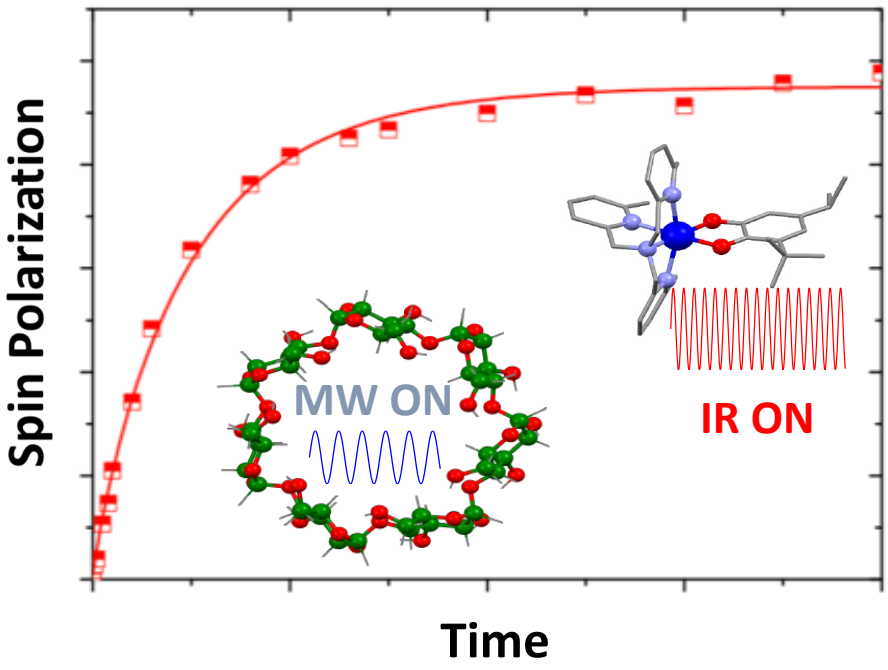

Tesi per il conseguimento del titolo

Exploiting Nuclear and Electronic Magnetism Out-of-equilibrium

Filippo Caracciolo

2018

University of Pavia, Department of Physics
PhD programme in Physics - XXXI cycle
2018

Exploiting Nuclear and Electronic Magnetism Out-of-equilibrium

submitted to the Graduate School of Physics by

Filippo Caracciolo

in partial fulfillment of the requirements for the degree of

Doctor of Philosophy in Physics

supervisor

Prof. Pietro Carretta

Cover. Spin polarization (either nuclear or electronic) as function of time under electromagnetic wave irradiation and two molecules (βCyclodextrin on the left and Valence Tautomer on the right) are depicted.

Exploiting Nuclear and Electronic Magnetism Out-of-equilibrium
Filippo Caracciolo
PhD thesis - University of Pavia
Pavia, Italy, December 2018

Contents

Chapter 1

Introduction

The physics of magnetism plays a key role in many branches of science and technology [1, 2]. Nowadays, a wide range of magnetic phenomena is exploited in many applications, thanks to the fact that magnetism is relevant at different length scales, from the macroscopic magnets [3] to the magnetic nanoparticles [4], from the electronic molecular magnetism [5] to the nuclear magnetism at the atomic level [6, 7]. In particular, the last two sectors are quite relevant for practical applications. For example, nuclear spins are exploited in nuclear magnetic resonance (NMR) as local probes to study the microscopic properties of matter, yielding information useful in many fields, ranging from physics [6, 7] to chemistry [8], pharmacology [9], biology [10], medicine [11], geophysics [12] and food science [13]. On the other hand electronic magnetism has provided for a long time an interesting way to store information through the magnetic memory device, allowing the development of computers and other electronic equipments [3]. The importance of magnetism in real life applications is however hindered by some crucial drawbacks: the nuclear magnetism is quite weak, due to the low value of nuclear gyromagnetic ratio, and consequently this makes NMR a low sensitivity technique; the size of the magnetic memories cannot be reduced beyond a given limit owing to the increased dissipation, preventing such devices to reach nanoscopic sizes. One possible solution to both problems is to combine external light irradiation and magnetism, exploiting the magnetic properties of out-of-equilibrium states. This thesis deals with the understanding and the development of techniques aimed at controlling magnetism using simple electromagnetic wave irradiation in order to extend and to improve real life applications of magnetism.

The first important technique that will be discussed is the dynamic nuclear polarization (DNP), an hyperpolarization technique that has been developed to increase nuclear polarization in order to amplify the NMR signal [14, 15]. Indeed, the NMR signal depends on the polarization nuclei acquire when placed into a magnetic field H_0, that is proportional to the population difference between the nuclear Zeeman levels. For spins $\mathrm{I} = \frac{1}{2}$ this difference is proportional to $\tanh\left[(\hbar\gamma_n H_0) \,/\, (2K_B T)\right]$, where γ_n is the gyromagnetic ratio and T is the

temperature. In typical NMR conditions, for example in a 3 T magnetic field at room temperature (300 K), protons (^{1}H) thermal polarization is only equal to 2.5×10^{-5}. For other nuclei, with lower gyromagnetic ratio, this value is even smaller. Consequently, the number of nuclei which actively contribute to the NMR signal is very low in thermal equilibrium conditions, leading to severe difficulties in the detection of low abundant or low gyromagnetic ratio nuclei. This aspect is even more relevant in magnetic resonance imaging (MRI), which provides high resolution and high contrast images of human and animal tissues. Due to low NMR sensitivity, MRI can only detect the protons contained in molecules like water and fat which are widely abundant, while it cannot follow the signal of other molecules, like the metabolites. This prevents ordinary MRI from obtaining real time information regarding dynamic processes involved in the metabolism. To overcome this low sensitivity limitation, many hyperpolarization techniques [16–20] have been devised to increase nuclear polarization, thus enhancing NMR signal: the brute force method, the spin exchange optical pumping (SEOP), the parahydrogen induced polarization (PHIP) and the dynamic nuclear polarization. The brute force method implies the use of very strong magnetic field (beyond 10 T) as well as of very low temperatures (around tens of mK) to achieve a sufficiently high nuclear polarization (over 30 %), but it is quite inconvenient for practical applications due to technical challenges and expensive costs. The SEOP relies on the transfer of polarization between vaporized alkali metals and noble gases and can reach very high polarization levels (around 100 %), but cannot be exploited to hyperpolarize solid compounds. The PHIP exploits parahydrogenation of the sample to convert the spin order of parahydrogen into nuclear polarization (even up to 60 % with several minutes lifetime at room temperature) via adiabatic field cycling; however, obtaining parahydrogen is quite challenging and it may be difficult to introduce ^{1}H pairs in the sample. In addition, optimization of the molecular design is required to maximize the transfer of polarization and removal of the parahydrogen is needed in some cases. On the other hand, the DNP process relies on a dynamic transfer of polarization from highly polarized electronic spins (in typical NMR magnetic fields electrons are fully polarized at liquid helium temperatures) to weakly polarized nuclear stimulated by microwave irradiation at a frequency close to the electron Larmor frequency, building an out-of-equilibrium hyperpolarized state. Even though DNP requires the presence of unpaired electrons, which, if not already present, are generally added by mixing the substrate with free radicals [21–23], rarely with rare earth ions [24], or generated in situ by ultraviolet irradiation [25]. Still there are several advantages: high efficiency, with nuclear polarization approaching 100 % in the optimal cases, a signal enhancement of many orders of magnitude, wide versatility. Due to possibility to hyperpolarize a large number of solid and liquid compounds, and relatively simplicity of experimental implementation with respect to the other hyperpolarization techniques, since it basically requires only the addition of a MW source to the

NMR setup [14, 19, 26], DNP has been successfully exploited to hyperpolarize a wide range of nuclear species ^{1}H, ^{2}H [27], ^{6}Li [28], ^{13}C [27], ^{15}N [29], ^{17}O [30], ^{19}F [31], ^{23}Na [32], ^{25}Mg [33], ^{27}Al [34], ^{29}Si [35], ^{31}P [36], ^{35}Cl [37], ^{43}Ca [38], ^{59}Co [39], ^{67}Zn [40], ^{77}Se [41], ^{89}Y [42], ^{107,109}Ag [43], ^{111,113}Cd [41], ^{115}In [44], ^{119}Sn [45], ^{121,123}Sb [46], ^{129}Xe [47], ^{133}Cs [48]. Even if the first practical application of DNP was the realization of highly polarized targets for nuclear particle physics experiments [26, 49], in the recent years it has become one of the main tools to achieve the so called molecular imaging (MI). The aim of MI [50–53] is to follow the real time evolution of biochemical processes in living cells, tissues and intact subjects. As explained above, by means of standard MRI this is not feasible due to the intrinsic low sensitivity. However, thanks to the birth of the so-called dissolution dynamic nuclear polarization (dDNP) [29, 54–61], where compounds of interest are hyperpolarized at very low temperatures, then solved and heated up to room temperatures and subsequently injected in vivo, magnetic resonance based MI [16, 62–64] has been successfully performed to study physiological processes like metabolism in healthy and tumoral tissues [65–82], perfusion studies [83],cardiovascular [84] and hepatic [85, 86] functions. DNP has played a key role also in other applications, ranging from solid state NMR of proteins [87–92] and hyperpolarization of gases [47, 93, 94] to the development heterogeneous catalysts, hybrid materials and polymers [36, 95–103], to additional medical studies [28, 35, 38, 104–108].

From a physical point of view, the DNP process can take place through different mechanisms: the Overhauser effect, the solid effect, the cross effect and the thermal mixing [15], depending on several experimental parameters like the electron paramagnetic resonance (EPR) linewidth and the nuclear Larmor frequency and leading to different hyperpolarization performances. Thus, there is a growing interest in investigating DNP both theoretically and experimentally, to check for example how the EPR spectrum changes upon MW irradiation and which of the abovementioned regimes takes place. On the other hand, almost all compounds hyperpolarized with DNP so far have, except for proteins, small sizes [109–122], however nowadays nanomedicine [53, 123, 124] relies on a wide range of functionalized macromolecules and nanoparticles.

In this thesis a theoretical study is presented in order to explain quantitatively the role of the free electron mutual interactions in determining the shape of the EPR spectrum in DNP experiments, and consequently the DNP mechanism taking place. This is important since the existing DNP modellization is not complete and cannot still explain some features regarding the EPR spectra observed in DNP experiments. Then an extensive description of DNP in βCyclodextrins (βCD's) macromolecules, a class of macromolecules that has been scarcely studied within the hyperpolarization context, is addressed. βCD's [125–127] are oligosaccharides formed by seven glucose units with a cone structure characterized by an inner hydrophobic cavity and an outer hydrophilic surface: this particular property allows βCD's to form inclusion complexes with several other molecules [128, 129]. Since they are also non

toxic and they have a good solubility in water, βCD's have found applications in nanomedicine as vectors for drug delivery [130–132] and as potential contrast agents [133–135]. Protons and ^{13}C (this latter in suitably ^{13}C enriched samples) hyperpolarization within βCD's is important for two main reasons: first, it provides new insight regarding how DNP takes place in this kind of macromolecules and how the out-of-equilibrium hyperpolarized state is affected by chemical changes of the local environment surrounding nuclear spins; second, it explores the possibility to exploit βCD's as possible candidates for MI and high resolution NMR experiments.

The second goal of the thesis focuses on the control of the magnetic state of molecular materials, the valence tautomers molecules, using external infrared (IR) light irradiation in view of possible data storage applications. Nowadays, the magnetic memory devices that are commercially available are made up of small, single and decoupled magnetic domains, where the single bit, i.e. the fundamental information unit, is stored in the orientation of the magnetization of the single domain [3]. However, there are three main open questions regarding the further development and improvement of these devices: size, read/write operations and heat dissipation. Concerning size, the single domain has a mean width which is less than 1 μm. The raggedness of the border of the bit produces noise that can be limited by reducing the size of the bit [136]. However, size reduction leads to an important physical boundary: the superparamagnetic limit [136–138]. Since the fundamental information is stored in magnetization direction in the single domain, the magnetization lifetime tells how long that information will be stored. For commercially available material, this lifetime, which depends on the domain size is around thousands of years, thus sufficiently long for memory devices. However, by reducing by a factor two the size of the domain, the lifetime reduces to tens of seconds, which is clearly a very short value [136, 137], due to the superparamagnetic limit. The second problem involves the limited read and write operations on magnetic memories: on one side, reducing the bit size implies that the writing magnetic field, necessary to switch the magnetization direction, has to increase in order to avoid thermally driven switching failures [139]; on the other hand, the read/write access time is limited to tens of nanoseconds [140]. Lastly, reducing bit size implies a higher concentration of electrical contacts which leads to larger heat dissipation. One possible solution is a revolution of the magnetic memory architectures, by using single molecules as bits [141–143], since they have already shown to mimic electronic device architectures [144–147]. There are two main families of compounds that can be exploited for this goal: the spin-crossover systems [148–151] and the valence tautomers [152–159]. In this thesis, the attention will be focused on the latter. The valence tautomer is a molecule formed by a metal ion (in our case Cobalt) with a redox-active organic ligand (belonging to the dioxolene family). The interest in this particular class of materials relies on their magnetic bistability, i.e. on the existence of two stable molecular magnetic state, a low spin (LS) and an high spin (HS)

one: these states can be associated with the fundamental binary values, 0 and 1, and thus these molecules could suitably be exploited for data storage applications. This magnetic bistability is due to an intramolecular electron transfer between the ion and the ligands that leads to a change in the global spin state of the molecule. Furthermore, it has been demonstrated that external stimuli, like temperature variation, infrared light irradiation and pressure application can induce the transition from LS to HS and viceversa [160–166], thus representing possible read and write protocols. In particular, after the light-induced transition the system is brought into an out-of-equilibrium state, with different features with respect to the thermal equilibrium one. Using these molecules for data storage application would lead in principle to some advantages: a three order of magnitude size reduction (from micrometer to nanometer scale), faster read and write access times (from nanoseconds to femtoseconds) and removal of the electric contacts (by using, for example, light to induce transitions, i.e. to write information), thus reducing heat dissipation. However, to test the feasibility of these compounds for data storage, it is necessary to properly study the light induced transition process as well as the lifetime and the coherence time of the light induced HS state in order to explore the stability of the system and the possible conditions of use. In this thesis the Superconducting Quantum Interference Device (SQUID) magnetometer and magnetic resonance techniques are employed to study the spin dynamics of the light induced HS state in a Cobalt-based valence tautomer.

The thesis is structured as follows. Chapter 2 introduces the basics concepts and quantities relevant in magnetic resonance, in particular the magnetic polarization and the spin-lattice relaxation time. In the chapter 3, after an overview of the theoretical background of DNP, the theoretical simulations of the EPR spectrum under DNP conditions are discussed and the description of the samples and the experimental NMR-DNP results and related discussions are presented. In chapter 4 the properties of Cobalt-based valence tautomers are discussed and the SQUID, NMR, Muon Spin Rotation (μSR) results in presence of external stimuli are given, with a particular focus on the application requirements of this compound for data storage application. Chapter 4 summarizes the main experimental conclusions, highlighting the future perspectives in both fields. The appendix A contains a brief description about the techniques and the sequences employed in the experiments.

Chapter 2

Basics of Magnetic Resonance

2.1 Polarization

The magnetic polarization, also called polarization, is a key concept of the magnetic resonance field. An ensemble of spins S = $\frac{1}{2}$, placed into a magnetic field H_0, experiences the Zeeman interaction, leading to the appearance of two Zeeman energy levels:

$$E_m = -\hbar\gamma_S H_0 \cdot m_S, \tag{2.1}$$

where m_S is the spin component along the external magnetic field direction and γ_S is the gyromagnetic ratio. For nuclear spins, γ is in most cases positive and the lower nuclear Zeeman state has spins aligned parallel to H_0, while the upper one has spins aligned antiparallel to H_0. On the other hand the electrons have a negative γ, so the spin orientation on each level will be opposite with respect to the nuclear system. However, in both case it is possible to define the magnetic polarization as the difference between the number of spin in the upper level and in the lower level:

$$P = \frac{N_{upper} - N_{lower}}{N_{upper} + N_{lower}}, \tag{2.2}$$

with the normalization factor $N_{upper} + N_{lower}$. If the system is highly polarized then P $\simeq \pm 1$, while if the system is weakly polarized then P $\simeq 0$. The energy difference between the two levels is:

$$E_Z = \hbar\gamma_S H_0 = \hbar\omega_S, \tag{2.3}$$

where ω_S is the Larmor frequency. Transitions are induced whenever the system absorbs or emits a quantum of energy equal to E_Z: a spin will switch to the upper or to the lower level, respectively. Electron spins have $\gamma/2\pi$ = -28.024 GHz/T, so their Larmor frequency will fall in the 10^0 - 10^2 GHz range when placed into a magnetic field of the order of 0.1 to 10 T, which is the order of magnitude of the fields used in magnetic resonance experiments,

meaning the microwaves (MW) are needed to induce transitions. On the other side, nuclear spins have γ in the range 10^0 - 10^1 MHz/T, which corresponds to Larmor frequencies in the 10^0 - 10^2 MHz range, which are matched by radiofrequency (RF) irradiation. The two level system can always be described by the spin temperature T_S, that is a thermodynamic quantity related to the population distribution over the two levels, provided that the spin can interact with each other much faster than with the external world (the so-called lattice) [167]. Since the nuclear (or the electron) spins are localized, the Boltzmann distribution describes the population in each level:

$$\begin{aligned} p_{lower} &= \frac{\exp\left(\frac{\hbar\omega_S}{2K_B T_S}\right)}{Z}, \\ p_{upper} &= \frac{\exp\left(\frac{-\hbar\omega_S}{2K_B T_S}\right)}{Z}, \end{aligned} \tag{2.4}$$

where $Z = p_{lower} + p_{upper}$ is the partition function. Sometimes the inverse spin temperature, defined as $\beta = \hbar/K_B T_S$, is used. Now, by inserting Eq. 2.4 in Eq. 2.2 one obtains

$$P = \tanh\left(\frac{\hbar\omega_S}{2K_B T_S}\right), \tag{2.5}$$

showing the spin temperature dependence of the magnetic polarization [167]. When T_S is equal to 0, then P is 1 and the system is completely polarized (all spins stay on the lower level), while if T_S is $+\infty$ then P is 0 and the system is not polarized (equal population on both levels). Negative spin temperatures correspond to population inversion, which eventually forces all the spin to populate the upper level, yielding P = -1. However, the spin system is never completely isolated, since it is always surrounded by the external environment, which is called lattice: it is characterized by its own spin temperature T_L, it can exchange energy with the spins and it is assumed to have a heat capacity much larger than the spins one. In thermal equilibrium conditions, a simple thermodynamic consideration holds: $T_S = T_L$. However, the abovementioned transitions induced by external electromagnetic wave irradiation may change the population distribution of the two level system, thus changing the spin temperature T_S, which may become larger or smaller than T_L. In this case it is said that the spin system is out-of-equilibrium: the thermal contact with the lattice will force the spin temperature T_S to go back to the the thermal equilibrium value T_L through an exchange of energy between the spins and the lattice. This process is called relaxation.

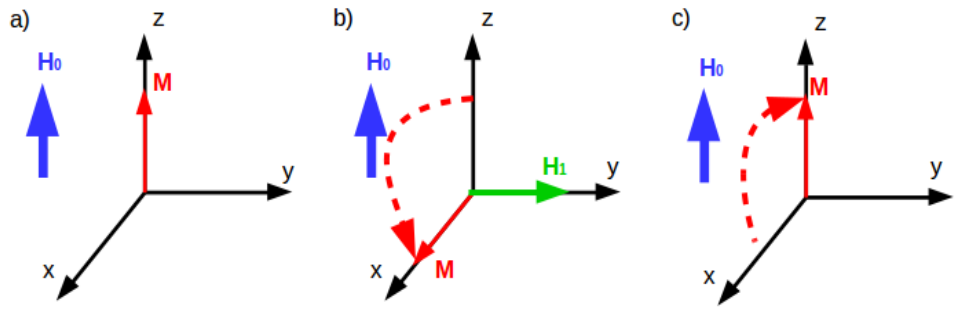

Figure 2.1: Picture of the simplest pulsed magnetic resonance experiment. a) The static field H_0 generates the magnetization M. b) The oscillating field H_1 tilts M by a 90° angle. c) M relaxes back to initial condition.

In nuclear and electron pulsed magnetic resonance experiments, a static field H_0 is used to induce a nuclear or electronic magnetization M along H_0, which is then rotated by an external oscillating field H_1 (at the Larmor frequency). If one supposes that H_0 is parallel to the $\hat{z}$ axis then M will be directed along that axis as well (Fig.2.1a). By applying the field H_1 along the $\hat{y}$ axis for a given time, it is possible to tilt M along the $\hat{x}$ axis through, for example, a 90° rotation (Fig.2.1b). After switching off H_1, two types of relaxation will take place: the spin-spin relaxation and the spin-lattice relaxation. The former one is a dephasing of the $\hat{x}$ components of the spins (i.e. a mutual exchange of energy between spins) and will cause the disappearance of M along the transverse $\hat{x}$-$\hat{y}$ plane within a timescale named T_2. The latter one is the exchange of energy between the spins and the lattice and causes the build-up of M along the $\hat{z}$ axis, i.e. along the thermal equilibrium condition, within a timescale named T_1 (Fig.2.1c). These two timescales can be measured in magnetic resonance experiments and allow to unravel microscopic properties of the compound studied.

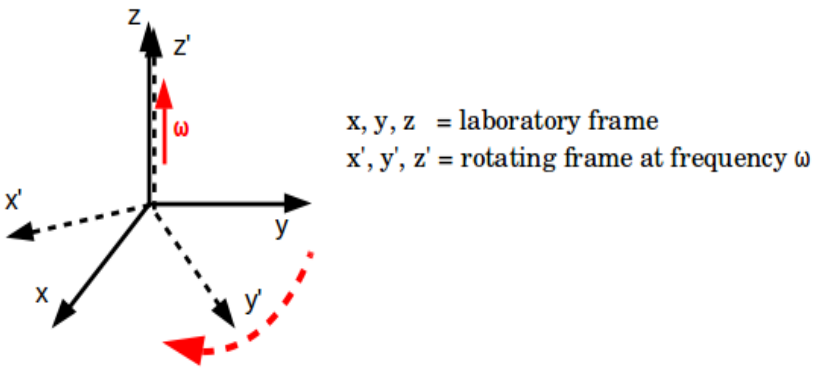

Figure 2.2: Picture of the laboratory frame and of the rotating frame used to describe magnetic resonance experiments.

When describing the motion of the magnetization in magnetic resonance

experiments, it is useful to introduce a rotating frame along the fixed laboratory frame (Fig. 2.2). It rotates with an angular frequency ω parallel to the $\hat{z}$ axis so that its $\hat{z}'$ is superimposed to the $\hat{z}$ axis. When ω matches the Larmor frequency then any dynamic effect due to the static field H_0 in the rotating frame is cancelled, thus simplifying the calculations. An example comes from the previously described experiment (Fig.2.1). In presence of both the static and the oscillating magnetic fields, in the rotating frame (with frequency ω) the total field probed will be:

$$H_T = \left(H_0 - \frac{\omega}{\gamma} \right) \hat{z}' + H_1 \hat{y}' \tag{2.6}$$

When ω matches the Larmor frequency then the H_T reduces to H_1, thus apparently cancelling the effect of the static field.

2.2 Bloch Equations and MR Signal

To quantitatively describe the motion of the magnetization M (resulting from an ensemble of N spins S, with γ indicating the gyromagnetic ratio) in a magnetic resonance experiment one can initially resort to the Bloch equations [6, 7]. Suppose that the external static magnetic field H_0 is directed along $\hat{z}$ and so does M. Then an other magnetic field H_1, rotating in the $\hat{xy}$ plane at a frequency ω, is added so that the total field probed by M is $H = H_0\hat{z} + H_1(\hat{x}\cos\omega t + \hat{y}\sin\omega t)$. By adding the relaxation times introduced in the previous section, T_1 and T_2, the Bloch equation describing the time evolution of the components of M can be cast in the form:

$$\frac{dM_z}{dt} = \gamma(M \times H)_z + \frac{M_0 - M_z}{T_1} \tag{2.7}$$

$$\frac{dM_x}{dt} = \gamma(M \times H)_x - \frac{M_x}{T_2} \tag{2.8}$$

$$\frac{dM_y}{dt} = \gamma(M \times H)_y - \frac{M_y}{T_2} \tag{2.9}$$

An analytical solution can be found in the limit $H_1 \ll H_0$ and considering the stationary state, $dM/dt = 0$:

$$M_z \simeq M_0, \tag{2.10}$$

$$M_x = \chi' \cdot H_1, \tag{2.11}$$

$$M_y = \chi'' \cdot H_1, \tag{2.12}$$

where χ' and χ" are the real and the imaginary part of the magnetic susceptibility, the quantity describing the response of the sample to an external oscillating magnetic field at a frequency ω. Explicit expressions are

$$\chi'(\omega) = \chi_0 \omega_S T_2 \frac{(\omega - \omega_S)}{1 + (\omega - \omega_S)^2 T_2^2}, \tag{2.13}$$

$$\chi''(\omega) = \chi_0 \omega_S T_2 \frac{1}{1 + (\omega - \omega_S)^2 T_2^2}, \tag{2.14}$$

where ω_S is the Larmor frequency. The factor χ_0 is the static susceptibility, describing the response to a static field and is given by the Curie theory:

$$\chi_0 = \frac{N\gamma^2\hbar^2 I(I+1)}{3K_B T} \tag{2.15}$$

From Eq. 2.14 it is clear that whenever the resonance condition $\omega = \omega_S$ is met then the energy transfer from H_1 to the spins is maximized and the magnetization M will move away from the equilibrium position. When the field H_1 is switched off then M will tend to go back to the equilibrium position, generating a variation in the magnetic field flux around the sample and, if the sample is placed into a coil, inducing a current which is the MR signal. Thus one can write:

$$G(t) \propto < M_x(t), M_x(0) > \tag{2.16}$$

i.e., the MR signal is directly proportional to the time correlation function of the transverse component of the magnetization. It is then clear that as M_x increases the MR signal intensity will increase as well. Eq. 2.16 is valid in the rotating frame when the resonance condition is matched. In the laboratory frame instead the effect of the static field is to multiply Eq. 2.16 by a factor $\cos(\omega_S t)$.

2.3 Spin-Lattice Relaxation Rate

The Bloch equations (Eq.s 2.7, 2.8, 2.9) take in account spin relaxation by introducing the relaxation times T_1 and T_2 but they do not provide any further detail about it. If one considers a $\frac{1}{2}$ spin placed into a magnetic field H_0 two Zeeman levels will appear ($|1\rangle$ and $|2\rangle$): when the spin is brought out-of equilibrium by any external perturbation, the timescale characterizing its return to the equilibrium state is the spin-lattice relaxation time, namely T_1. Thus T_1 plays a fundamental role in the investigation of out-of-equilibrium states. The spins can be very sensitive probes of the local magnetic fields, which might be modulated by molecular or glassy dynamics in some cases, by detecting them directly or indirectly. A strategy to evaluate T_1 is to take into account a general external perturbation characterized by a fluctuating local magnetic field h(t) at the spin site. The related hamiltonian is:

$$\mathcal{H}_{fluct} = -\gamma\hbar I h(t) \tag{2.17}$$

that is a perturbation to the principal hamiltonian, containing the Zeeman term. The probability that $\mathcal{H}_{fluct}$ induces a transition from $|1\rangle$ to $|2\rangle$ after a certain time t is given by:

$$P_{1,2}(t) = \frac{1}{\hbar^2} \left| \int_0^t \langle 1 | \mathcal{H}_{fluct} | 2 \rangle \exp(+i\omega_I t') dt' \right|^2 \tag{2.18}$$

where $\omega_I = \gamma H_0$ is the spin Larmor frequency. If one considers an ensemble of spins, then one has to average over all the transition elements $\langle 1| \mathcal{H}_{fluct} |2\rangle$ introducing the correlation function G(τ). The transition rate becomes:

$$W_{1,2} = \frac{P_{1,2}(t)}{t} = \frac{1}{\hbar^2} \int_{-\infty}^{+\infty} G(\tau) \exp(+i\omega_I \tau) d\tau \tag{2.19}$$

where the integral has been extended over an infinite range of fluctuation times. Eq. 2.19 shows that the transition rate is the Fourier transform of the fluctuating field correlation function at the spin Larmor frequency. If H_0 is directed along $\hat{z}$ only the $\hat{x}$ and $\hat{y}$ component of h(t) must be retained in the correlation function because only they are able to induce transitions between Zeeman levels. Furthermore, since h_x(t) and h_y(t) can be expressed as function of the corresponding scale operators h_+(t) and h_-(t) and since $W_{1,2} = 1/(2T_1)$, Eq. 2.19 becomes:

$$\frac{1}{T_1} = \frac{\gamma^2}{2} \int_{-\infty}^{+\infty} < h_-(\tau) h_+(0) > \exp(+i\omega_I \tau) d\tau \tag{2.20}$$

where Eq. 2.17 has been exploited to express the fluctuating field h(t). The conclusion is that the spin-lattice relaxation rate is the Fourier transform of the correlation function of the transverse components (to satisfy the transition rules from quantum mechanics) of the external fluctuating field at the spin Larmor frequency (to satisfy the conservation of total energy). Eq. 2.20 is the general form of the spin-lattice relaxation rate in the presence of a fluctuating magnetic field and it is the starting point in the analysis of the process which brings an out-of-equilibrium system back to its equilibrium state through an exchange of energy with the surrounding lattice. One can consider the typical exponential decay for the correlation function:

$$< h_-(\tau), h_+(0) > = < \Delta h_\perp^2 > \exp\left(-\frac{\tau}{\tau_C}\right) \tag{2.21}$$

where τ_C is the correlation time characterizing the fluctuations. Thus the $1/T_1$ will be a lorentzian function of $\omega_C = 1/\tau_C$:

$$\frac{1}{T_1} = \frac{\gamma^2}{2} < \Delta h_\perp^2 > \frac{2\tau_C}{1 + \omega_I^2 \tau_C^2} \tag{2.22}$$

It is possible to approximate Eq. 2.22 in case of fast motions ($\omega_I \tau_C \ll 1$) or slow motions ($\omega_I \tau_C \gg 1$), yielding, respectively:

$$\frac{1}{T_1} = \gamma^2 < \Delta h_\perp^2 > \tau_C, \tag{2.23}$$

$$\frac{1}{T_1} = \gamma^2 < \Delta h_\perp^2 > \frac{1}{\omega_I^2 \tau_C}. \tag{2.24}$$

As shown in the next chapter, the local magnetic fields can be modulated by different phenomena. In amorphous compounds low-frequency glassy modes, involving changes in the local structures of molecules, can modulate the local magnetic fields which become dynamic even at liquid helium temperatures. On the other side, at higher temperatures, the activated molecular motion makes the magnetic interaction fluctuate with a frequency clearly depending on the speed of the motion. Thus the analysis of the $1/T_1$ is a powerful tool to investigate the microscopic environment.

Chapter 3

Dynamic Nuclear Polarization (DNP)

As stated in the introduction, hyperpolarization techniques aims at enhancing the nuclear thermal polarization, which at room temperature and for magnetic fields around 1 to 3 T ranges from 10^{-5} to 10^{-6} depending on the nuclear isotope, leading to the NMR signal amplification. In the last decades several methods have been developed: the brute force method, the spin exchange optical pumping (SEOP), the parahydrogen induced polarization (PHIP), the use of nitrogen vacancy (NV) defects and the dynamic nuclear polarization (DNP) [16–20]. The brute force method simply requires that the sample is placed into the highest magnetic field (beyond 10 T) at the lower temperature possible (down to tens of mK) in order to maximize the ratio appearing in Eq. 2.5. By considering $H_0 = 20$ T and T = 10 mK, then proton polarization would be P = 0.31, which is a huge value: however, achieving such extreme conditions is not practical and, furthermore, is quite expensive. The SEOP method is used to hyperpolarize noble gases (like ^{3}He, ^{83}Kr and ^{129}Xe) with their polarization $P \simeq 1$ in many cases, demonstrating the efficiency of the process. Within a SEOP setup an optical cell contains the target noble gas and a vaporized alkali metal, like Rb or Cs: in the first step a circularly polarized laser is used to optically pump the metal ions while in the second step the electronic polarization is transferred to the nuclear spins of the noble gas by spin exchange due to Fermi contact interaction. The accumulation rate of nuclear polarization shall exceed the nuclear spin-lattice relaxation rate to ensure an efficient process. The main limit of SEOP is that it only works with gases. The PHIP method requires the addition of parahydrogen pairs (p-H_2) to the unsaturated chemical bonds in a sample of interest, with an addition rate faster than the nuclear spin-lattice relaxation rate. The spin order is then converted into nuclear hyperpolarization of other isotopes by RF pulses or field-cycling scheme. While having a good efficiency, with $P > 0.1$, the need of unsaturated chemical bonds in the target sample is the main limit for PHIP. The use of the negatively charged nitrogen vacancy defects is quite a recent

technique [168]. It relies on the optical pumping of the NV centers inside diamond leading to a huge electronic polarization, that is then transferred to the surrounding nuclear spins (by means of MW irradiation in case of solid and liquid samples or by spin collision in case of gases) which are brought into the out-of-equilibrium hyperpolarized state. The last and most widespread method is DNP.

In Fig. 3.1 ^{1}H, ^{13}C and electron spin polarization are reported as function of temperature at $H_0 = 3.45$ T, evaluated as $P = \tanh\left[(\hbar\gamma H_0) / (2K_B T)\right]$. Due to the large difference in the gyromagnetic ratio γ, it is clear that electrons are much strongly polarized than nuclear spins, in particular at liquid helium temperatures, where the electron polarization is close to unity (100 %), while nuclear polarizations are far smaller (10^{-2} to 10^{-3} %).

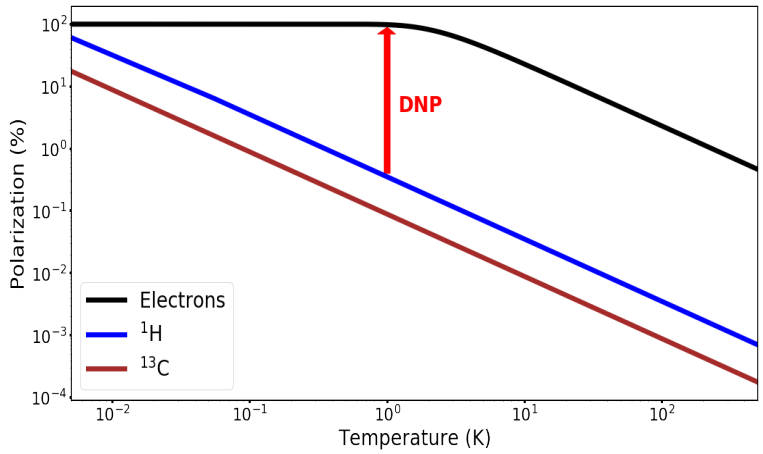

Figure 3.1: Electron (black), ^{1}H (blue), ^{13}C spin polarizations temperature dependence at 3.45 T.

However, external MW irradiation, at a frequency close to the electron Larmor frequency and at such low temperatures, might help to transfer the polarization from free electron spins to nuclear spins, achieving an out-of-equilibrium hyperpolarized nuclear state. At higher magnetic fields, above 9 T, the electrons are completely polarized already at 80 - 90 K: this is the so-called high field DNP [22, 95, 169, 170]. In some cases, like metals or paramagnetic substances, the free electrons are already present, in the form of conduction electrons or paramagnetic centers, while in organic diamagnetic compounds, they can be added in form of paramagnetic impurities, like free radicals or metal ions [21–24], or temporarily generated by external UV irradiation [25]. The transfer of polarization is made possible thanks to the magnetic hyperfine interaction that allows simultaneous electron and nuclear spin flips: in metals and liquid compounds, this interaction is dominated by the Fermi scalar contact interaction and leads to the Overhauser effect (with maximum ^{1}H enhancement equal to 660) [171], while in diamagnetic compounds the magnetic dipolar interaction plays the key role and in this case the process is properly called DNP [14, 15]. DNP is a complex physical process

that can take place through different mechanisms, namely the solid effect (SE) [172], the thermal mixing (TM) [173] and the cross effect (CE) [174]. In the former, the polarization transfer is realized by means of two body interactions, flipping one electron and one nuclear spin each, stimulated by external MW irradiation. On the other hand, the second mechanism is a collective process that requires a thermodynamic description, where the electrons and the nuclei are both characterized by their own spin temperature, with two steps: fist, the MW irradiation cools down the electron spin temperature and second, the nuclear spins are cooled in turn by the thermal contact with electrons, that is realized through three body interaction involving two electrons and one nucleus. The last mechanism, the cross effect, is something in between the SE and the TM since predicts that nuclear hyperpolarization is achieved through the three body interactions (as it happens in TM) which are directly stimulated by MW irradiation (as in SE) without resorting to thermodynamics. Since distinguishing between these regimes is not trivial, a theoretical background is provided in the first section of this chapter to present the equations relevant for model interpretation and data analysis. In particular, the first two subsections will focus on a quantum-mechanics based treatment of the rate equations describing the nuclear polarization time evolution by combining the effect of DNP hyperpolarization build-up and nuclear spin-lattice relaxation to find the steady-state out-of-equilibrium condition. Furthermore, since the EPR spectrum changes its shape upon MW irradiation and depending on the DNP regime taking place, numerical simulations are presented in the third subsection to investigate the quantitative role of the electron mutual interactions and of the MW power in typical DNP conditions.

The most striking application of DNP is the magnetic resonance based-MI, where compounds of interest are hyperpolarized at low temperatures and at high magnetic fields, then heated and dissolved in physiological solutions and eventually injected in human or animal patients in order to perform a selective imaging to follow their real time evolution: this is the so-called dissolution DNP (dDNP) [29, 54, 58–60, 175] and it takes around 10 s (from heating to in vivo transfer) [58–60] (Fig. 3.2). There are many concerns about studying DNP in view of dDNP applications. First of all, though large proton polarization has been obtained with DNP, ^{1}H MI is hindered by the very short relaxation times at room temperatures, that prevent from performing the imaging sequences required, since hyperpolarization is rapidly lost. Indeed, most dDNP studies and MI have been focused on other nuclear species, like ^{13}C [62–66, 69–74, 76–79, 81–83, 176, 177] which, due to lower gyromagnetic ratio, is in general characterized by longer relaxation times. However, compounds of MI interest must be enriched with ^{13}C before DNP and it is vital to study how different chemical environments surrounding ^{13}C atoms change their hyperpolarization performances.

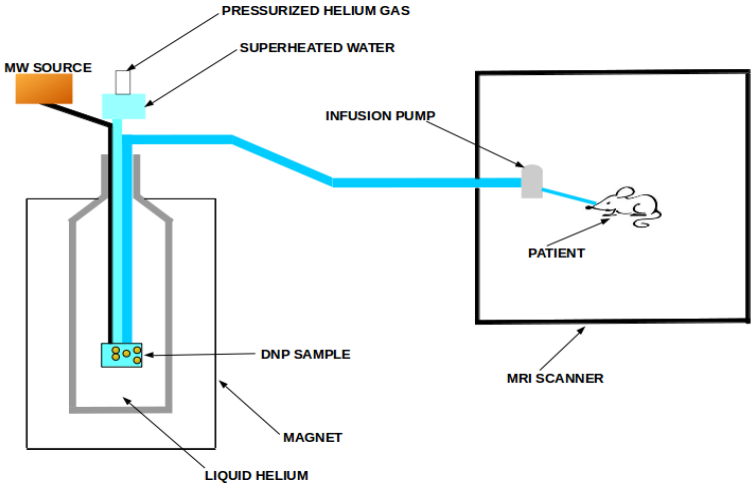

Figure 3.2: Schematic view of the setup for dDNP.

Significant NMR signal enhancement must be achieved, in order to make the NMR signal detectable. Furthermore, the size [62] of the selected molecule and the solid phase (crystalline or amorphous) of the sample [56, 117, 178] are expected to affect the DNP process. Regarding the dissolution and the injection steps, one must assure that the compound is completely soluble and that any free radical have a negligible impact on the patient. Lastly, since the transfer time in dDNP lasts 3 to 15 s, the nuclear spin-lattice relaxation time at body temperature must be high enough to preserve at least part of the hyperpolarization for the imaging sequence, which may take at least 1 minute [60]. Other applications of DNP involve the high resolution NMR spectroscopy experiments, where it is fundamental to combine DNP with magic angle spinning (MAS) [88, 89, 100, 179, 180]. Fewer requirements are needed here: high hyperpolarization performances and short polarization (build-up) times.

Both theoretical and experimental questions are addressed in the second and third sections of this chapter, along with sample preparation description and presentation and interpretation of the DNP-NMR results.

3.1 Typical DNP Regimes

3.1.1 The Solid Effect

The solid effect is a polarization process, that allows to transfer the polarization from electrons to nuclei coupled via magnetic dipolar interaction by simultaneous flip of both spins and that takes place when the EPR linewidth is much smaller than the nuclear Larmor frequency:

$$\Delta\omega_S \ll \omega_I. \tag{3.1}$$

A simplified and qualitative picture useful to explain how the SE works is shown in Fig. 3.3. Suppose that, in a static magnetic field H_0, the electron system (S

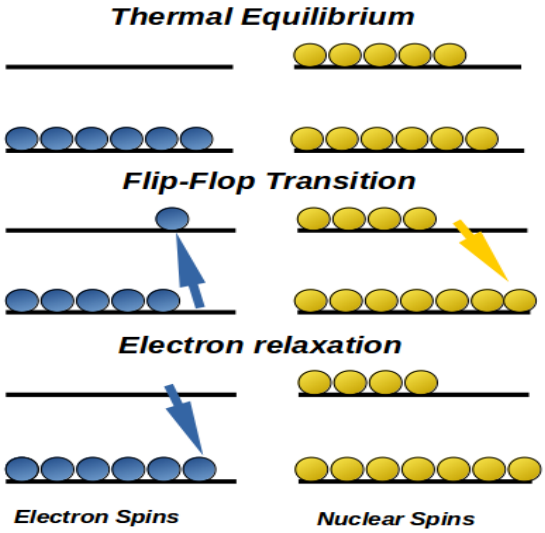

Figure 3.3: Schematic view of the DNP via the SE, with the flip-flop transition involving one electron (blue circles) and one nucleus (yellow circles). Zeeman energy levels are not in scale.

$= \frac{1}{2}$) is completely polarized ($P_S \simeq 100$ %), while the nuclear one ($I = \frac{1}{2}$) is not ($P_I \simeq 0$ %). Thanks to the hyperfine interaction ($S \cdot \bar{\bar{A}} \cdot I$), MW irradiation at a frequency $\omega_{MW} = \omega_S \pm \omega_I$ is able to induce the so-called forbidden transitions, where both electron (with Larmor frequency $\omega_S = H_0 \cdot \gamma_S$) and nucleus (with Larmor frequency $\omega_I = H_0 \cdot \gamma_I$) spins flip, provided that $\bar{\bar{A}}$ is a tensor. Suppose that MW irradiation stimulates only the flip-flop transition (this is possible thanks to condition 3.1): since all the electrons are in the lowest electron Zeeman level, the flip-flop transition will send one electron into the upper level. At the same time, due to the frequency relation, a nucleus will go in the upper nuclear Zeeman level too. In this way, one electron and one nucleus will be out-of-equilibrium: since the electron spin-lattice relaxation is faster than the nuclear one, the electron will go back to the starting condition almost immediately, while the nucleus will not. By repeating this process several times, the nuclear spins will hyperpopulate one of the two nuclear Zeeman level, creating an hyperpolarized out-of-equilibrium state. If the flip-flip transition is chosen, then the nuclear spins will hyperpopulate the other nuclear Zeeman level and the DNP enhanced polarization will change its sign. Since we are treating a diamagnetic solid doped with paramagnetic impurities, the electron will interact only with surrounding nuclei: the nuclear hyperpolarization will be spread throughout the sample due to the nuclear spin diffusion, a process that is based on nuclear dipolar magnetic interaction, which will be explained at Sect. 3.1.4. To build a quantitative description of the SE, one might refer to quantum mechanics [15, 181]. The simplest possible model contains an electron spin S interacting with a nuclear spin I, both placed into a static magnetic field

H_0 (pointing along the $\hat{z}$ axis) and subject to a MW field $H_1 \cos(\omega_{MW} t)$ (along the $\hat{x}$ axis). The hamiltonian is:

$$\mathcal{H} = \hbar \left[\omega_S S_z + 2\omega_{1S} S_x \cos(\omega_{MW} t) - \omega_I I_z + \frac{1}{2} S_z \left(\bar{\bar{A}}_{z-} I_+ + \bar{\bar{A}}_{z+} I_- \right) \right], \quad (3.2)$$

where the first and the third terms are the electron and nuclear Zeeman interactions, the second term is the interaction between electrons and MW field and the last term is the truncated hyperfine interaction. By means of a series of reference frames changes and truncation of negligible terms (like those inducing pure nuclear transitions, which are not useful for SE), it is possible to write the following expression for the hamiltonian:

$$\begin{aligned} \mathcal{H} = \hbar(\omega_S - \omega_{MW}) S_z + \frac{1}{2}\hbar\omega_{1S}(S_+ + S_-) - \hbar\omega_I I_z \\ -\frac{1}{8}\hbar(S_+ + S_-)\left(\bar{\bar{A}}_{z-} I_+ - \bar{\bar{A}}_{z+} I_- \right) \sin\theta\cos\theta \\ -\frac{1}{8}\hbar(S_+ - S_-)\left(\bar{\bar{A}}_{z-} I_+ + \bar{\bar{A}}_{z+} I_- \right) \sin\theta, \end{aligned} \quad (3.3)$$

where θ is the angle between the effective magnetic field acting on the electron spin (H_0+$H_1 \cos(\omega_{MW} t)$, in the rotating reference frame) and the $\hat{z}$ axis. The eigenstates may be written in the form $|m_S, m_I\rangle$. These eigenstates are:

- a) $|+\frac{1}{2}, -\frac{1}{2}\rangle$
- b) $|+\frac{1}{2}, +\frac{1}{2}\rangle$
- c) $|-\frac{1}{2}, -\frac{1}{2}\rangle$
- d) $|-\frac{1}{2}, +\frac{1}{2}\rangle$

The non-diagonal terms of Eq. 3.3 yield the following transitions:

- the term $\frac{1}{2}\hbar\omega_S (S_+ + S_-)$ induces transitions $|m_S\rangle = |+\frac{1}{2}\rangle \leftrightarrow |+\frac{1}{2}\rangle$, which are pure electronic transitions, not leading to DNP;
- the term containing $\bar{\bar{A}}_{z-} S_+ I_+ + \bar{\bar{A}}_{z+} S_- I_-$ induces transitions where S and I flip in the same direction, i.e. flip-flip transitions;
- the term containing $\bar{\bar{A}}_{z+} S_- I_+ + \bar{\bar{A}}_{z-} S_+ I_-$ induces transitions where S and I flip in opposite directions, i.e. flip-flop transitions.

Flip-flip and flip-flop transitions play the key role in the dynamic transfer of polarization from electrons to nuclei. Exploiting the density matrix approach it is possible to write the rate equations for the eigenstates populations in the cases the MW irradiation induces one transition or the other. For flip-flip transitions:

$$W_{flip-flip} = \frac{1}{2}\pi \frac{\left| \frac{1}{2} \bar{\bar{A}}_{z+} \right|^2 \omega_1^2}{\omega_I^2} h_e(\omega_S - \omega_{MW} - \omega_I), \quad (3.4)$$

while for flip-flop transitions:

$$W_{flip-flop} = \frac{1}{2}\pi \frac{\left|\frac{1}{2}\bar{\bar{A}}_{z+}\right|^2 \omega_1^2}{\omega_I^2} h_e\left(\omega_S - \omega_{MW} + \omega_I\right), \tag{3.5}$$

where h_e refers to the electron homogeneous lineshape. The next step is to extend this simple model to a system containing N_S electrons and N_I nuclei, by introducing summation over all available spins in the rate equations. Eq. 3.4 and 3.5 become:

$$W_{flip-flip} = \frac{1}{2}\pi \frac{|\bar{\bar{A}}|^2 \omega_1^2}{\omega_I^2} \frac{N_S}{N_I} g\left(\omega_{MW} + \omega_I\right), \tag{3.6}$$

$$W_{flip-flop} = \frac{1}{2}\pi \frac{|\bar{\bar{A}}|^2 \omega_1^2}{\omega_I^2} \frac{N_S}{N_I} g\left(\omega_{MW} - \omega_I\right), \tag{3.7}$$

where A is the hyperfine interaction strength averaged over electrons and nuclei, while g is the full EPR lineshape, i.e. the inhomogeneous convolution of many homogeneous lineshapes h used above. The corresponding rate equation for the nuclear polarization is:

$$\begin{aligned} \frac{\partial P_I}{\partial t} = &-2W_{flip-flip}\left[P_I - P_S\left(\omega_{MW} + \omega_I\right)\right] + \\ &-2W_{flip-flop}\left[P_I + P_S\left(\omega_{MW} - \omega_I\right)\right], \end{aligned} \tag{3.8}$$

showing how it grows through SE after switching on the MW field. It is now possible to distinguish two cases:

- 1) the EPR linewidth is smaller than ω_I: it is possible to selectively irradiate either the flip-flip or the flip-flop transition, yielding a positive or a negative DNP enhanced polarization. By calculating the DNP profile, i.e. the DNP enhanced polarization as a function of ω_{MW}, one observes two well separated peaks, each with opposite sign, corresponding to the two abovementioned transitions. This case is called well-resolved solid effect (Fig. 3.4a).

- 2) the EPR lineshape is of the same order of ω_I: it is no longer possible to irradiate selectively one of the two forbidden transitions and, since they aim to build polarizations with opposite signs, their effects will balance each other and the global efficiency of the process will be reduced. The DNP profile displays two overlapping opposite peaks. This case is called differential solid effect (Fig. 3.4b).

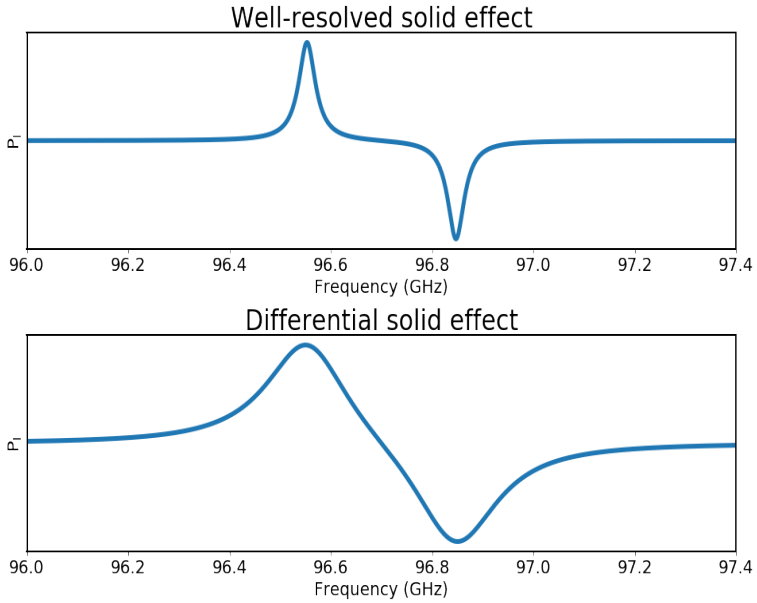

Figure 3.4: DNP profile, namely the nuclear polarization over ω_{MW}, for a) well-resolved solid effect and b) differential solid effect.

The well-resolved SE has been observed experimentally many times, mainly using narrow EPR spectrum free radicals, like trityls [22, 24, 182, 183], exploiting single crystals to reduce the electron g-factor anisotropy as much as possible, to limit the EPR spectrum broadening [184] or using low concentration of free radicals [23]. Also differential SE has been observed experimentally [182, 185, 186]. So far, the quantum mechanics treatment has explained how SE works, showing that the hyperfine interaction, stimulated by MW can transfer polarization from electrons to nuclei. However, the same interaction, in the absence of MW, is a channel for the nuclear spin-lattice relaxation: each time an electron spin flips due to the interaction with a phonon mode, for example, with a rate given by $1/\mathrm{T}_{1e}$, the hyperfine interaction may cause a nuclear spin to flip. It is possible to demonstrate [15] that the nuclear spin-lattice relaxation rate for this process, that is called direct relaxation, is:

$$\frac{1}{T_{1n}} = \frac{1}{T_{1e}} \frac{2N_S|\bar{\bar{A}}|^2}{N_I\omega_I^2}, \tag{3.9}$$

regardless of the process that causes the electron relaxation (direct, Raman or Orbach) in the slow motion limit (Eq. 3.9 is an explicit form of Eq. 2.24). By introducing the lattice polarization P_L, that is the electron polarization at thermal equilibrium at the temperature T, the rate equation 3.8 must be modified by adding the following term:

$$\frac{\partial P_I}{\partial t} = -\frac{1}{T_{1n}} \left(1 - P_L P_S\right) P_I, \tag{3.10}$$

which counteracts the polarization growth induced by SE and thus limits the maximum enhancement achievable, i.e. it lowers the height of the peaks rep-

resented in Fig. 3.4. The rate equation can be solved in the case of a steady state, by taking $\partial P_I/\partial t = 0$. The solution for well-resolved solid effect (in case of stimulating the flip-flip transition, but an analogous formula is valid also for flip-flop transition) is:

$$P_I = \frac{W_{flip-flip} T_{1e}}{W_{flip-flip} T_{1e} + (1 - P_L^2)} P_L. \tag{3.11}$$

For differential solid effect:

$$P_I = \frac{W_{flip-flip} T_{1e} - W_{flip-flop} T_{1e}}{W_{flip-flip} T_{1e} + W_{flip-flop} T_{1e} + (1 - P_L^2)} P_L. \tag{3.12}$$

This highlights the double role played by the electrons: on one side, they help to build nuclear hyperpolarization, but, at the same time, they cause its decrease through T_{1n} processes. It is clear that a compromise must be found in the number of free electron spin present in the sample: experiments have shown that in the SE process the DNP efficiency depends on the polarizing agent concentration [187].

3.1.2 Thermal Mixing

The thermal mixing (TM) process requires a completely different approach with respect to the solid effect and it takes place when the nuclear Larmor frequency is of the same order or even smaller than the EPR linewidth [167, 188]:

$$\Delta\omega_S \gtrsim \omega_I. \tag{3.13}$$

In this limit, the flip-flop and flip-flip transitions cannot be induced selectively and thus their effect is cancelled: they are no longer responsible for the polarization transfer from electrons to nuclei. The TM mechanism can be invoked to explain DNP in this limit. In the first step, the system is described by thermodynamical point of view as made up of four different energy reservoirs [42], each corresponding to a term of the total hamiltonian and characterized by an own inverse spin temperature, depicted in Fig. 3.5:

- a) the electron Zeeman reservoir, described by the interaction of electrons with the static field H_0, with inverse spin temperature α;
- b) the nuclear Zeeman reservoir, described by the interaction of nuclei with the static field H_0, with inverse spin temperature β_n;
- c) the electron dipolar reservoir, described by the magnetic dipolar interaction between electrons, with inverse spin temperature β_e;
- d) the lattice reservoir, described by the environment surrounding electrons and nuclei, with inverse spin temperature β_L.

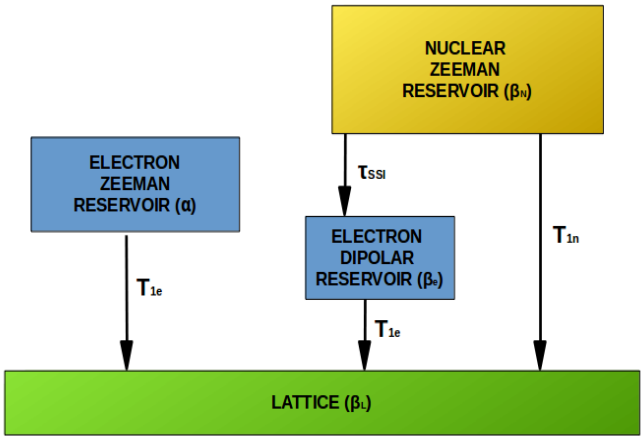

Figure 3.5: Schematic view of the four energy reservoirs involved in the TM regime with the relaxation times between them and, in round brackets, the inverse spin temperatures.

In terms of quantum mechanics, the inverse spin temperatures α and β_n depend on the population distribution in the electron Zeeman and nuclear Zeeman energy levels, respectively. On the other hand, the interaction between electrons transforms the sharp electron Zeeman levels into wide bands of sub-levels: the population distribution inside each band determines β_e. Finally, β_L corresponds to the inverse of the working temperature, that is the temperature at which the whole process takes place. In a thermal equilibrium condition, $\alpha = \beta_n = \beta_e = \beta_L$ (see Fig. 3.6). However, by applying MW irradiation at a

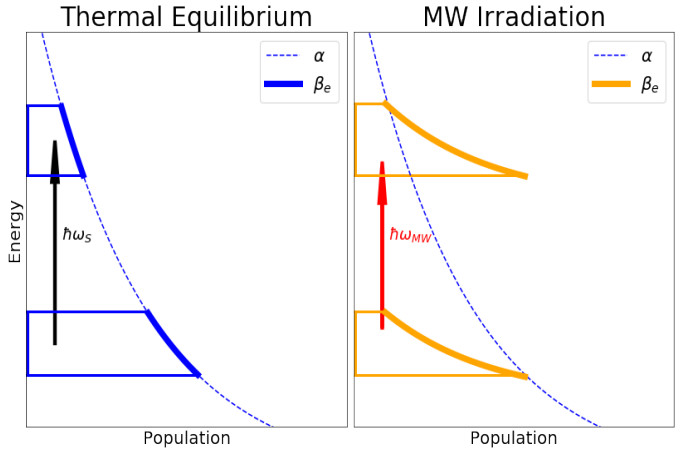

Figure 3.6: Schematic representation of the cooling process. At thermal equilibrium (left panel), $\alpha = \beta_e$ and the population distribution of the two Zeeman levels and inside the bands can be described by one spin temperature. By MW irradiation (right panel) at a frequency (ω_{MW}) slightly lower than the electron Larmor frequency (ω_S), α is decreased, while β_e increases, achieving the dynamic cooling of the electron dipolar reservoir, through enhancement of the population difference between the upper and the lower sublevels in each band.

frequency slightly lower than ω_S, transitions between from the upper energy

sub-levels of the lower band to the lower energy sub-levels of the upper band are induced (see Fig. 3.6): this causes a decrease of α, but, at the same time, an increase of β_e, i.e. the electron dipolar reservoir is dynamically cooled. The second step of TM requires a thermal contact between this latter reservoir and the nuclear Zeeman reservoir, that is thus cooled as well. The increase of β_n causes the increase in the population difference between the nuclear Zeeman energy levels and an increase of the nuclear polarization, even by orders of magnitude. The mentioned thermal contact is realized by mean of three body interactions [188], where two electron spins with slightly different ω_S flip simultaneously in different directions and the remaining energy is given to a nuclear flip, which can flip itself, as depicted in Fig. 3.7. This process is possible since the order of magnitude of the electron mutual interaction is the same of that of the nuclear Zeeman, i.e. tens to hundred of MHz. A striking feature of TM is that all nuclear species involved reach the same spin temperature [27, 42, 54, 110, 189].

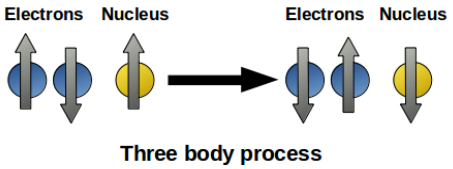

Figure 3.7: Schematic view of the triple spin flip process involving two electron and one nuclear spins.

To get a quantitative picture one has to resort to the quantum mechanics treatment [15], as done for SE.

First of all, the Provotorov's theory can be recalled to explain how the electron system (N_S electrons placed into a static magnetic field H_0) evolves in time under MW irradiation, provided that the EPR spectrum is inhomogeneously or homogeneously broadened and a fast spectral diffusion acts on it (that is, the mutual electron interaction is very fast) [190]. If the EPR spectrum is characterized by a center of gravity ω_0 and a width D, then the electron polarization is

$$P_S(\omega) = \tanh \frac{1}{2}(\omega_0 \alpha + (\omega - \omega_0)\beta_e), \tag{3.14}$$

and the total energy of the system is

$$U = -\hbar N_S \cdot \left[\frac{1}{4}\omega_0^2 \alpha + \frac{1}{4} D^2 \beta_e\right]. \tag{3.15}$$

The Provotorov theory assumes that the electron system is characterized by two parameters, α and β_e (Eq. 3.14), which can be identified as the two spin temperatures of the two blocks that form the electron system: these are the same electron reservoirs mentioned in the qualitative description. Now, if a

MW field H_1 is applied perpendicular to H_0 with a frequency ω_{MW}, the rate equation for the electron polarization is:

$$\frac{\partial P_S(\omega)}{\partial t} = -\pi\omega_1^2 g(\omega_{MW}) P_S(\omega) \tag{3.16}$$

where $\omega_1 = \gamma_e H_1$ and g is the inhomogeneous lineshape. By working on Eq. 3.16, it is possible to arrive at the two Provotorov equations:

$$\frac{\partial P_S(\omega)}{\partial t} = -2W(\omega_{MW}) \cdot \left[P_S(\omega) + \frac{1}{2}(\omega_{MW} - \omega_0)\left(1 - P_S(\omega)^2\right)\beta_e \right], \tag{3.17}$$

$$\begin{aligned} \frac{1}{2}D^2 \frac{\partial}{\partial t}\left(1 - P_S(\omega)^2\right)\beta_e = -2W(\omega_{MW}) \cdot (\omega_{MW} - \omega_0) \cdot \\ \cdot \left[P_S(\omega) + \frac{1}{2}(\omega_{MW} - \omega_0)\left(1 - P_S(\omega)^2\right)\beta_e \right], \end{aligned} \tag{3.18}$$

where $W(\omega) = \frac{1}{2}\pi\omega_1^2 g(\omega)$ is the MW-induced transition rate. These equations express the time evolution of the two parameters, α (which is included implicitly by using Eq. 3.14) and β_e, under MW irradiation. In the high temperature approximation $\left(1 - P_S(\omega)^2\right) \simeq 1$ and Eq. 3.17 and 3.18 become:

$$\omega_0^2 \frac{\partial \alpha}{\partial t} = -2W(\omega_{MW})\omega_0 \cdot [\omega_0\alpha + (\omega_{MW} - \omega_0)\beta_e], \tag{3.19}$$

$$D^2 \frac{\partial \beta_e}{\partial t} = -2W(\omega_{MW}) \cdot (\omega_{MW} - \omega_0) \cdot [\omega_0\alpha + (\omega_{MW} - \omega_0)\beta_e]. \tag{3.20}$$

The stationary solutions in the high temperature approximation are obtained by applying the MW field for a very long time and by putting $\partial\alpha/\partial t = 0$ and $\partial\beta_e/\partial t = 0$ in Eq. 3.19 and 3.20. The initial condition is that at the beginning of the DNP process the system is in thermal equilibrium and thus all the spin temperatures are equalized to a common value β_0. Then the solutions are:

$$\alpha_{\text{inf}} = \frac{(\omega_{MW} - \omega_0)^2}{D^2 + (\omega_{MW} - \omega_0)^2}\beta_0, \tag{3.21}$$

$$\beta_{e\,\text{inf}} = -\frac{\omega_0(\omega_{MW} - \omega_0) - D^2}{D^2 + (\omega_{MW} - \omega_0)^2}\beta_0. \tag{3.22}$$

The profile of $\beta_{e\,\text{inf}}$ as function of ω_{MW} displays two unresolved peaks with opposite signs (see Fig. 3.8), showing how TM cools the electron dipolar reservoir, as stated in the first step of the qualitative TM description. An extension to the Provotorov theory is given by Borghini [191], who introduces also the nuclear inverse spin temperature, obtaining an additional rate equation describing the time dependence of the nuclear polarization.

To explain the second step, it is crucial to understand how the thermal contact between electron dipolar and nuclear Zeeman reservoirs is realized. One can start with a simple model containing one nuclear spin I and two

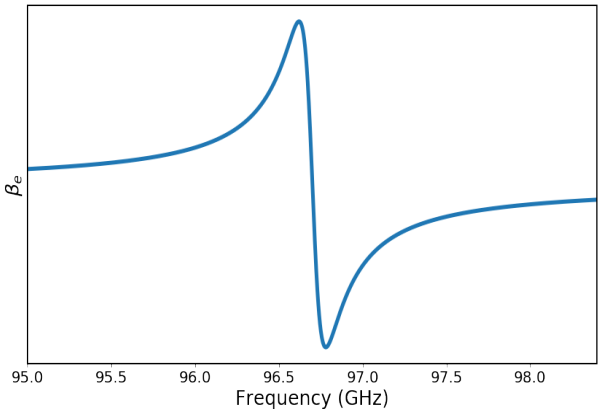

Figure 3.8: Electron dipolar inverse spin temperature over MW irradiation frequency from the steady state solution of the Provotorov equations.

electron spins S_i and S_j, placed into a static magnetic field H_0, directed along the $\hat{z}$ axis [15]:

$$\begin{aligned}\mathcal{H} = \hbar\omega_S^i S_z^i + \hbar\omega_S^j S_z^j - \hbar\omega_I I_z + \\ \hbar\frac{1}{4}D_{+-}\left(S_+^i S_-^j + S_-^i S_+^j\right) + \\ +\hbar\frac{1}{2}\left(\bar{\bar{A}}_{z-} S_z^i I_+ + \bar{\bar{A}}_{z+} S_z^i I_-\right),\end{aligned} \tag{3.23}$$

where the first three terms are the Zeeman interaction between H_0 of S_i, S_j and I, respectively. Then there are the mutual electron interaction and the hyperfine interaction, fourth and fifth term respectively, where truncation has removed the parts which do not induce transitions. By mean of a series of reference frames changes and truncation of negligible terms, similar to those applied on the SE hamiltonian, Eq. 3.23 becomes

$$\begin{aligned}\mathcal{H} = \hbar\left(\omega_S^j - \omega_S^i\right) S_z^i - \hbar\omega_I I_z + \hbar\frac{1}{2}D_{+-}\left(S_+^i + S_-^i\right) + \\ -\hbar\frac{1}{8}\left(S_+^i + S_-^i\right)\left(\bar{\bar{A}}_{z-} I_+ + \bar{\bar{A}}_{z+} I_-\right)\sin\theta\cos\theta + \\ -\hbar\frac{1}{8}\left(S_+^i - S_-^i\right)\left(\bar{\bar{A}}_{z-} I_+ - \bar{\bar{A}}_{z+} I_-\right)\sin\theta,\end{aligned} \tag{3.24}$$

whose eigenstates may be represented using the notation $|m_S^i, m_S^j, m_I\rangle$, where the quantum numbers refer to the electron and nuclear spin components along the $\hat{z}$ axis. The eight eigenstates are:

- a) $|+\frac{1}{2}, +\frac{1}{2}, -\frac{1}{2}\rangle$
- b) $|+\frac{1}{2}, +\frac{1}{2}, +\frac{1}{2}\rangle$
- c) $|+\frac{1}{2}, -\frac{1}{2}, -\frac{1}{2}\rangle$
- d) $|+\frac{1}{2}, -\frac{1}{2}, +\frac{1}{2}\rangle$

- e) $|-\frac{1}{2},+\frac{1}{2},-\frac{1}{2}\rangle$
- f) $|-\frac{1}{2},+\frac{1}{2},+\frac{1}{2}\rangle$
- g) $|-\frac{1}{2},-\frac{1}{2},-\frac{1}{2}\rangle$
- h) $|-\frac{1}{2},-\frac{1}{2},+\frac{1}{2}\rangle$

The non-diagonal terms of the hamiltonian of Eq. 3.24 can induce the following transitions:

- the term proportional to D_{+-} induces transitions of the type $|m_S^i, m_S^j\rangle = |+\frac{1}{2},-\frac{1}{2}\rangle \leftrightarrow |-\frac{1}{2},+\frac{1}{2}\rangle$, which are pure electronic flip-flop transition transitions, not leading to thermal contact, since $\omega_S^i \simeq \omega_S^i$;
- the term proportional to S_+I_+ and S_-I_- induces transitions triple spin flip transitions (type A) $|m_S^i, m_S^j, m_I\rangle = |+\frac{1}{2},-\frac{1}{2},+\frac{1}{2}\rangle \leftrightarrow |-\frac{1}{2},+\frac{1}{2},-\frac{1}{2}\rangle$, since $\omega_S^j \simeq \omega_S^i - \omega_I$;
- the term proportional to S_+I_- and S_-I_+ induces transitions triple spin flip transitions (type B) $|m_S^i, m_S^j, m_I\rangle = |+\frac{1}{2},-\frac{1}{2},-\frac{1}{2}\rangle \leftrightarrow |-\frac{1}{2},+\frac{1}{2},+\frac{1}{2}\rangle$, since $\omega_S^j \simeq \omega_S^i + \omega_I$.

Hence, triple spin flips transitions are responsible for the thermal contact between the electron dipolar reservoir and the nuclear Zeeman reservoir. The corresponding transition rates are:

$$W_A = \frac{1}{2}\pi \frac{|\frac{1}{2}\bar{\bar{A}}_{z+}|^2 \left(\frac{1}{2}D_{+-}\right)^2}{\omega_I^2} g\left(\omega_S^i - \omega_S^j - \omega_I\right), \tag{3.25}$$

and

$$W_B = \frac{1}{2}\pi \frac{|\frac{1}{2}\bar{\bar{A}}_{z+}|^2 \left(\frac{1}{2}D_{+-}\right)^2}{\omega_I^2} g\left(\omega_S^i - \omega_S^j + \omega_I\right), \tag{3.26}$$

To evaluate the nuclear polarization and thus the polarization transfer, one uses the following rate equation:

$$\frac{\partial P_I}{\partial t} = -\frac{1}{2} W_A \left(1 - P_S^i P_S^j\right) \left(P_I - \frac{P_S^i - P_S^j}{1 - P_S^i - P_S^j}\right), \tag{3.27}$$

and

$$\frac{\partial P_I}{\partial t} = -\frac{1}{2} W_B \left(1 - P_S^i P_S^j\right) \left(P_I + \frac{P_S^i - P_S^j}{1 - P_S^i - P_S^j}\right), \tag{3.28}$$

In a real system, there are N_S electrons and N_I nuclei, thus one has to sum over all spins available. Eq. 3.27 becomes:

$$\begin{aligned} \frac{\partial P_I}{\partial t} = -\frac{1}{2}\pi \frac{N_S}{N_I} \frac{|\bar{\bar{A}}|^2 M_2^0}{\omega_I^2} \int_{-\infty}^{+\infty} g(\omega)\, g(\omega - \omega_I)\, d\omega \cdot \\ \cdot \left(1 - P_S(\omega)\, P_S(\omega - \omega_I)\right) \cdot \left(P_I - \frac{P_S(\omega) - P_S(\omega - \omega_I)}{1 - P_S(\omega)\, P_S(\omega - \omega_I)}\right), \end{aligned} \tag{3.29}$$

and a similar formula holds for Eq. 3.28. By solving Eq. 3.29 in the absence of other interaction one finds that in a steady-state, since electrons and $\frac{1}{2}$ nuclei can always be characterized by inverse spin temperatures, electron and nuclear inverse spin temperatures are equalized by these triple spin flips, i.e. a good thermal contact is attained.

So far, it has been shown how the MW irradiation cools the electron dipolar reservoir (Provotorov theory) and how, consequently, nuclear spins are hyperpolarized (triple spin flips). To complete the TM framework, one has to add the nuclear relaxation since the hyperpolarized state is an out-of-equilibrium one. Nuclei can relax following mainly two channels: the first one is the direct relaxation, involving one electron and one nucleus, that has been introduced in the previous subsection; the second one is the indirect relaxation, involving two electrons and one nucleus. Just like in the SE, the same mechanism providing nuclear hyperpolarization is also a channel for nuclear relaxation in the absence of MW irradiation. For this indirect process, one can write:

$$\frac{\partial \beta_n}{\partial t} = -\frac{1}{\tau_{SSI}} \frac{N_S}{N_I} \frac{D^2}{\omega_I^2} \left(1 - P_S^2\right) \left(\beta_n - \beta_e\right), \tag{3.30}$$

where τ_{SSI} is the triple spin flips timescale:

$$\frac{1}{\tau_{SSI}} = \frac{1}{2}\pi \frac{|\bar{\bar{A}}|^2 M_0^2}{D^2} \int_{-\infty}^{+\infty} g\left(\omega_S\right) g\left(\omega_S - \omega_I\right) d\omega_S \tag{3.31}$$

It should be stressed that this process allows nuclei to relax exchanging energy with the electron dipolar reservoir (β_e appears in Eq. 3.30 and not β_L), which, in its turn, will relax exchanging energy with the lattice [111]. This is the reason for the "indirect" nomenclature, while the direct process transfers energy directly from the nuclei to the lattice. The direct and the indirect relaxation processes are competing in the TM so the total nuclear relaxation will be:

$$\frac{\partial \beta_n}{\partial t} = -\frac{1}{\tau_{SSI}} \frac{N_S}{N_I} \frac{D^2}{\omega_I^2} \left(1 - P_S^2\right) \left(\beta_n - \beta_e\right) - \frac{1}{T_{1n}} \left(1 - P_L P_S\right) \beta_n. \tag{3.32}$$

Depending on the magnitude of the relaxation times for this two processes, three different regimes can be distinguished:

- if $T_{1n}/\tau_{SSI} < 2|\bar{\bar{A}}|^2/D^2$ then the direct process dominates the relaxation and Eq. 3.32 becomes:

$$\frac{\partial \beta_n}{\partial t} = -\frac{1}{T_{1e}} \frac{2N_S}{N_I} \frac{|\bar{\bar{A}}|^2}{\omega_I^2} \left(1 - P_L^2\right) \beta_n. \tag{3.33}$$

  This condition is satisfied whenever the EPR spectrum is narrow enough or the electron spin-lattice relaxation is fast enough.

- if $T_{1n}/\tau_{SSI} < 1$ then the indirect process dominates the nuclear relaxation and the electron dipolar reservoir is strongly coupled to the lattice, so:

$$\frac{\partial \beta_n}{\partial t} = -\frac{1}{\tau_{SSI}} \frac{N_S}{N_I} \frac{D^2}{\omega_I^2} \left(1 - P_L^2\right) \beta_n. \tag{3.34}$$

  This case is called slow thermal mixing.

- if $T_{1n}/\tau_{SSI} > 1$ then the indirect process dominates the nuclear relaxation and the electron dipolar reservoir is only slowing relaxing towards the lattice, thus constituting a bottleneck for the flow of energy from nuclear spins to the lattice. Eq. 3.32 becomes:

$$\frac{\partial \beta_n}{\partial t} = -\frac{1}{T_{1e}} \frac{N_S}{N_I} \frac{D^2}{\omega_I^2} \left(1 - P_S^2\right) \beta_n. \tag{3.35}$$

  This case is called fast thermal mixing.

To finish the TM description, one can write a set of equation combining the MW dynamic cooling from Provotorov theory, the thermal contact by mean of three spin flips and the indirect nuclear relaxation [15]:

$$\begin{aligned} \frac{\partial P_S(\omega)}{\partial t} = -2W(\omega_{MW}) \cdot \left[P_S(\omega) + \frac{1}{2}(\omega_{MW} - \omega_0) \left(1 - P_S(\omega)^2\right) \beta_e \right] \\ -\frac{1}{T_{1e}} \left[P_S - P_L\right], \end{aligned} \tag{3.36}$$

$$\begin{aligned} \frac{1}{2} D^2 \frac{\partial}{\partial t} \left(1 - P_S(\omega)^2\right) \beta_e = -2W(\omega_{MW}) \cdot (\omega_{MW} - \omega_0) \cdot \\ \cdot \left[P_S(\omega) + \frac{1}{2}(\omega_{MW} - \omega_0) \left(1 - P_S(\omega)^2\right) \beta_e \right] + \\ + \frac{1}{2} D^2 \left(1 - P_S(\omega)^2\right) \cdot \left[\frac{1}{\tau_{SSI}} (\beta_n - \beta_e) - \frac{1}{T_{1e}} \beta_e \right], \end{aligned} \tag{3.37}$$

$$\frac{\partial \beta_n}{\partial t} = -\frac{1}{\tau_{SSI}} \frac{N_S}{N_I} \frac{D^2}{\omega_I^2} \left(1 - P_S(\omega)^2\right) (\beta_n - \beta_e). \tag{3.38}$$

Eqs. 3.36, 3.37 and 3.38 have analytical solutions in the high temperature approximation, where $\mathrm{P}_S \simeq \frac{1}{2}\omega_0\alpha$, $\mathrm{P}_L \simeq \frac{1}{2}\omega_0\beta_L$, $\left(1 - P_S(\omega)^2\right) \simeq 1$ and $\left(1 - P_L(\omega)^2\right) \simeq 1$ and they become:

$$\omega_0 \frac{\partial \alpha}{\partial t} = -2W(\omega_{MW}) \cdot \left[\omega_0\alpha + (\omega_{MW} - \omega_0)\beta_e\right] - \omega_0 \frac{1}{T_{1e}} \left[\alpha - \beta_L\right], \tag{3.39}$$

$$\begin{aligned} D^2 \frac{\partial \beta_e}{\partial t} = -2W(\omega_{MW}) \cdot (\omega_{MW} - \omega_0) \cdot \\ \cdot \left[\omega_0\alpha + (\omega_{MW} - \omega_0)\beta_e\right] + D^2 \cdot \left[\frac{1}{\tau_{SSI}} (\beta_n - \beta_e) - \frac{1}{T_{1e}} \beta_e \right], \end{aligned} \tag{3.40}$$

$$\frac{\partial \beta_n}{\partial t} = -\frac{1}{\tau_{SSI}} \frac{N_S}{N_I} \frac{D^2}{\omega_I^2} \left(\beta_n - \beta_e\right). \tag{3.41}$$

The steady-state solutions of Eqs. 3.39, 3.40 and 3.41 lead to the enhancement of the nuclear polarization in the TM process:

$$\frac{\beta_{e\infty}}{\beta_L} = -\frac{-2W\left(\omega_{MW}\right) T_{1e}\omega_0 \left(\omega_{MW} - \omega_0\right)}{-2W\left(\omega_{MW}\right) T_{1e}\left[\left(\omega_{MW} - \omega_0\right)^2 + D^2\right] + D^2}, \tag{3.42}$$

with the maximum value equal to

$$\frac{\beta_{e\infty}}{\beta_L} = -\frac{\omega_0 \left(\omega_{MW} - \omega_0\right)}{\left(\omega_{MW} - \omega_0\right)^2 + D^2}. \tag{3.43}$$

The DNP profile in the TM regime displays two opposite signs unresolved peaks (see Fig. 3.9) [27, 42, 111, 113, 115, 121, 182, 188, 192].

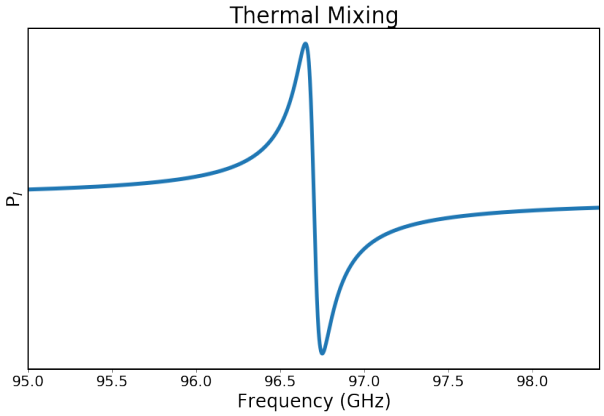

Figure 3.9: DNP profile in the TM regime.

The general solution of Eqs. 3.36, 3.37 and 3.38 requires numerical procedure [193, 194]. In the case of slow thermal mixing, the triple spin flip rate is slow, so the nuclear spins reach the polarization enhancement of Eq. 3.42, slowly, with a polarization time:

$$T_{POL} \simeq \tau_{SSI} \frac{N_I}{N_S} \frac{\omega_I^2}{D^2}, \tag{3.44}$$

while, in the fast thermal mixing regime, the triple spin flip rate is very fast and both β_n and β_e grow together to a stationary value with a timescale:

$$T_{POL} \simeq \frac{1}{2} T_{1e} \frac{N_I}{N_S} \frac{\omega_I^2}{D^2}. \tag{3.45}$$

The treatment has considered so far a very fast electron spectral diffusion, so that the whole EPR spectrum is involved in the DNP process. However, if the electron spectral diffusion is not so fast, only a portion of the spectrum will be

involved and an intermediate regime between SE and TM will take place: the so-called cross effect (CE), where triple spin flips hyperpolarize nuclear spins but it is difficult to define a common inverse spin temperature for the electron dipolar reservoir [24, 174, 188, 189], yielding a DNP profile similar to the TM one [30, 39, 88].

3.1.3 Numerical Simulations of the EPR Spectrum and Evidence for the Validity of a Spin Temperature Approach

Since the DNP process relies on a transfer of polarization from electrons to nuclei, it is fundamental to study the structure of the EPR spectrum, as well as how it changes by considering different polarizing agents and how it is affected by the MW irradiation in DNP experiments. If we place an electron system into a magnetic field H_0, we can define the electron Larmor frequency as $\omega_S{=}\gamma_e{\cdot}H_0$, that is the frequency at which all electrons ideally resonates. However, in real systems, several factors, like electron g-factor anisotropy and mutual electron interactions, determine a distribution of resonance frequencies over a narrow or broad interval, $g(\omega)$, which represents the fraction of electrons resonating at a given frequency and satisfying the normalization condition:

$$\int_{-\infty}^{+\infty} g\left(\omega\right) d\omega = 1. \tag{3.46}$$

As stated before, the EPR linewidth plays a key role into the DNP process with the inhomogeneous broadening, caused by electron g-factor anisotropy, the hyperfine interaction and the superhyperfine interaction and extending up to hundreds of MHz, and the homogeneous broadening, caused by the mutual interaction between electrons and the mutual interaction between nuclear spins and ranging from tens of KHz to hundreds of MHz [167]. Thanks to Eq. 3.1 and 3.13, the choice of the paramagnetic center and of its concentration determines which mechanism will transfer the polarization from electrons to nuclei.

There are three main groups of polarizing agents used in DNP experiments [22, 23]:

- narrow EPR spectrum free radicals, like BDPA and trityls;
- the nitroxides;
- the paramagnetic metal ions.

The BDPA (1,3-bisdiphenylene-2-phenyl allyl) radical [195, 196] has a very narrow (down to 20 MHz) EPR spectrum mainly due to hyperfine interaction with the protons over a large range (up to 9 T) of static fields [197], is chemically stable but has a low water solubility, thus preventing many biological

applications. The trityls (triphenylmethyl) are among the most studied free radicals in DNP experiments [115, 198], in particular OX063, due to chemical stability, high water solubility, narrow linewidth (50 MHz at 5 T, scaling linearly with H_0) due to very small inhomogeneous broadening and very high DNP performances [29, 88, 199–201]. These two families have been used to achieve mainly SE DNP [199], always depending on the nucleus of interest and on the static field applied. The nitroxides family covers free radicals where the free electron is localized at the NO group (the one used in this thesis is TEMPO, 2,2,6,6-tetramethyl-1-piperidiny-1-oxyl) [87, 95, 202]: they have a broad NMR spectrum, that is dominated by the electron g-factor anisotropy, granting a sizeable linewidth and efficient CE or TM processes for DNP. They show also good solubility in aqueous and organic compounds and can be tailored to produce many derivatives for a plenty of applications. In order to match the CE or TM conditions, one can vary the nitroxides concentration or synthesize the so-called biradical nitroxides (for example TOTAPOL) [30, 118, 178, 203, 204], which are molecules with two free electronic spins that have demonstrated promising DNP performances [22]. Since metal ions display one or more unpaired electrons (for example Gd and Cr), they have been sometimes used as polarizing agents for DNP applications [24, 39, 110, 205], even if difficulties arise due to the very broad EPR spectrum (very high electron g-factor anisotropy) and the DNP performances are much lower with respect to the free radicals. Furthermore, many of them are toxic for human health and thus not suitable for biomedical applications.

Since the choice of the polarizing agent and of its concentration determines the mechanism underlying DNP, it is relevant to study the change in the EPR spectrum under MW irradiation. In the case of SE, the DNP is realized by mean of two-body interactions, which do not imply communication between electron spins: this means that the effect of the MW irradiation on the EPR spectrum is localized over a small interval centered around ω_{MW}. In particular, MW will saturate a small portion of the EPR spectrum, a phenomenon called hole burning. As the MW power grows, the hole gets larger and deeper. Suppose the EPR spectrum is the sum of many homogeneous packets located at different frequencies. From Sec. 3.1.1, MW irradiation at ω_{MW} will induce transitions at a rate:

$$W_{HB}(\omega) = \frac{1}{2}\pi\omega_1^2 \cdot h_e(\omega - \omega_{MW}), \tag{3.47}$$

where h is the lorentzian lineshape of the homogeneous packet containing ω_{MW}. The rate equation for the electronic polarization is:

$$\frac{\partial P_S(\omega, t)}{\partial t} = -2W_{HB}P_S(\omega, t) \tag{3.48}$$

and the solution

$$P_S(\omega, t_0) = P_S^0 \cdot \exp(-2W_{HB}t_0), \tag{3.49}$$

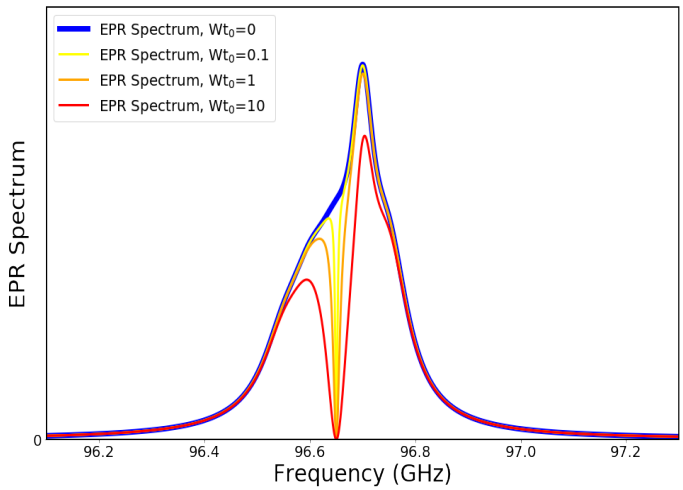

Figure 3.10: Hole burning in EPR spectra for different MW powers, as predicted from solid effect theory. The hole burning gets larger as the MW power increases.

An example of hole burnings, for different MW power, is given in Fig. 3.10. On the other hand, it is well established that the TM is a collective process and in this case the MW irradiation effects are not limited to a tiny portion of the spectrum but extends, thanks to the electron spectral diffusion, almost to all electrons. In the TM regime the EPR spectrum undergoes a sign inversion at ω_{MW} (see Fig 3.11). This is quantified by the Provotorov theory (From Sec. 3.1.2), which yields:

$$P_S(\omega) = P_S^0 \cdot \frac{1}{2}(\omega_{MW} - \omega) \frac{\omega_0(\omega_{MW} - \omega_0)}{D^2 + (\omega_{MW} - \omega_0)^2} \beta_0, \tag{3.50}$$

It must be pointed out that, for all MW powers explored, the TM theory always leads to sign inversion in the irradiated EPR spectrum [206].

However, the abovementioned calculation do not provide a complete theoretical description that is also able to describe some unexpected experimental features. As previously discussed (Sec. 3.1.2) the Provotorov and Borghini theories postulate the existence of the electron dipolar spin-temperatures but do not justify it theoretically nor they take into account explicitly the magnetic dipolar interactions between electrons during calculation. On the other hand, Eq. 3.14 predicts a sign inversion in the electron polarization, corresponding to a population inversion in the electron Zeeman levels, with electron spins becoming aligned parallel to H_0. The sign inversion has been observed experimentally [207], but other experiments, carried out in typical TM conditions, displayed no inversion in the EPR spectrum [208–210], while showing a huge depolarization of the EPR spectrum, i.e. a very huge hole burning which is not consistent with the localized one in Fig. 3.10 nor with Fig. 3.11. A system of rate equations based on an electron spectral diffusion has been introduced to explain this huge depolarization [210]: the spectral diffusion is responsible

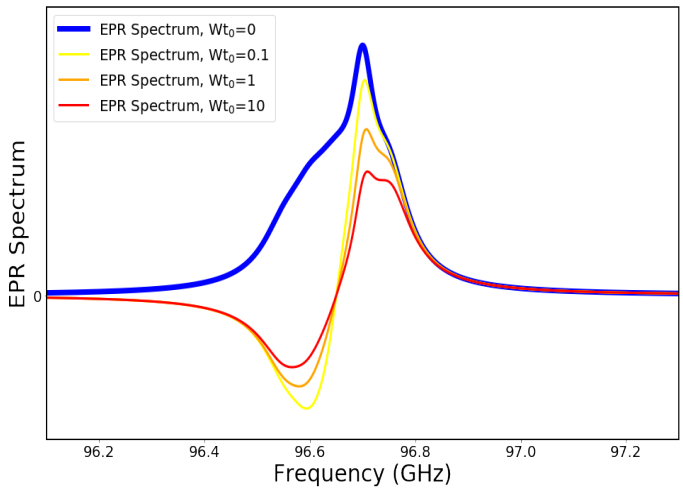

Figure 3.11: Inversion in EPR spectrum for different MW powers, as predicted from Provotorov theory. Sign inversion is always observed for all MW powers.

for flip-flop transitions between electrons but yet does not have a clear microscopic origin. Furthermore, this argument is used to invalidate the spin temperature concept in TM regimes [210]. It is thus necessary to numerically simulate the shape of the EPR spectrum in typical DNP conditions, investigating in particular the role of the electron dipolar interaction and of the MW power quantitatively as well as verifying the validity of the spin-temperature approach. An exact computation of the EPR spectrum will be presented in a scenario where electrons can interact with each other by magnetic dipolar interaction, whose strength will change depending on the electron concentration.

Starting Model

The starting model [211] contains N electron spins placed into a magnetic field H_0 directed along the $\hat{z}$ axis, described by the hamiltonian:

$$\mathcal{H}_{\mathcal{S}} = \sum_{i=1}^{N} \hbar \left(\omega_S + \Delta_i\right) \hat{S}_z^i + \mathcal{H}_{\text{dip}}, \tag{3.51}$$

where the novelty is the addition of a term describing the dipolar electron interaction in a system of electrons arranged on a cubic lattice. The Δ_i's describe the inhomogeneous shift of the ω_S. Since we are studying DNP, the large magnetic field employed allows to treat the electron dipolar interaction in its truncated form:

$$\mathcal{H}_{\text{dip}} = \sum_{i<j} U_{ij} \left[4\hat{S}_z^i \hat{S}_z^j - (\hat{S}_+^i \hat{S}_-^j + \hat{S}_-^i \hat{S}_+^j)\right] \tag{3.52}$$

where $U_{ij} = \mu_0 \hbar^2 \gamma_e^2 (1 - 3\cos^2\theta_{ij})/(16\pi |r_{ij}|^3)$, μ_0 is the vacuum magnetic permeability, γ_e is the electron gyromagnetic ratio and $\hbar\mu_0\gamma_e^2/16\pi$ is $81.7 \times 2\pi$

GHz [3]. r_{ij} is the distance between the spin i and the spin j while θ_{ij} is the angle between r_{ij} and H_0. Next, the hamiltonian describing MW interaction with the electron spins is:

$$\mathcal{H}_{\mathrm{MW}}(t) = 2\hbar\omega_1 \sum_i \hat{S}_x^i \cos(\omega_{MW} t), \tag{3.53}$$

which is much smaller than the previous term of the total hamiltionian $\mathcal{H}_{\mathcal{S}}$ since ω_1 is in the hundreds of KHz range. Then it is possible to relate different reference frames, the laboratory one, with its own density matrix ρ, and the rotating one, with density matrix ρ^{rot}, at a frequency ω_{MW}. The relationship between the two density matrix is:

$$\rho^{\mathrm{rot}} \equiv e^{\mathbf{i}\hat{S}_z\omega_{MW}t}\rho e^{-\mathbf{i}\hat{S}_z\omega_{MW}t}. \tag{3.54}$$

When considering the time evolution of ρ^{rot}, one can neglect the fast oscillating terms and focus on the time independent one and one can write the Liouville equation:

$$\frac{d}{dt}\rho^{\mathrm{rot}} = -\frac{\mathbf{i}}{\hbar}[\mathcal{H}^{\mathrm{rot}}, \rho^{\mathrm{rot}}] \tag{3.55}$$

The hamiltonian in the rotating frame now reads:

$$\mathcal{H}^{\mathrm{rot}} = \mathcal{H}_{\mathcal{S}} - \hbar\omega_{MW}\sum_i \hat{S}_z^i + \hbar\omega_1 \sum_i \hat{S}_x^i. \tag{3.56}$$

Master Equations

Eq. 3.55 describes the time evolution of the system by evaluating the change in the density matrix components, which are 4^N, thus limiting the maximum number of electron that can be used in the simulation. However, since the electron spin-spin relaxation rate is much faster than the electron spin-lattice relaxation rate (in typical DNP conditions), then the Hilbert approximation can be used [211–214], allowing to evaluate the time evolution of the spin system as the time evolution of the diagonal element of ρ^{rot} (which are called p_n and are equal to $\equiv \rho^{\mathrm{rot}}_{nn}$) on the basis of eigenstates of $\mathcal{H}_{\mathcal{S}}$ (which are called $|n\rangle$). Then we have a set of rate equations for p_n, representing the occupation probability of $|n\rangle$.

$$\frac{dp_n}{dt} = \sum_{n'\neq n} W_{n'\to n}p_{n'} - W_{n\to n'}p_n \ . \tag{3.57}$$

By considering the transition between two eigenstates $|n\rangle$ and $|n'\rangle$ the total transition rate ($W_{n\to n'}$) is the sum of two terms:

$$W^{\mathrm{latt}}_{n,n'} = \frac{2h_\beta(\Delta\epsilon_{n,n'})}{T_{1e}} \sum_{j=1}^{N}\sum_{\alpha=x,y,z} |\langle n|\hat{S}^j_\alpha|n'\rangle|^2, \tag{3.58}$$

$$W_{n,n'}^{\mathrm{MW}} = \frac{4\omega_1^2 T_{2e} |\langle n| \sum_{j=1}^{N} \hat{S}_x^j |n'\rangle|^2}{1 + T_{2e}^2 (|\epsilon_n - \epsilon_{n'}|/\hbar - \omega_{MW})^2}, \tag{3.59}$$

where the former refers to transitions induced by the spin-lattice relaxation processes and the latter refers to the transitions induced by MW irradiation. The function $h_\beta(x) = e^{\beta x}/(1 + e^{\beta x})$ assures the detailed balance of the transitions and the convergence to Gibbs equilibrium at the lattice temperature β_L^{-1}, while ϵ_n's are the eigenvalues corresponding to $|n\rangle$.

Numerical Implementation

The numerical simulation employs 12 electrons which are arranged to form a cubic lattice, where, by varying the the lattice step, it is possible to change the electron concentration. Two concentrations have been analyzed: the first with lattice step equal to 114 Å and the second with 54 Å, corresponding to 1.5 and 15 mM, respectively, which are typical electron concentrations used in real DNP experiments. As it will be presented below, the exact topology of the spins is not important, provided that they are homogeneously distributed. The Δ_i's are chosen for simplicity from a gaussian distribution centered at ω_S and with width $\Delta\omega_S$. The other parameter which are fixed are reported in Table 3.1 and refer to a sample of pyruvic acid doped with trytil radical which is known to display thermal mixing at 1.2 K and in 3.35 T from previous experiments [113, 120]. The written code performs the following steps:

T_{1e} (s)	T_{2e} (s)	ω_S (GHz)	$\Delta\omega_S$ (GHz)	ω_{MW} (GHz)	β_L (K^{-1})
1	10^{-6}	93.9	0.108	93.8685	0.04

Table 3.1: Parameters of the simulation: T_{1e} and T_{2e} are the longitudinal and transverse electron relaxation times, ω_S is the electron Larmor frequency, $\Delta\omega_S$ the electron linewidth in absence of dipolar interaction and β_L^{-1} is the lattice temperature.

- diagonalizes $\mathcal{H}_\mathcal{S}$, computing eigenvalues ϵ_n and eigenvectors $|n\rangle$;
- evaluates the total electron magnetization $s_{z,n} = \langle n| \hat{S}_z |n\rangle$ with $\hat{S}_z = \sum_i \hat{S}_z^i$;
- computes the transition rates from Eq. 3.58 and 3.59;
- evaluates the occupation probabilities p_n^{stat} from the stationary solution of the equation system 3.57, introducing the constraint $dp_n\ dt{=}0$;
- repeats the whole procedure 600 times allowing for numerical average over the local magnetic fields Δ_i.

EPR Spectrum Evaluation

In the simplest EPR pulse experiment the electron magnetization is rotated from the $\hat{z}$ axis to the $\hat{xy}$ plane by applying a $\frac{\pi}{2}$ pulse. If one assumes that the final magnetization is along the $\hat{y}$ axis, then $\hat{U}_{\pi/2}\hat{S}^i_z\hat{U}_{-\pi/2} = \hat{S}^i_y$ where $\hat{U}_\theta = e^{i\theta\hat{S}_x}$ is the rotation of an angle θ around the $\hat{x}$ axis and $\hat{S}_x = \sum_i \hat{S}^i_x$. After the rotation the density matrix of the system changes:

$$\rho \longrightarrow \rho_{\pi/2} \equiv \hat{U}_{\pi/2}\rho\hat{U}_{-\pi/2}, \tag{3.60}$$

After the $\frac{\pi}{2}$ pulse the i-th spin will rotate in the $\hat{xy}$ plane with a frequency equal to $\omega_i = \omega_S + \Delta_i$ and it will probe a dephasing due to the dipolar interaction with the other spins. The polarization component of the i-th spin in the plane $\hat{xy}$ will decay over a timescale equal to T_{2e}, so that:

$$\begin{bmatrix} P^i_{x,\pi/2}(\tau) \\ P^i_{y,\pi/2}(\tau) \end{bmatrix} = \begin{bmatrix} -\sin(\omega_i\tau) \\ \cos(\omega_i\tau) \end{bmatrix} P^i_z(\tau = 0)e^{-\tau/T_{2e}} \ . \tag{3.61}$$

where $P^i_z(\tau = 0)$ is the initial polarization along the $\hat{z}$ axis. In this picture, where the dipolar interaction has been treated only implicitly, the EPR spectrum is then equal to:

$$f_i(\omega) = \mathrm{Re}\left[\int_0^\infty \frac{dt}{\pi} g_i(\tau)e^{-i\omega\tau}\right] = \frac{T_{2e}P^i_z/\pi}{T^2_{2e}(\omega - \omega_i)^2 + 1}, \tag{3.62}$$

where the following function is used:

$$g_i(\tau) \equiv P^i_{y,\pi/2}(\tau) - \mathbf{i}P^i_{x,\pi/2}(\tau). \tag{3.63}$$

However, since the aim of the numerical calculation is to treat explicitly the electron dipolar interaction, T_{2e} only accounts for the MW effect, as results from Eq. 3.59, and Eq. 3.62 is modified. For time much shorter than T_{1e} the time evolution of the system can be efficiently described by Eq. 3.56 where the effect of the electron spin-lattice relaxation is not accounted for. Then the i-th spin polarization is

$$P^i_{\alpha,\pi/2}(\tau) = 2\mathbf{Tr}[\hat{S}^i_\alpha(\tau)\rho_{\pi/2}] \tag{3.64}$$

where the Heisenberg picture for the time-evolution is used, that is $\hat{S}^i_\alpha(\tau) = e^{\mathbf{i}\hat{H}_S\tau}\hat{S}^i_\alpha e^{-\mathbf{i}\hat{H}_S\tau}$. Thus Eq. 3.63 becomes:

$$g_i(\tau) = -2\mathbf{i}\mathbf{Tr}[\hat{S}^i_+(\tau)\rho_{\pi/2}] \ . \tag{3.65}$$

Since $e^{\mathbf{i}\pi\hat{S}^i_x/2} = 2^{-1/2}(1 + 2i\hat{S}^i_x)$ and $[\hat{S}_z, \hat{H}_S] = 0$ (because only the terms conserving the total magnetization are retained) Eq. 3.65 transforms to

$$g_i(\tau) = \mathbf{Tr}[\hat{S}^i_+(\tau)\hat{S}^i_-(0)\rho] - \mathbf{Tr}[\hat{S}^i_-(0)\hat{S}^i_+(\tau)\rho] \ . \tag{3.66}$$

which is the spin-spin time correlation function. Adding the hypothesis of fast dephasing, we can express the density matrix as diagonalized on the basis of the eigenstates $\mathcal{H}_\mathcal{S}$ [211, 212]

$$\rho = \sum_n p_n \left|n\right\rangle \left\langle n\right| \ . \tag{3.67}$$

so that Eq. 3.66 becomes

$$g_i(\tau) = \sum_{n,m} (p_n - p_m) e^{\mathbf{i}\tau(E_n - E_m)} |\left\langle n\right| \hat{S}^i_+ \left|m\right\rangle|^2 \ . \tag{3.68}$$

Generalizing Eq. 3.62 one gets

$$f(\omega) = \frac{1}{N} \sum_i \mathrm{Re}\left[\int_0^\infty \frac{dt}{\pi} g_i(\tau) e^{-i\omega\tau - \eta\tau} \right] \ . \tag{3.69}$$

where the parameter η is a small cutoff necessary to obtain a smooth spectrum while the average is computed over all available spins. Now, by inserting Eq. 3.68 into 3.69

$$f(\omega) = \frac{\eta}{N\pi} \sum_{n,m} \frac{(p_n - p_m) \sum_i |\left\langle n\right| S^i_+ \left|m\right\rangle|^2}{(\omega - (\epsilon_n - \epsilon_m))^2 + \eta^2} \tag{3.70}$$

Here, if $\eta \to 0$, for a finite value N the EPR spectrum is just the sum of discrete peaks which are located at frequency $\omega = \frac{1}{\hbar}\epsilon_n - \epsilon_m$: it is clear that by letting $N \to \infty$ then the EPR spectrum becomes smooth, since the number of peaks grows exponentially with N. In the numerical calculation, $\eta \to 0$ but the spectrum is integrated over a small interval $\delta\omega = \Delta\omega_e/150$: $\tilde{f(\omega)} = \frac{1}{\delta\omega} \int_\omega^{\omega+\delta\omega} f(\omega)$. This quantity $\tilde{f}(\omega)$ is then averaged over 600 random realizations of the fields Δ_i (from the gaussian distribution) to obtain the final EPR spectrum. In the absence of interaction Eq. 3.70 simplifies to

$$f(\omega) = \frac{1}{N} \sum_i P^i_z \delta(\omega - \omega_i) \tag{3.71}$$

In both cases (explicitly accounting for interaction or not) the area subtended by the EPR spectrum is the total magnetization.

Results and Discussion

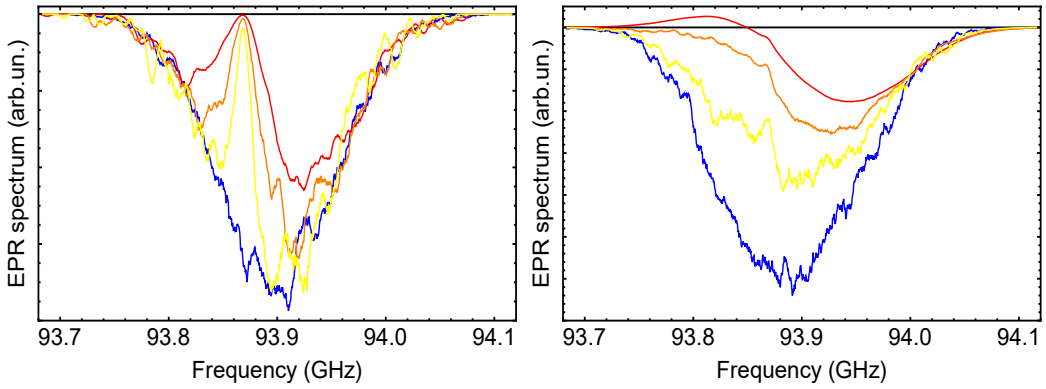

(a) (b)

Figure 3.12: Numerical EPR spectrum (from exact computation) under MW irradiation for the two free radical concentrations of 1.5 mM (a) and 15 mM (b) as obtained from Eq. 3.70 with $p_n = p_n^{stat}$. MW intensities are : $\omega_1 = 0$ GHz (black line),$\omega_1 = 0.625 \times 10^{-5}$ GHz (yellow line), $\omega_1 = 0.125 \times 10^{-4}$ GHz (orange line),$\omega_1 = 0.25 \times 10^{-4}$ GHz (red line).

As shown in Fig. 3.12 in the absence of MW the EPR spectrum at C = 15 mM (high concentration) is only slightly broader than the one at C = 1.5 mM (low concentration), whereas their gaussian shape is a consequence of the choice of Δ_i's from the gaussian distribution. Upon irradiation with MW the two EPR spectra change in a completely different way. **In the low concentration case**, Fig. 3.12a, **a hole burning appears at ω_{MW} and it becomes broader and deeper as the MW power is increased: one can associate this case with the SE regime** since it is in agreement with theory.

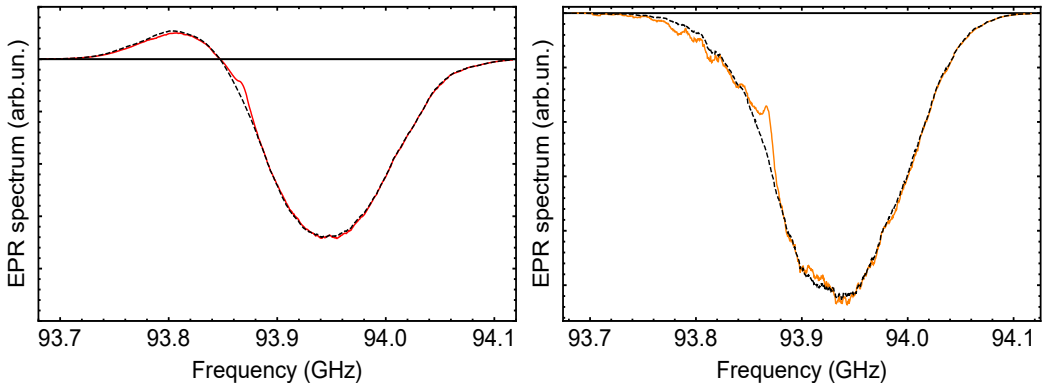

(a) (b)

Figure 3.13: Comparison between the numerical EPR spectrum (from exact computation, with $p_n = p_n^{stat}$ in Eq. 3.70, continuous line) with the one obtained through the spin-temperature approach (with $p_n = p_n^{ans}$ in Eq. 3.70, dashed line) at concentration C= 15 mM. a) MW intensity: $\omega_1 = 0.25 \times 10^{-4}$ GHz. b) $\omega_1 = 0.125 \times 10^{-4}$ GHz.

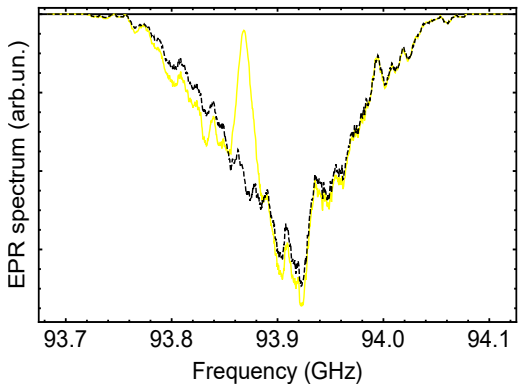

Figure 3.14: Comparison between the numerical EPR spectrum (from exact computation, with $p_n = p_n^{stat}$ in Eq. 3.70, continuous line) with the one obtained through the spin-temperature approach (with $p_n = p_n^{ans}$ in Eq. 3.70, dashed line) at concentration C= 1.5 mM. MW intensity: 0.625×10^{-5} GHz.

On the other hand, **in the high concentration case**, Fig. 3.12b, **low MW power is able to affect almost the whole EPR spectrum producing a huge depolarization** (similar to the one observed in Ref. [210]), while **for sufficiently high MW power the sign inversion, predicted by Provotorov and Borghini, appears. This case corresponds to the TM regime**, where the strong mutual interaction between electrons spreads the MW effect across the whole spectrum. However, another step is required to check the validity of the spin temperature approach.

If one assumes the Provotorov theory to hold then two parameters, β_e and ω_0, must exist such that one can write:

$$p_n^{stat} \sim p_n^{ans} \equiv \frac{e^{-\beta_s(\epsilon_n - \omega_0 s_{z,n})}}{\mathcal{Z}}, \tag{3.72}$$

i.e. such that the occupation probabilities can be evaluated through the spin temperature approach, where $\mathcal{Z} = \sum_n e^{-\beta_s(\epsilon_n - \omega_0 s_{z,n})}$ is the partition function. Now, to fix these two parameters, one can impose that the total energy and the total magnetization are the same for the "exact" case (with $p_n = p_n^{stat}$) and for the "spin temperature" case (with $p_n = p_n^{ans}$):

$$\langle \mathcal{H}_S \rangle = \sum_n p_n^{stat} \epsilon_n = \sum_n p_n^{ans} \epsilon_n \ , \tag{3.73a}$$

$$\langle \hat{S}_z \rangle = \sum_n p_n^{stat} s_{z,n} = \sum_n p_n^{ans} s_{z,n} \ . \tag{3.73b}$$

For sufficiently large N, β_e and ω_0 do not change between different realizations while for N = 12 they fluctuate. Thus the code evaluates the couple of parameters for every realization solving Eqs. 3.73, then the EPR spectrum is computed using Eq. 3.70 and putting $p_n = p_n^{ans}$. In particular this is done clearly for high concentration case and for two different MW power, as it is depicted in Fig. 3.13. **The spin temperature approach can well reproduce**

the exact EPR spectrum for C = 15 mM: moreover, it can reproduce both the huge depolarization, appearing at low MW power, and the sign inversion, for high MW power, confirming that this case can be associated with the TM regime, with β_e reaching mK^{-1} values. For C = 1.5 mM (see Fig. 3.14) the spin temperature approach is not able to reproduce the hole burning, demonstrating, as expected, that **in the SE regime no electron spin temperature can be defined to describe the system**.

To compare these theoretical simulations with experimental data, one can go back to Ref. [210], where the EPR spectrum of pyruvic acid dope with trityls or TEMPOL is measured under MW irradiation. In particular, at T = 2.7 K, a huge depolarization appears in the irradiated spectrum and it is explained by resorting to a macroscopic electron spectral diffusion, without providing any detail about its microscopic origin. Since the model presented here evaluates the EPR spectrum of a system of interacting electrons in typical DNP conditions and a huge depolarization is found both within the exact computation and the spin temperature approach, it can be concluded that the electron spectral diffusion in Ref. [210] is generated by the magnetic dipolar interaction between electrons. Thus the magnitude of the dipolar interaction plays a fundamental role in determining the EPR spectrum shape under MW irradiation and, more in general, the DNP mechanism (SE or TM) that takes place. The crossover between one regime and the other is the many body localization which has been recently identified with the quantum thermalization [211]. The T_{1e} and T_{2e} have been kept constant at both concentration, even if they are known to slightly change, in order to focus exclusively on the role of the electron mutual interaction.

A final remark concerns the choice of arranging the 12 electrons on a cubic lattice in the simulations. In real DNP samples, amorphous phase is needed to allow for homogeneous free radical distribution and good DNP performances, whereas the polycrystalline samples are known to badly hyperpolarize with DNP [42, 117]. However, in these simulations **an ordered (and thus crystalline) arrangement of free electrons still leads to low spin temperatures in the TM framework, leading to good DNP performances**. The conclusion is that to efficiently hyperpolarize substrates through DNP the free radicals must be homogeneously distributed (no matter if regularly on a cubic lattice or randomly). **Only amorphous phase, however, can ensure this homogeneous distribution since in polycrystalline samples, the substrates form grains and the free radicals are forced to accumulate between one grain and the other, thus creating radical-rich and radical-poor regions**, as confirmed by theory [211, 215] and by DNP [113] and EPR [117] experiments.

3.1.4 Nuclear Spin Diffusion

Both SE and TM rely on the hyperfine interaction (two o three body, respectively) to transfer the polarization from electrons to nuclei under MW

irradiation. However, this hyperfine interaction is dominated by the magnetic dipolar interaction whose strength scales with $1/r^3$, where r is the distance between the interacting spins. Thus the free electrons will interact only with the neighbouring nuclear spins, while the nuclear hyperpolarization achieved in DNP experiments is a macroscopic quantity, which involves all the nuclear spins [15]. To explain how the hyperpolarization is spread throughout the whole sample it is crucial to refer to the nuclear magnetic dipolar interaction, whose hamiltionian in case of two nuclear spins k and l interacting involves terms of the form:

$$\mathcal{H}_{nn} = \frac{1}{4} C_{+-} \left(I_+^k I_-^l + I_-^k I_+^l \right). \tag{3.74}$$

In Eq. 3.74, only the part of the hamiltonian able to induce flip-flop transitions (where nuclear spin are flipped in opposite directions) has been considered. These transitions tends to equalize the polarization of the two interacting spins, provided that their Larmor frequencies are close. However, since this is again a dipolar interaction, it involves only neighbouring spins: a series of this nuclear flip-flop transitions are needed to spread the polarization throughout the sample. The sequence of these transitions is a three-dimensional random walk that is called nuclear spin diffusion and which obeys a diffusion law, allowing one to define the diffusion tensor $\mathcal{D}$ [15, 216]. Generally, $\mathcal{D}$ is isotropic when considering a glassy sample. Now, it is possible to divide the nuclear spins in two groups: the local spins, which are close to the free electrons, and the bulk spins, which are far away instead. The local spin communicate directly with the free electrons but cannot partecipate in the diffusion process, due to the strong paramagnetic shift in their Larmor frequencies. Local and bulk spins are separated by the diffusion barrier (see Fig. 3.15), which is the surface satisfying the conditions:

$$r \simeq \left(1 - 3\cos\theta^2\right)^{\frac{1}{3}}, \tag{3.75}$$

where θ is the angle between the static magnetic field and r. Outside the diffusion barrier defined by Eq. 3.75 the polarization transfer to the nuclear spins may take place in two ways: directly, i.e. with direct interaction with the free electron, or indirectly, by mean of the spin diffusion. This allows to define a diffusion boundary (see Fig. 3.15):

$$r \simeq \left(\frac{3\cos\theta^2 \sin\theta^2}{4\mathcal{D}} \right)^{\frac{1}{4}}. \tag{3.76}$$

Inside the diffusion barrier, there is no spin diffusion, between the diffusion barrier and the diffusion boundary the direct process spreads polarization faster than the nuclear spin diffusion, outside the diffusion boundary the nuclear spin diffusion is faster than the direct process.

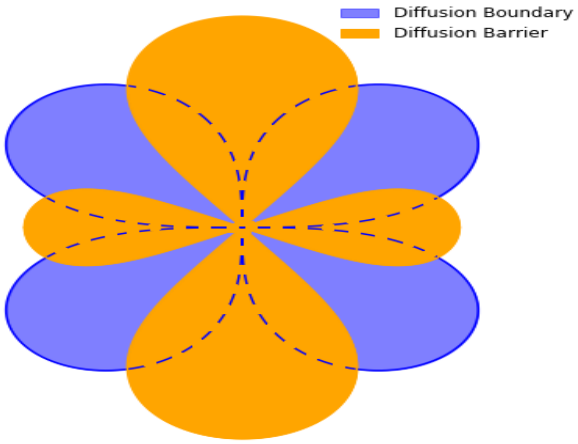

Figure 3.15: Projection of diffusion barrier (orange) and boundary (blue).

3.1.5 Nuclear Spin-lattice Relaxation Temperature Dependence

This subsection deals with the temperature dependence of the nuclear spin-lattice relaxation rate. Even if in the previous it has been stated that in the low-temperature range the nuclei relax through direct and indirect processes due to hyperfine interaction, nothing has been said about any specific temperature dependence. Furthermore, for possible MI application, it is crucial to analyze also the nuclear relaxation in the high-temperature range, in particular at room temperature, to observe how long the system retains the hyperpolarization once heated.

In general, in the presence of magnetic field fluctuations described by an exponential decaying correlation function, the nuclear spin-lattice relaxation rate is given by [217]:

$$\frac{1}{T_{1n}} = \frac{\gamma_n^2}{2} \left\langle \Delta h_\perp^2 \right\rangle \frac{2\tau_C}{1 + \omega_I^2 \tau_C^2}, \tag{3.77}$$

where $\langle \Delta h_\perp^2 \rangle$ is the mean square amplitude of the magnetic fluctuations and τ_C the related correlation time.

In the low-temperature range, i.e. when $1.60 < \mathrm{T} < 4.20$ K, the molecular dynamics is frozen, so one would expect that $1/T_{1n}$ vanishing. However, as discussed below, the samples treated here are not crystalline: they are synthesized in an amorphous phase to allow the free radical distribution to be the most homogeneous possible. This amorphous phase is characterized by low frequency, glassy modes which can modulate the hyperfine interaction driving the nuclear relaxation. Single atoms or group of atoms can fluctuate between several quasi-equilibrium states corresponding to different local arrangements. The single local energy level structure can be described as an asymmetric double quantum well, with two close energy states separated by an energy barrier E_G [218–222]. If the system undergoes a transition from one state to the other,

then the change in the local arrangement of the structure will cause hyperfine field fluctuations. The single barrier is characterized by a correlation time τ_C (due to thermal activation) given by the Arrhenius law:

$$\tau_C = \tau_0 \exp\left(\frac{E_G}{T}\right), \tag{3.78}$$

where τ_0 is the infinite temperature correlation time. However, due to the disordered nature of the amorphous phase, each sample has a distribution of E_G resulting in a distribution of correlation times [223, 224], whose inverse mean value is:

$$\left\langle \frac{1}{\tau_C} \right\rangle = \int \frac{1}{\tau_C\left(T\right)} p\left(E_G\right) dE_G, \tag{3.79}$$

where $\mathrm{p}(E_G)$ is the energy barrier distribution. It has been recognized that this distribution should be broad and continuous and that its shape affects the $1/T_{1n}$ temperature dependence [225, 226]. In the slow motion regime and in the presence of a distribution $\mathrm{p}(E_G)$ Eq. 3.77 becomes:

$$\frac{1}{T_{1n}} = \frac{\gamma_I^2}{2} \left\langle \Delta h_\perp^2 \right\rangle \frac{1}{\omega_I^2} \left\langle \frac{1}{\tau_C} \right\rangle. \tag{3.80}$$

On the other hand, in the high-temperature range the molecular dynamics is activated and one expects a peak in $1/T_{1n}$ temperature dependence associated with the slowing down of the magnetic fluctuations whose frequency approaches the nuclear Larmor frequency [227]. Consequently, in principle, one may use Eq. 3.77 with the correlation time given by Eq. 3.78, with an energy barrier to the molecular motion which is E_A and an infinite temperature correlation time τ_1. However, amorphous sample are often characterized by a distribution of E_A ($\mathrm{P}(E_A)$), which leads to a distribution of $1/T_{1n}$ and that is reflected into the stretched recovery of the longitudinal magnetization in the T_{1n} sequences. So Eq. 3.78 is replaced by [228–230]:

$$\left\langle \frac{1}{T_{1n}} \right\rangle = \int P\left(E_A\right) \frac{1}{T_{1n}\left(E_A\right)} d\left(E_A\right). \tag{3.81}$$

A reasonable assumption is to take a rectangular distribution of activation energy barriers, with mean value E_A and half width Δ, so that Eq. 3.81 becomes [230]:

$$\frac{1}{T_{1n}} = \frac{\gamma_n^2 \left\langle \Delta h_\perp^2 \right\rangle}{2\omega_I \Delta} \left[\arctan\left[\omega_I \tau_1 \exp\left(\frac{E_A + \Delta}{T}\right)\right] - \arctan\left[\omega_I \tau_1 \exp\left(\frac{E_A - \Delta}{T}\right)\right]\right]. \tag{3.82}$$

Furthermore, in case of molecular dynamics, defining $\tau_R = \tau_1 \exp E_A/T$, the time evolution of the NMR signal is given by [6]:

$$G\left(t\right) = G\left(0\right) \cdot \exp -\omega_I^2 \tau_R^2 \left[\exp -\frac{t}{\tau_R} - 1 + \frac{t}{\tau_R}\right]. \tag{3.83}$$

By taking the Fourier transform of this curve, one can derive the NMR spectrum and evaluate the theoretical prediction of the NMR linewidth in the presence of molecular motion, to be compared with the experimental one as well as with the characteristic correlation time derived from Eq. 3.82.

3.2 DNP in βCyclodextrins

3.2.1 βCyclodextrins Properties and Preparation

Cyclodextrins are naturally occurring ring-shaped oligosaccharides formed by different number of α-[1-4]-linked α-d-glucopyranose units[125, 127]. The most common CDs have 6, 7 and 8 glucose units (α, β and γCD, respectively, see Fig. 3.16) but CDs with higher number (up to thirteen) of units have been reported [125], while steric factors prevents formation of CDs with less than 6 units.

They are produced through the intramolecular transglycosylation reaction during degradation of starch and they are also named cycloamyloses, cyclomaltoses or Schardinger dextrins [126]. They have cone-shaped or toroidal structure, where the narrower edge is called primary face and the wider edge is called secondary face and both edges are covered by several hydroxyl groups which give rise to an outer hydrophilic surface. The inner cavity is hydrophobic instead due to the presence of apolar molecular groups and it is lipophilic. For these reasons CDs are able to form inclusion complexes with a wide range of liquid, solid and gaseous appropriate size molecules (called guests), giving rise to a dynamic binding strongly depending on how well host and guest fit together and on the interaction between surface atoms [126, 129, 131, 231]. While the main force driving the complex formation is the thermodynamic balance which favors the inclusion due to an energy gain, the binding can take place both in solid and liquid phase, through methods like co-precipitation, slurry complexation and dry and liquid mixing. They act as a supramolecular cage able to modify the physicochemical properties of the guest they bind with. Furthermore, they are mainly non-toxic, when administered orally or parentally, and slowly biodegradable and have a relatively good solubility in water. CDs are known to crystallize forming either channel structures and cage structures. CDs are widely used in the pharmaceutical and health care for the delivery of active principles [130, 131], since they are able to increase drug's aqueous solubility, dissolution rate, stability against effects of light (visible or UV) and oxidation and heat, controlled released (which can be immediate, prolonged or delayed) and, more in general, to modify the guest chemical reactivity and stability in all phases [126, 127, 130, 232]. Their hydrophilic surface prevents them from crossing biological membranes and this is vital for enhancing drug bioavailability in the place of interest. Furthermore many drugs imply a combination of solvents and extreme pH conditions, which often cause irritation or other adverse reactions, while CDs are known not to irritate tissues. Volatile drugs can be handled thanks to the inclusion complex with CDs, which can also reduces the effect of drugs bad smelling or tasting. Examples of applications in this sectors are oligonucleotide agents [233], peptides [234] or heparin delivery [235]. They also find application in food science, cosmetics, environment protection, bioconversion, packing and textile industry, agricultural chemical industry [126]. The presence of several hydroxyl groups with different

reactivity allows to functionalize the CD cone, by esterification or etherification, in a selective way and to modify the physico-chemical properties of the final derivative for applications [125]. Considering also the possibility, due to covalent or noncovalent links to other CDs, to build up complex supramolecular architectures like catenanes, rotaxanes, polyrotaxanes and tubes [236–241], CDs applications nowadays range from the design of molecular machines, to the development of nanovectors for the cancer treatment and the gene delivery [132, 232, 236–239, 242, 243]. With specific reference to the medical diagnostics, CDs are, for the same reasons, also promising candidates for the synthesis of advanced contrast agents for MRI by specific binding with Manganese-based molecules [244], Gadolinium [133, 135, 245] and mono or polynitroxides [134], with proton relaxivities close to the traditional and currently used Gd-based contrast agents [135, 244, 246].

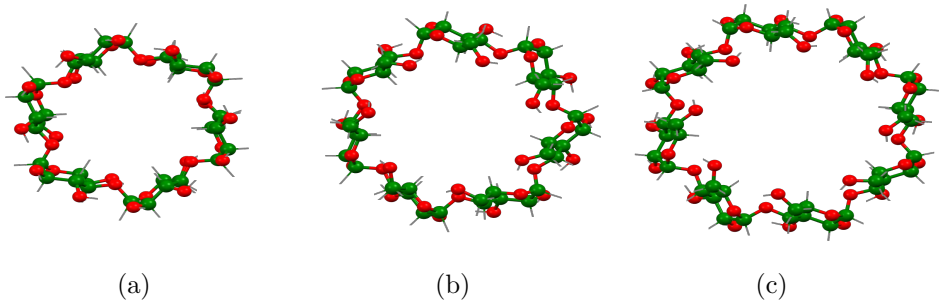

(a) (b) (c)

Figure 3.16: Molecular structures of: a) αCD, b) βCD, c) γCD. Red balls, green balls and gray sticks are oxygen, carbon and hydrogen atoms, respectively.

Successful hyperpolarization of βCD's may be exploited to follow their evolution in several medical applications through molecular imaging experiments. For example, βCD's complexes are used to remove lipofuscin from the retinal pigment epithelium [247], to efficiently deliver dosages of insulin in type 2 diabetes patients [248], to treat autosomal recessive neurologic diseases caused by defective intracellular cholesterol and lipid trafficking [249] and to attack multidrug resistant bacteria [250].

In this thesis, attention has been focused on βCD, since they are most accessible, lowest priced and the most studied for human health [126]. βCD-TEMPO has been synthesized following a known procedure [134], leading to amorphous samples. Samples with different concentration of free radicals were prepared by dissolving weighted amounts of βCD and βCD-TEMPO in 2 mL of (DMSO) at room temperature (Fig. 3.17).

Name	Rad(%)	$^{13}CH_3$	$^{13}CD_3$	Batch
CD025	0.25	0	0	1^{st}
CD050	0.50	0	0	1^{st}
CD100	1.00	0	0	1^{st}
CD200	2.00	0	0	1^{st}
CD400	4.00	0	0	1^{st}
CD600	6.00	0	0	1^{st}
CD9	0	9	0	2^{nd}
CD21	0	21	0	2^{nd}
CD9R	1.00	9	0	2^{nd}
CD21R	1.00	21	0	2^{nd}
CD21d	0	0	21	3^{rd}
CD21Rd	1.00	0	21	3^{rd}

Table 3.2: Table summarizing DNP samples. The second, third, fourth and columns refers to the free radical concentration, to the number of methyl groups and of deuterated methyl groups per molecule, respectively.

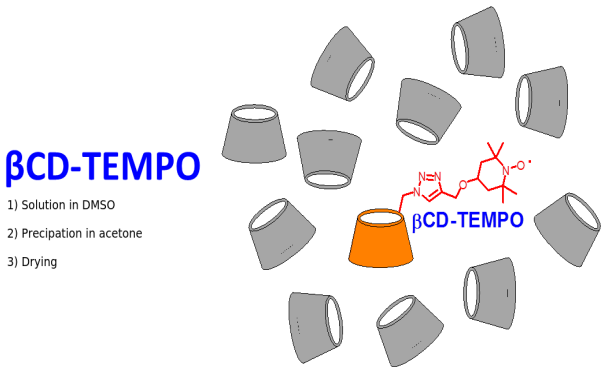

Figure 3.17: Preparation procedure for the βCD/βCD-TEMPO solid sample.

The w/w percentage of TEMPO radical (with respect to the total mass) is:

$$\%\text{TEMPO} = 100 \times \frac{\left(\frac{m_{\beta\text{CD}-\text{TEMPO}}}{1370.50} \times 156.25\right)}{m_{\beta\text{CD}} + m_{\beta\text{CD}-\text{TEMPO}}}, \tag{3.84}$$

where 1370.5 is the βCD-TEMPO molar mass while 156.25 is the molar mass of TEMPO radical. The solution has been poured in acetone, stirred and the solid was recovered by filtration and the washing procedure has been repeated five times [251]. Finally, the solid has been dried in air and under vacuum. The recovery of the solid material has been quantitative for all samples. It is important to remark that the alternative use of TEMPO non-covalently tethered to the βCD macrocycle has the disadvantage that the radical is practically irrecoverable at the end of the procedure due to its high solubility in acetone.

^{13}C-enriched βCD's have been doped with TEMPO free radical covalently tethered to a permethylated βCD (Me-CD-TEMPO, see Fig. 3.18). βCD has been purchased from Alfa Aesar while Iodomethane-^{13}C has purchased from

Sigma-Aldrich, and both have been dried before use. Methylation of the βCD (CD9 and CD21, i.e. Me-CD) have been obtained by solving weighted amounts of pure βCD and Iodomethane-^{13}C in DMF solutions, while doped samples (CD9R and CD21R) have been synthetized by mixing weighted amounts of Me-CD-TEMPO and Me-CD in DMF solution, according to the literature [134, 240, 252]. All the solution have been followed by recovery of the solid [252].

This list summarizes all the samples studied:

- First Batch. βCD's samples doped with the following amounts of TEMPO free radical, 0.10, 0.13, 0.25, 0.50, 1.00, 2.00, 4.00, 6.00, % (TEMPO weight over total weight) are named CD010, CD013, CD025, CD050, CD100, CD200, CD400, CD600, respectively. CD100 liquid solutions (25, 50, 75 and 100 mM) in d-DMSO were obtained by dissolving weighted amounts of CD100 in 0.5 mL of d-DMSO (see also Fig. 3.17). The aim of the first batch is to find the optimal TEMPO concentration yielding the highest ^{1}H DNP enhancement and to study the dependence of nuclear relaxation and polarization rates over the TEMPO concentration in order to check the role of the free electrons.

- Second Batch. ^{13}C-enriched samples CD9 (partially methylated with an average of 9.5 methyl groups per molecule) and CD21 (totally methylated with 21 methyl groups per molecule) and the corresponding TEMPO-doped (with 1 % w/w) samples (CD9R and CD21R respectively) (see also Fig. 3.19). The aim of the second batch is to explore ^{13}C DNP performances and high-temperature spin relaxation and to compare them to ^{1}H ones.

- Third Batch. The third batch contains a βCD's sample doped with 1 % TEMPO and totally methylated (21 methyl groups per molecules) with $^{13}CD_3$, called CD21Rd. The corresponding methylated and deuterated, but undoped sample is CD21d. The aim of the third batch is to improve ^{13}C DNP performances and to increase the ^{13}C room temperature relaxation rate.

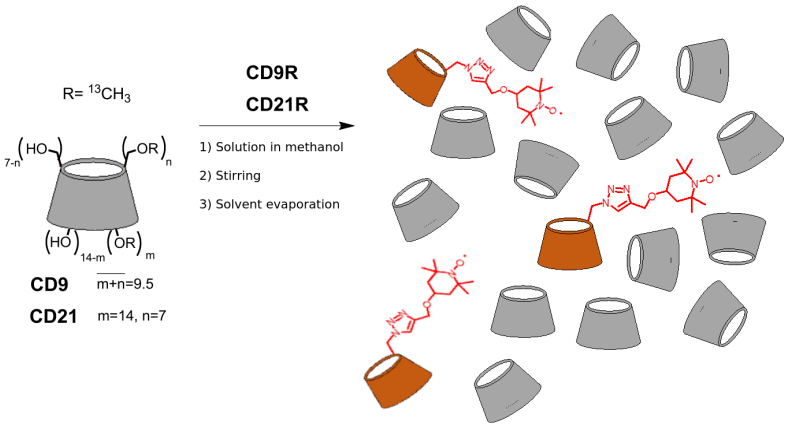

Figure 3.18: Preparation of CD9R and CD21R.

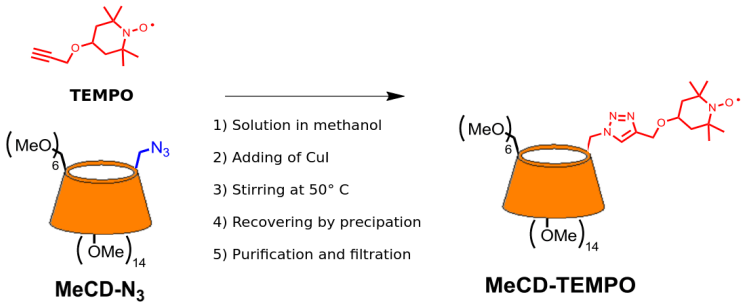

Figure 3.19: Synthesis of MeCD-(2,2,6,6-tetramethylpiperidin-1-yl)oxyl (TEMPO).

3.2.2 Results and Discussion

All the DNP experiments in the low-temperature range (T < 4.20 K) have been performed at 3.45 T where ^{1}H and ^{13}C Larmor frequencies are 147 MHz and 37 MHz, respectively. The EPR experiments have been carried out in the X-band, with electron Larmor frequency equal to 9.6 GHz.

First Evidences for a Thermal Mixing

The theory describing the fast thermal mixing regime predicts a linear relationship between ^{1}H $1/T_{1n}$ and ^{1}H $1/T_{POL}\,(1-P_S^2)$ by combining Eq. 3.35 and 3.45. The TEMPO free radical belongs to the nitroxides family, which is characterized by broad EPR spectrum, with $\Delta\omega_S$ often larger than ω_I; thus it is reasonable to guess that the TM regime is the relevant one.

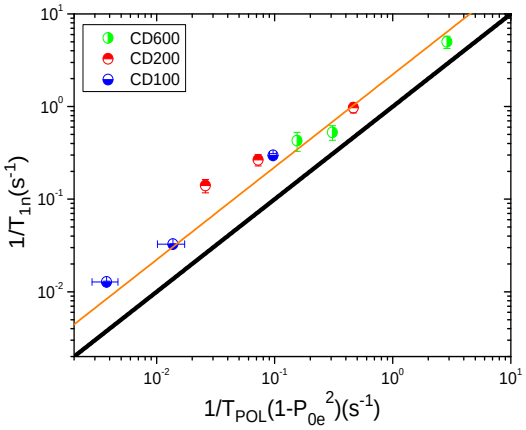

Figure 3.20: Plot of ^{1}H $1/T_{1n}$ over ^{1}H $1/T_{POL}\left(1-P_S^2\right)$ for CD600 (green half right circles), CD200 (blue half down circles) and CD100(red half up circles) at 3.45 T, with temperature as implicit parameter. The thick black line is the theoretical relation predicted by Eq. 3.35 in the case of the fast thermal mixing regime. The orange thin line is the linear fit ($y = A \cdot x$).

In Fig 3.20 a linear relationship between the nuclear spin-lattice relaxation rate and the nuclear polarization rate, weighted by a factor containing the thermal electron polarization, is reported for different samples from the first batch, which are doped with variable amounts of TEMPO free radical. **This is a first clue suggesting that in βCD's doped TEMPO the DNP process takes place through the TM regime.**

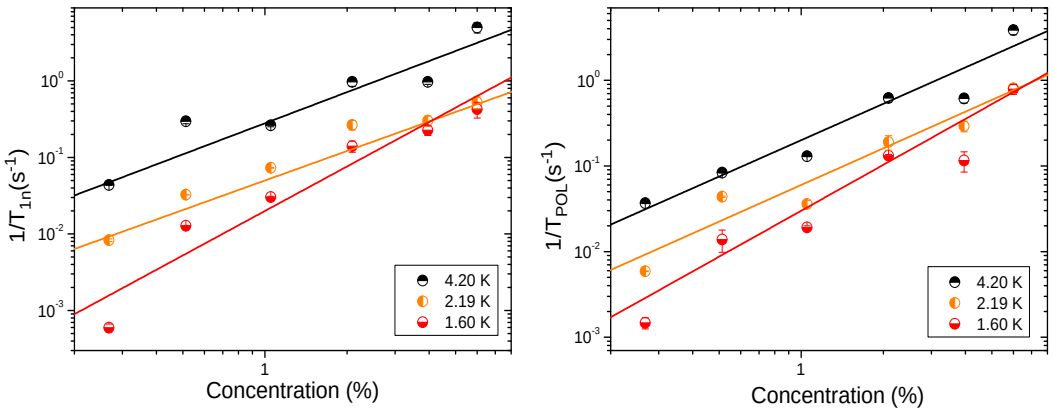

(a) (b)

Figure 3.21: a) ^{1}H $1/T_{1n}$ radical concentration dependence at 4.20 (black half up circles), 2.19 (orange half left circles) and 1.60 K (red half down circles) at 3.45 T. Fit according to $y\left(C\right) = a \cdot C^f$. b) ^{1}H $1/T_{POL}$ radical concentration dependence at 4.20 (black half up circles), 2.19 (orange half left circles) and 1.60 K (red half down circles) at 3.45 T. Fit according to $y\left(C\right) = a \cdot C^f$.

Remarkably, all the experimental points in Fig. 3.20 lie above the theo-

	Spin	T (K)	a (s^{-1})	f
$1/T_{1n}$	^1H	4.20	0.28 ± 0.06	1.35 ± 0.15
$1/T_{1n}$	^1H	2.19	0.05 ± 0.01	1.28 ± 0.06
$1/T_{1n}$	^1H	1.60	0.02 ± 0.01	1.93 ± 0.05
$1/T_{POL}$	^1H	4.20	0.26 ± 0.04	1.41 ± 0.09
$1/T_{POL}$	^1H	2.19	0.06 ± 0.01	1.42 ± 0.04
$1/T_{POL}$	^1H	1.60	0.03 ± 0.01	1.78± 0.08
$1/T_{1e}$ F	e^-	5.00	$(2.9 \pm 0.2)\times 10^{-5}$	0.72 ± 0.07
$1/T_{1e}$ S	e^-	5.00	$(2.9 \pm 0.1)\times 10^{-6}$	0.46 ± 0.02
$1/T_{2e}$	e^-	5.00	$(6.0 \pm 0.5)\times 10^{-3}$	0.74 ± 0.02

Table 3.3: Parameters for $y\,(C) = a \cdot C^f$ of different quantities.

retical prediction, underlining that either the nuclear relaxation is faster from that predicted by TM theory or the nuclear polarization rate is slower: this discrepancy might be due to a reduced efficiency of the nuclear diffusion process or to the MW power, which might not be high enough to strongly saturate the EPR spectrum.

The role of the free electrons

The first set of DNP experiments has been carried out to clarify the role of the free electrons and of their concentration in the proton relaxation and polarization processes. Fig. 3.21 shows how ^{1}H $1/T_{1n}$ and $1/T_{POL}$ change upon increasing the radical concentration C in the βCD's (technical details are given in Sec. A.1.2 and A.1.2). $1/T_{1e}$ and $1/T_{2e}$ radical concentration dependence is reported in Fig. 3.22 (technical details are given in Sec. A.3.2 and A.3.2).

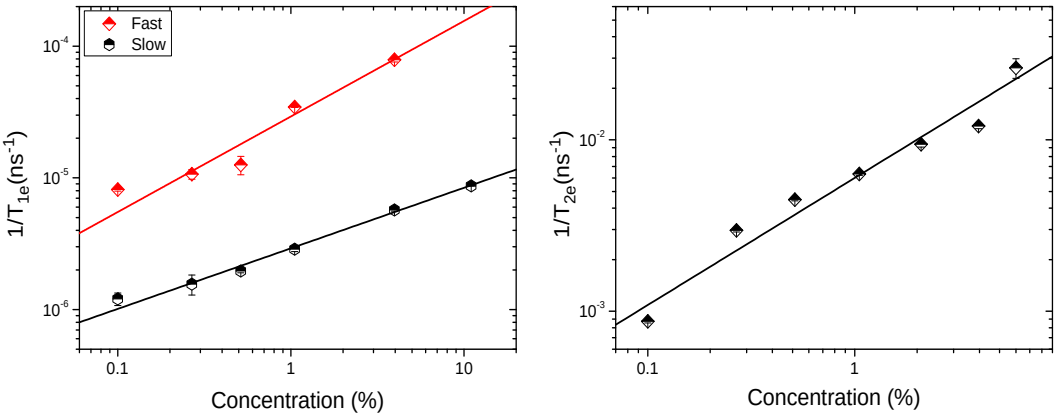

(a) (b)

Figure 3.22: a) Electron spin-lattice relaxation rate components as function of radical concentration at 5 K. Fit according to $y\,(C) = a \cdot C^f$. b) Electron spin-spin relaxation rate as function of radical concentration at 5 K. Fit according to $y\,(C) = a \cdot C^f$.

From Fig. 3.21a it is clear that if C increases by one order of magnitude

then ^{1}H T_{1n} decreases by one order of magnitude, underlining **the relevance of the hyperfine interaction as the main channel for the nuclear spin-lattice relaxation**. Since the data in Fig. 3.21a have been fit using a simple power-law, without addition of a constant term, the nuclear spin-spin interaction plays an almost negligible role in the nuclear relaxation (and magnetic interaction with other nuclear species can be neglected since ^{13}C and ^{17}O have very low abundance). The fit yields an exponent f $\simeq$ 1.3 at 4.20 and 2.19 K, while providing a larger value ($\simeq$ 1.9) at 1.60 K. This feature is in common with $1/T_{POL}$, which displays a strong radical concentration dependence (as expected) following similar power-law functions (3.21b), with fit yielding exponents $\simeq$ 1.4 at 4.20 and 2.19 K and $\simeq$ 1.8 at 1.60 K, far from values found in previous DNP studies on different compounds [122]. From the fast thermal mixing regime theory, Eq. 3.35 and 3.45 are known to depend on $1/T_{1e}$ ($\sim$ C^{x}) and N_S/N_I(= C), so that the product scales as C^{x+1}. Thus, NMR data predict x $\simeq$ 0.3 - 0.4 at 4.20 and 2.19 K and x $\simeq$ 0.8 - 0.9 at 1.60 K. EPR data (Fig. 3.22a) show that a fast component in the electron spin-lattice relaxation, whose power-law dependence is similar to that of $1/T_{2e}$ (Fig. 3.22b) and that can thus be ascribed to the electron spectral diffusion, and a slow one, which is the classical phonon-driven spin-lattice relaxation. Since the former scales as $\sim$ C$^{0.4}$ and the latter as $\sim$ C$^{0.7}$, it is reasonable to suggest that only for T approaching 4.20 K the electron spin-lattice contribution becomes relevant for the nuclear relaxation.

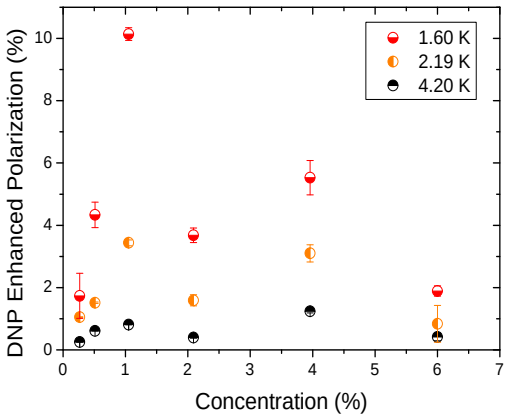

Figure 3.23: DNP enhanced polarization radical concentration dependence at 4.20 (black half up circles), 2.19 (orange half left circles) and 1.60 K (red half down circles) at 3.45 T.

Interestingly, the power-law exponents shown in Table 3.3 for ^{1}H are much different from the values obtained in other molecules characterized by good DNP through TM regime, which were around 3 in Ref. [122] and around 1 in Ref. [111, 114]. It is possible that the huge different size between the molecules studied here and those analyzed in other works could influence this behavior.

Finally, the ^{1}H DNP enhanced polarization (shown as function of the free radical concentration in Fig. 3.23) **has its maximum value for the**

CD100 sample at 1.60 K, where proton polarization is around 10 %, a value of the same order of magnitude, even if lower in some cases, to other found elsewhere [27, 110, 117, 118], where P could reach even 97 %.

The corresponding signal enhancement is 47. The optimal free radical weight (1 % over total weight) is then used in the second and third batches samples, which are labelled with ^{13}C. An interesting feature of Fig. 3.23 is that for too low or too high radical concentrations the DNP process efficiency strongly diminishes [34, 39, 96, 110, 114, 121, 122, 174, 187, 253]. For low concentrations the number of free electrons available for the DNP is reduced, thus slowing the polarization transfer process and affecting the final performance. For high concentrations the hyperfine interaction strongly enhances the nuclear spin-lattice relaxation (see Fig. 3.21) and the hyperpolarized state is rapidly destroyed [215, 254].

^{1}H and ^{13}C Thermal Mixing

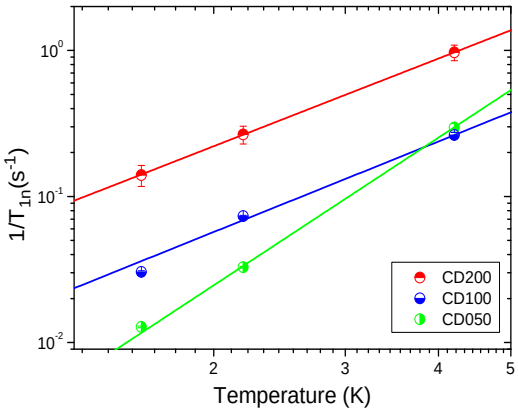

Figure 3.24: ^{1}H nuclear spin-lattice relaxation rate temperature dependence in CD200 (red half up circles), CD100 (blue half down circles), CD050 (green half right circles) at 3.45 T. Fit according to $y(T) = a \cdot T^b$.

To get a deeper look at the DNP process it is fundamental to study the temperature dependence of the ^{1}H relaxation and polarization rates in the samples belonging to the first batch (technical details are given in Sec. A.1.2 and A.1.2). First of all, to understand which dynamics is modulating the hyperfine interaction, that is driving nuclear relaxation, one has to refer to Fig. 3.24, where ^{1}H $1/T_{1n}$ displays a power-law dependence over the temperature, that is nearly quadratic for CD100, CD200 and CD400, while it is cubic for lower (CD025, CD050) and higher (CD600) radical concentrations. At these low temperatures the molecular dynamics is frozen and it is not involved, but, as explained in Section 3.2.1, **the sample is in an amorphous phase, where low-frequency glassy modes can induce fluctuations in the spatial arrangement of the local structure, thus modulating the hyperfine**

field probed by nuclei. By taking Eq. 3.80, with a distribution $p(E_G) \propto E_G$, one obtains $1/T_{1n} \propto T^2$, that is a quadratic trend which nicely explains the behavior of CD100, CD200, CD400 and which is common to other amorphous compounds [120, 122]. The departure of b from 2 at low radical concentrations might be explained by considering that in this limit the nuclear dipolar interaction may interfere. On the other hand, for higher free radical concentration, the strong electron coupling causes $1/T_{1e}$ to change its temperature dependence and, through Eq. 3.35, also $1/T_{1n}$ temperature dependence: this is a sign of a good thermal contact [122].

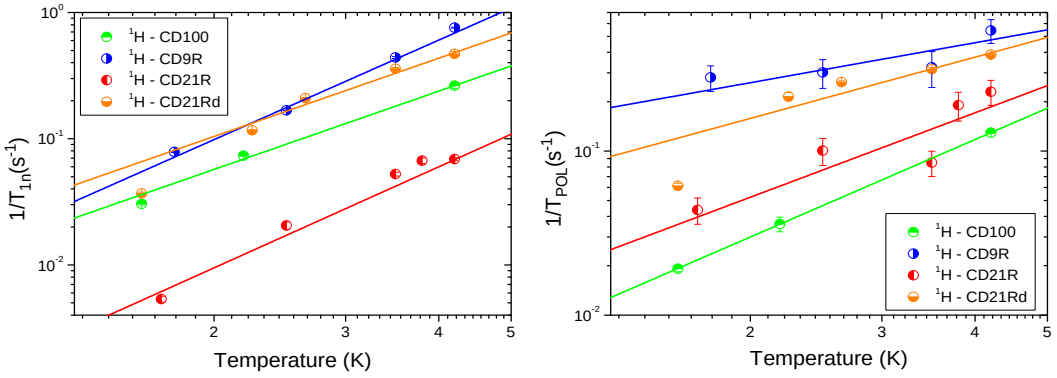

(a) (b)

Figure 3.25: a) ^{1}H $1/T_{1n}$ temperature dependence for CD100 (green half up circles), CD9R (blue half right circles), CD21R (red half left circles) and CD21Rd (orange half down circles) at 3.45 T. Fit according to $y(T) = a \cdot T^b$. b) ^{1}H $1/T_{POL}$ temperature dependence for CD100 (green half up circles), CD9R (blue half right circles), CD21R (red half left circles) and CD21Rd (orange half down circles) at 3.45 T. Fit according to $y(T) = a \cdot T^b$.

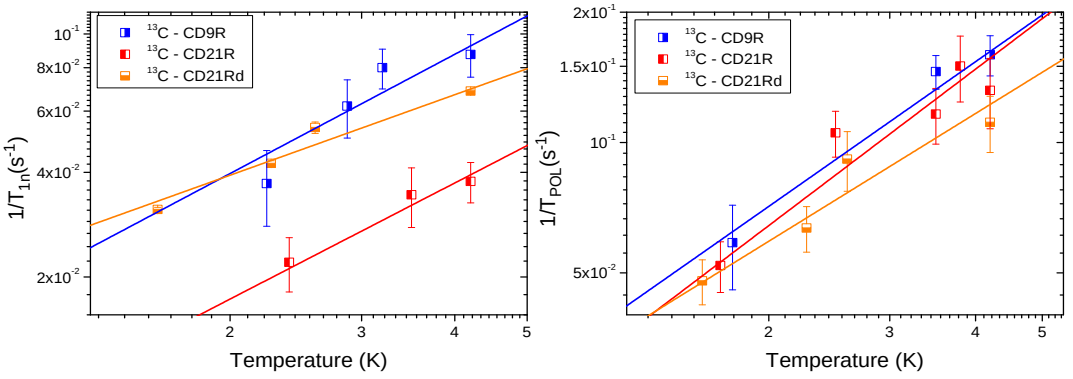

(a) (b)

Figure 3.26: a) ^{13}C $1/T_{1n}$ temperature dependence for CD9R (blue half right squares), CD21R (red half left squares) and CD21Rd (orange half down squares) at 3.45 T. Fit according to $y(T) = a \cdot T^b$. b) ^{13}C $1/T_{POL}$ temperature dependence for CD9R (blue half right squares), CD21R (red half left squares) and CD21Rd (orange half down squares) at 3.45 T. Fit according to $y(T) = a \cdot T^b$.

Sample	Nucleus	a ($s^{-1}K^{-b}$)	b
CD100	^{1}H	$(7.6 \pm 0.5) \times 10^{-3}$	1.97±0.05
CD9R	^{1}H	$(1.5 \pm 0.8) \times 10^{-1}$	0.81±0.04
CD21R	^{1}H	$(1.6 \pm 0.1) \times 10^{-1}$	1.71±0.37
CD21Rd	^{1}H	$(6.7 \pm 2.4) \times 10^{-2}$	1.24±0.28
CD9R	^{13}C	$(3.3 \pm 0.1) \times 10^{-2}$	1.11 ±0.20
CD21R	^{13}C	$(2.8 \pm 0.1) \times 10^{-2}$	1.20±0.14
CD21Rd	^{13}C	$(2.6 \pm 0.4) \times 10^{-2}$	0.98± 0.15

Table 3.5: Parameters for $y(T) = a \cdot T^b$ of $1/T_{POL}$ temperature dependence.

Then, once the optimal concentration is fixed, the temperature dependence of ^{1}H and ^{13}C relaxation and polarization rates may be studied to investigate the chemical changes in samples from the second and third batches.

Fig. 3.25 shows the ^{1}H $1/T_{1n}$ and ^{1}H $1/T_{POL}$ temperature dependence, in samples CD100, CD9R, CD21R and CD21Rd, namely with 0, 9, 21 and 21-deuterated methyl groups per molecule, while Fig. 3.26 shows the ^{13}C $1/T_{1n}$ and ^{13}C $1/T_{POL}$ temperature dependence, in samples CD9R, CD21R and CD21Rd.

Sample	Nucleus	a ($s^{-1}K^{-b}$)	b
CD025	^{1}H	$(7.5 \pm 5.4) \times 10^{-4}$	2.83 ± 0.51
CD050	^{1}H	$(2.4 \pm 0.2) \times 10^{-3}$	3.36±0.06
CD100	^{1}H	$(1.4 \pm 0.3) \times 10^{-2}$	2.06±0.13
CD200	^{1}H	$(5.5 \pm 0.1) \times 10^{-2}$	1.99±0.01
CD400	^{1}H	0.10 ± 0.02	1.56±0.13
CD600	^{1}H	0.05 ± 0.01	3.32±0.01
CD9R	^{1}H	$(1.6 \pm 0.3) \times 10^{-2}$	2.62±0.19
CD21R	^{1}H	$(0.2 \pm 0.1) \times 10^{-2}$	2.66±0.31
CD21Rd	^{1}H	$(2.5 \pm 0.8) \times 10^{-2}$	2.06±0.23
CD9R	^{13}C	$(1.8 \pm 0.8) \times 10^{-2}$	1.14±0.22
CD21R	^{13}C	$(0.7 \pm 0.3) \times 10^{-2}$	0.77±0.15
CD21Rd	^{13}C	$(2.3 \pm 0.3) \times 10^{-2}$	1.11±0.37

Table 3.4: Parameters for $y(T) = a \cdot T^b$ of $1/T_{1n}$ temperature dependence.

As it can be observed by Fig. 3.25a and 3.26a $1/T_{1n}$ is found to critically depend on N_S/N_I, as suggested by Eq. 3.35. When one increases the methylation degree of the molecules, N_I increases, while N_S stays constant, leading to a overall decrease of their ratio and to **a drop in the nuclear spin-lattice relaxation rate: this effect is known as the bottleneck effect**. In this case the nuclear relaxation is mainly due to the indirect relaxation described in Section 3.1.2. This means that energy flows first from nuclei to electrons and then from electrons to the lattice. If the number of nuclei increases while the number of electrons is kept constant, then each electron is forced to relax a more nuclear spins thus generating a bottleneck for energy flow. Furthermore, the large increase in N_I may also have a influence on the $1/T_{POL}$: when the nuclear concentration increases, distances between nuclei gets shorter and

nuclear dipolar magnetic interaction is faster, since it depends on the inverse cubic root of the distance between the interacting spins.

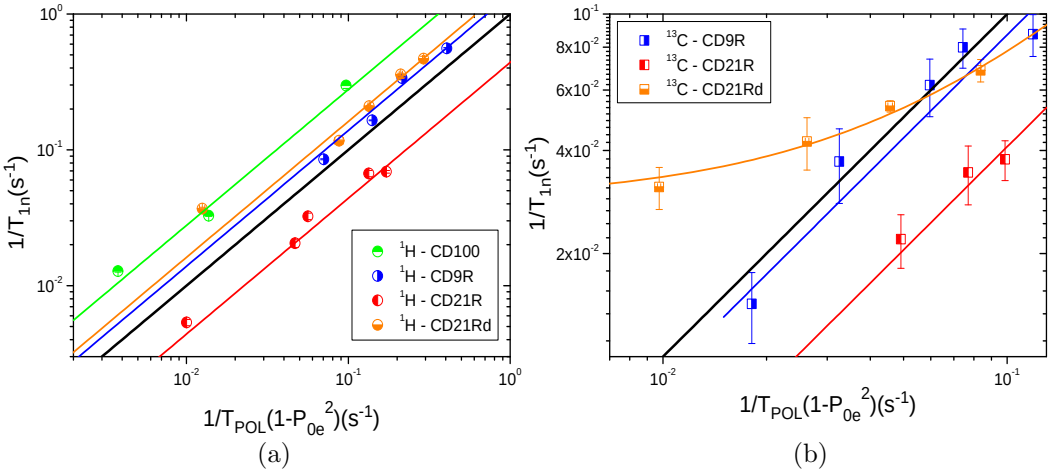

Figure 3.27: a) Plot of ^{1}H $1/T_{1n}$ over ^{1}H $1/T_{POL}\left(1-P_S^2\right)$ for CD100 (green half up circles), CD9R (blue half right circles), CD21R (red half left circles) and CD21Rd (orange half down circles) at 3.45 T, with temperature as implicit parameter. The thick black line is the theoretical relation predicted by Eq. 3.35 in the case of the fast thermal mixing regime. Fit according to $y = A \cdot x$. b) Plot of ^{13}C $1/T_{1n}$ over ^{13}C $1/T_{POL}\left(1-P_S^2\right)$ for CD9R (blue half right squares), CD21R (red half left squares) and CD21Rd (orange half down squares) at 3.45 T, with temperature as implicit parameter. The thick black line is the theoretical relation predicted by Eq. 3.35 in the case of the fast thermal mixing regime. Fit according to $y = A \cdot x$.

However, the overall macroscopic process that spreads polarization in the sample becomes slower and this compensate the speeding up of the microscopic spin diffusion: in Fig. 3.25b and 3.26b great and slight polarization rates reductions are found when going from CD9R to CD21R for ^{1}H and ^{13}C, respectively. Interestingly, sample CD21Rd, seems not to suffer the bottleneck effect and its experimental points lie close to the theoretical line both for ^{1}H and ^{13}C, as shown in Fig. 3.27a and 3.27b. In case of the former, the protons hyperpolarized belong to the OH- groups, similarly to the hyperpolarized protons in CD100. Regarding ^{13}C, the nuclei still sit in the methyl groups, but they are now surrounded by deuterium instead of protons. Since the N_S/N_I for carbon atoms does not change upon deuteration (i.e. from CD21R to CD21Rd), it looks like another channel of relaxation allows nuclei to overcome the bottleneck due to the electron spins. The power-law exponents for the fit in Fig. 3.25b for ^{1}H are slightly lower than those found in Ref. [122].

Finally, to check the validity of the fast thermal mixing regime, Fig. 3.27 summarizes the relation between $1/T_{1n}$ and $1/T_{POL}\left(1-P_S^2\right)$ for ^{1}H and ^{13}C, respectively, in samples CD100 (only ^{1}H), CD9R, CD21R and CD21Rd.

As it can be noticed, in CD9R, for both nuclear species the points lie very close to the theoretical prediction, **suggesting that a TM regime is**

Sample	Nucleus	A
Batch 1	^{1}H	2.97 ± 0.30
CD100	^{1}H	2.97 ± 0.30
CD9R	^{1}H	1.39 ± 0.06
CD21R	^{1}H	0.44 ± 0.03
CD21Rd	^{1}H	1.62 ± 0.04
CD9R	^{13}C	0.87 ± 0.08
CD21R	^{13}C	0.41 ± 0.02
CD21Rd	^{13}C	0.49± 0.05

Table 3.6: Parameters for $y = A \cdot x$ fit of $1/T_{1n}$ over ^{1}H $1/T_{POL}\left(1 - P_S^2\right)$.

attained for both ^{1}H and ^{13}C. It must be pointed out that in CD100 the protons hyperpolarized belong to the several OH- groups, while in CD9R they almost all belong to the methyl groups. This shows that a different spatial arrangement, in this case somewhat less homogeneous, does not change the DNP regime and does not prevent nuclear hyperpolarization. On the other hand, in CD21R, a linear relationship is found, though the experimental points lie well below the theoretical prediction for both ^{1}H and ^{13}C, underlining a deviation from the model. This drop is due to the reduction of $1/T_{1n}$ in CD21R with respect to CD9R.

Polarization Results

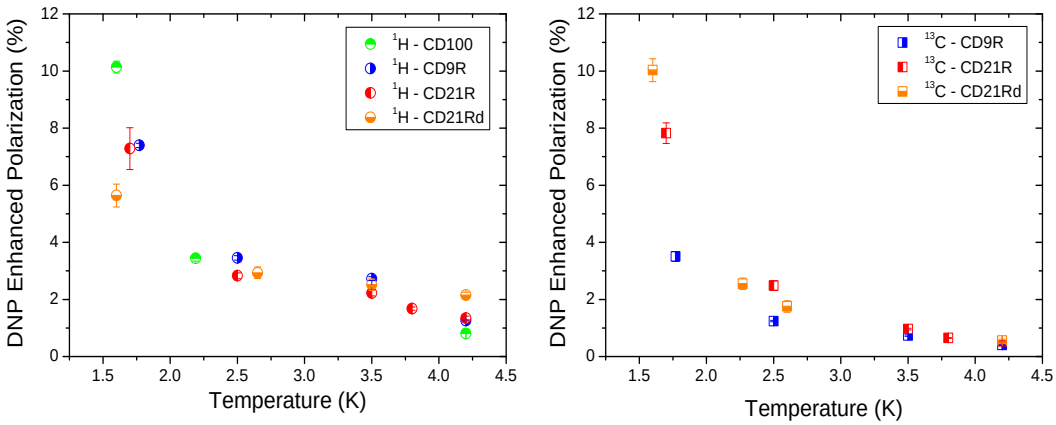

(a) (b)

Figure 3.28: a) ^{1}H DNP enhanced polarization temperature dependence for CD100 (green half up circles), CD9R (blue half right circles), CD21R (red half left circles) and CD21Rd (orange half down circles) at 3.45 T. b) ^{13}C DNP enhanced polarization temperature dependence for CD9R (blue half right squares), CD21R (red half left squares) and CD21Rd (orange half down squares) at 3.45 T.

The ^{1}H and ^{13}C DNP enhanced polarization are shown in Fig. 3.28 as a function of temperature.

Regarding ^{1}H the best results have been achieved in CD100, with a polarization equal to 10 % at 1.60 K, that is a pretty satisfactory achievement, if compared to other DNP works [27, 110, 112, 115], considering also the novelty of this work. It is also noticed that the MW power, which is fixed to 15 mW in our MW source, can affect the DNP performances: it has been found that if one reduces the MW power below 100 mW then the DNP signal enhancement decreases [110], due to incomplete saturation. In methylated samples, with an equal free radical concentration, the proton polarization is slightly lower, around 6 to 7.5 %, probably due to the different arrangement and concentration of nuclear spins that probably affect the nuclear spin diffusion and the overall DNP performances [110]. **Concerning ^{13}C**, one observes striking differences between CD9R and CD21R, where **maximum polarizations achieved at 1.60 K are 3.5 and 7.8 %**, respectively. In sample CD9R, **^{1}H and ^{13}C corresponds to almost equal spin temperatures**, confirming the hypothesis that in this sample the TM regime is attained for both species. On the other side, in sample CD21R the ^{13}C is markedly lower, with better DNP performances. As stated in the previous paragraph, in this sample ^{13}C nuclear spins exit the fast TM regime, yielding a different behavior with respect to the one expected.

Deuteration of the methyl groups has the clear effect of enhancing DNP performances on ^{13}C by increasing the maximum DNP polarization around 10 %. This latter effect has been also observed elsewhere [89, 110, 192, 255] for TEMPO-doped deuterated substrates and it has been ascribed to the reduced heat capacity for the nuclear Zeeman reservoir caused by deuteration, which leads to a more efficient thermal contact with the electron dipolar one. It must be remarked that in a TM framework that different nuclear spin reservoirs reach the same spin temperatures and there may an exchange of energy between them. The result obtained here is a good starting point [75], even if better DNP performances have been achieved in ^{13}C hyperpolarization [27, 29, 110, 111, 113–115, 182, 255], with P ranging from 14 to 46 %. There might be two reasons: the large size of βCD, which could badly affect the hyperpolarization by making nuclear spin diffusion slower with respect to small size molecules, or the use of this specific free radical, the TEMPO nitroxide, whereas other radicals could transfer polarization more efficiently.

Another striking feature about the results presented here is that the nuclear hyperpolarization is achieved rather quickly, with $\mathbf{T}_{POL}$ around tens of seconds (see Fig. 3.29), as opposed to previous DNP works where the process took from several minutes to even hours [27, 29, 42, 109–111, 113–115, 174, 182, 192]. This feature has been observed also in other macromolecules, like proteins [118], biological macromolecules [88] and polymers [98], with comparable DNP performances. This feature represents an advantage since it allows fast repetition of DNP experiments, in particular in the case of high resolution NMR experiments.

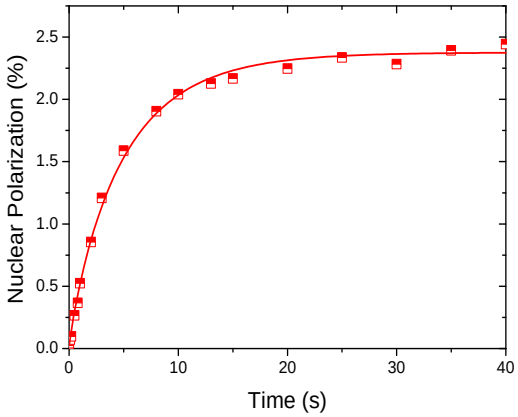

Figure 3.29: ^{13}C nuclear hyperpolarization build-up in the presence of the MW irradiation in CD21R at 2.5 K at 3.45 T.

^{1}H High Temperature Relaxation

The ^{1}H $1/T_{1n}$ and nuclear linewidth for CD100 are reported in Fig. 3.30, in the high temperature range (technical details are given in Sec. A.1.2 and A.1.2).

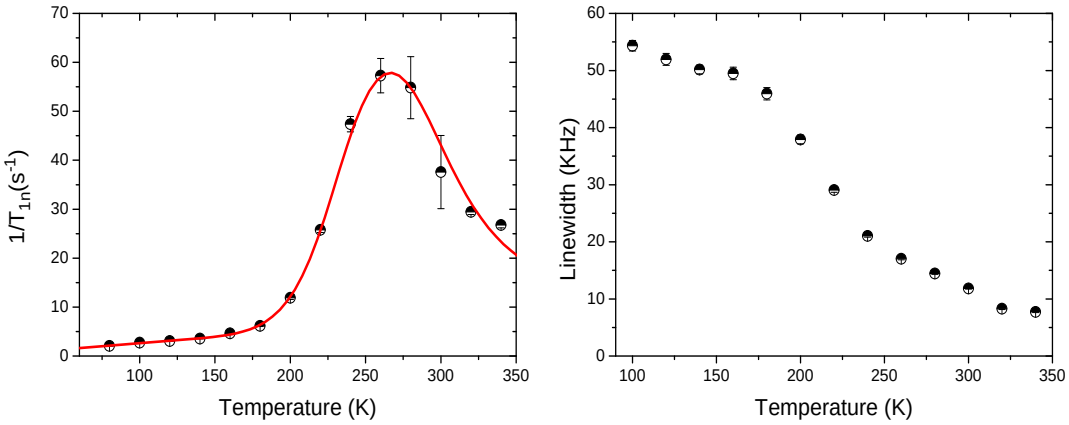

(a) (b)

Figure 3.30: a) ^{1}H $1/T_{1n}$ temperature dependence for CD100 at 1.50 T. Fit according to Eq. 3.82 plus a power-law term $y(T) = a \cdot T^b$.

From Fig. 3.30a, **the ^{1}H $1/T_{1n}$ follows a power-law trend up to 170 K and it is then characterized by broad peak for higher temperatures, that is related to the intramolecular motion of CH, OH (largely abundant in βCD's) and CH_2 (one for each of the seven units of glucopyranose)**: using Eq. 3.82 to fit the peak, one obtains an average energy barrier E_A to molecular rotation around 2570 K. Fig. 3.30b confirms the hypothesis of molecular dynamics, showing how nuclear linewidth is reduced since the NMR spectrum is affected by motional narrowing. However, the narrowing

is not as sharp as predicted by theory [6], since the free radicals generate an additional local field which causes a broadening in the NMR spectrum.

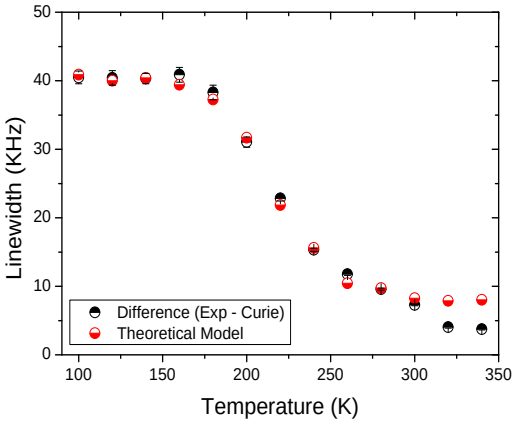

(a) (b)

Figure 3.31: a) ^{1}H nuclear linewidth temperature dependence for CD100 at 1.50 T corrected for the Curie contribution (black half up circles) and theoretical values estimated by the Fourier transform of Eq. 3.83 (red half down circles). b) ^{1}H $1/T_{1n}$ is reported for some concentrations of CD100 in liquid d-DMSO at 300 K at 1.50 T. The line is the best linear fit.

To perform a clear analysis of the nuclear linewidth, one has first to remove the paramagnetic contribution. Thus, by fitting the high-temperature points of Fig. 3.30b with $\mathrm{LW}_{Curie}(T) = C_C/T + constant$, it is possible to obtain the Curie contribution, which can then be subtracted to all the experimental points of Fig. 3.30b obtaining the black data in Fig. 3.31a. Then, by resorting to the free induction decay formula in the presence of molecular motion (Eq. 3.83, where τ_R, the correlation time, is $\tau_1 \exp E_A/T$, with τ_1 and E_A from the fit shown in Fig. 3.30a) one can apply the Fourier transform to evaluate the theoretical NMR spectrum and, consequently, the theoretical nuclear linewidth (red data in Fig. 3.31a). The good agreement between theoretical and corrected experimental data provide a further proof to the fact that the peak and the narrowing are due to molecular motion.

Since the **^{1}H nuclear spin-lattice relaxation time at room temperature in the solid phase is around 40 ms**, some liquid solution of CD100 in d-DMSO have been prepared to evaluate **the liquid phase relaxation time**. The use of a deuterated solvent allows to detect signal only from protons belonging to βCD's). As shown in Fig. 3.31b, the ^{1}H nuclear spin-lattice relaxation rate depends linearly on the CD100 concentration and, in the best case, is reduced by one order of magnitude, yielding relaxation times **of the order of 0.5 s**, too short for any molecular imaging application.

^{13}C High Temperature Relaxation

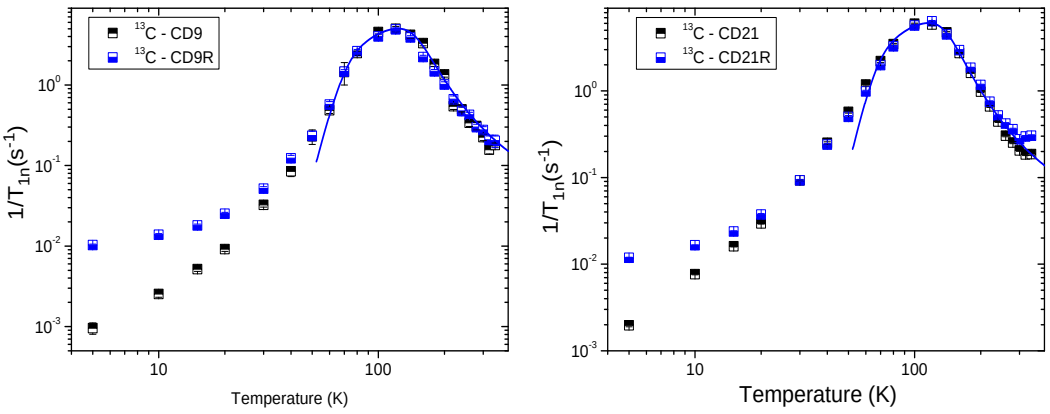

(a) (b)

Figure 3.32: a) ^{13}C $1/T_{1n}$ temperature dependence for CD9 (black half up squares) and CD9R (blue half down squares) at 6.95 T. Fit to CD9R data according to Eq. 3.82. b) ^{13}C $1/T_{1n}$ temperature dependence for CD21 (black half up squares) and CD21R (blue half down squares) at 6.95 T. Fit to CD21R data according to Eq. 3.82.

The high temperature ^{13}C $1/T_{1n}$ is reported for doped and undoped ^{13}C-labeled samples in Fig. 3.32 and 3.33 (technical details are given in Sec. A.1.2).

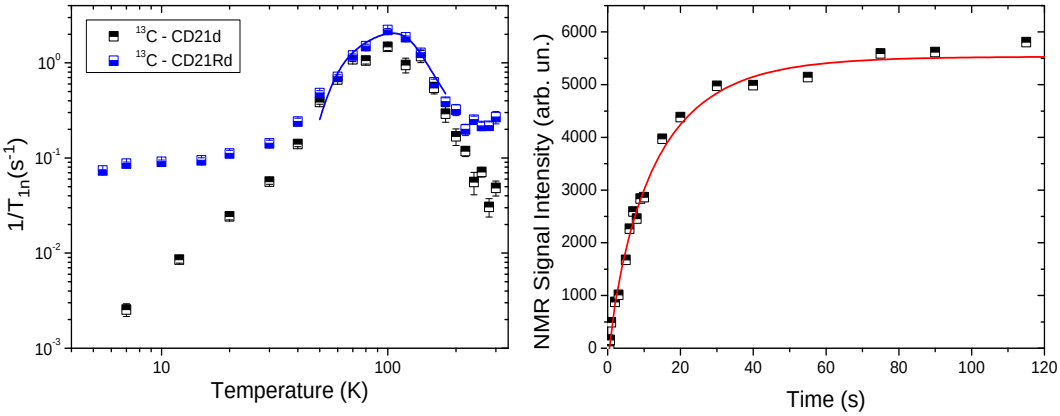

(a) (b)

Figure 3.33: a) ^{13}C $1/T_{1n}$ temperature dependence for CD21d (black half up squares) and CD21Rd (blue half down squares) at 3.45 T. Fit to CD21Rd data according to Eq. 3.82. b) Recovery of ^{13}C longitudinal magnetization in sample CD21d at 280 K at 3.45 T.

Since, proton relaxation is too fast at room temperatures, it is necessary to study ^{13}C spin dynamics in the high-temperature range. As shown by Fig. 3.32, CD9, CD9R, CD21 and CD21R display peaks in ^{13}C relaxation

Sample	n	$< \Delta h_{\perp}^2 >$ (T^2)	τ_1 (s)	E (K)	Δ (K)
CD100	^{1}H	$(6.9 \pm 0.6) \times 10^{-7}$	$(1.5\pm 0.8) \times 10^{-13}$	2570± 155	280± 25
CD9	^{13}C	$(1.4 \pm 0.1) \times 10^{-6}$	$(2.9\pm 0.1) \times 10^{-12}$	758± 45	268± 24
CD9R	^{13}C	$(1.5 \pm 0.1) \times 10^{-6}$	$(3.1\pm 0.7) \times 10^{-12}$	729± 28	247± 15
CD21	^{13}C	$(1.8 \pm 0.1) \times 10^{-6}$	$(2.3\pm 0.8) \times 10^{-12}$	740± 42	258± 22
CD21R	^{13}C	$(1.6 \pm 0.1) \times 10^{-6}$	$(3.9\pm 0.1) \times 10^{-12}$	693± 32	222± 18
CD21d	^{13}C	$(1.5 \pm 0.4) \times 10^{-7}$	$(9.0 \pm 0.1) \times 10^{-12}$	523 ± 144	243± 88
CD21Rd	^{13}C	$(2.1 \pm 0.2) \times 10^{-7}$	$(5.7\pm 3.3) \times 10^{-12}$	588± 60	227± 34

Table 3.7: Fit results according to Eq. (3.82) for all samples.

temperature dependence that can be fit using Eq. 3.82 with an average energy barrier around 700 K common to the four samples. This peak, like in case of CD100, is ascribed to molecular motion, specifically to CH_3 rotation: its position, height and width do not depend on the presence of the free radical, confirming the hypothesis of molecular dynamics. The effect of the free electron spins are clearly visible in the two tails of the peak, both at lower and higher temperatures. where ^{13}C nuclei in CD9 (6.3 s at 300 K) and CD21 (5.4 s at 300 K) relax slower than in the corresponding doped samples (CD9R 4.9 s at 300 K, CD21R 3.3 s at 300 K). **^{13}C relaxation in deuterated samples CD21d and CD21Rd still displays the molecular motion related peak, but yields longer relaxation times, in particular at room temperature in CD21d where ^{13}C T_{1n} reaches 30 s** (see Fig. 3.33). This is expected in case of DNP on samples where the compound of interest or the solvent have been deuterated: nuclear spin-lattice relaxation times can grow over 100 s [75, 89, 110, 255].

Summarizing Results

This chapter has been devoted to the study of the out-of-equilibrium hyperpolarized nuclear state that is achieved in DNP experiments. The numerical simulations of the EPR spectrum have demonstrated that the strength of the electron dipolar interaction (and thus the electron concentration) plays a key role in determining the regime that is attained. For low concentration the EPR spectrum displays a localized hole burning (in agreement with solid effect theory) while for high concentration a complete reorganization is noticed. For high enough MW power, the EPR spectrum shows a clear sign inversion (predicted by thermal mixing theory and seen in DNP experiments), while for low MW power it displays a huge depolarization, which is not predicted by any theory but it has been observed in experiments. Furthermore, the validity of the spin-temperature approach to describe DNP in the thermal mixing (both for high and low MW power) is demonstrated. On the other side, an experimental study on the DNP in βCD's samples doped with TEMPO free radical has been presented. A first batch, containing βCD's samples doped with variable amounts of TEMPO, has been used to demonstrate the possibility to efficiently hyperpolarize ^{1}H, whose polarization has been raised to 10 % in the

optimal case (1 % radical weight over total weight) within quite short polarization times (tens of seconds). The role of the free electrons has been found to be dominant in the low-temperature range (1.60 - 4.20 K), where nuclear spins relax through the hyperfine interaction, whose strength is modulated by low-frequency glassy modes, as suggested by the analysis of the temperature dependence of ^{1}H T_{1n}. By comparing T_{1n} and T_{POL} the ^{1}H hyperpolarization looks consistent with the thermal mixing regime. The second batch of samples has been prepared with random and total $^{13}CH_3$ methylation (9 or 21 methyl groups per molecules, respectively) at the fixed optimal concentration previously found. ^{13}C polarization has been raised to 7.5 % and better DNP performances have been obtained in samples with a larger number of ^{13}C atoms per molecules. The hyperfine interaction, driving both ^{1}H and ^{13}C nuclear spin-lattice relaxation, is strongly slowed in the samples with 21 methyl groups per molecule: this highlights the bottleneck effect affecting the nuclear relaxation mediated by electrons. In these second batch ^{1}H and ^{13}C hyperpolarization still looks consistent with the thermal mixing framework, even if some deviations appears. The third batch contains samples where deuterated methyl groups have been used to label the βCD's in order to study the effect of deuterium on the DNP process. ^{13}C polarization appears to be enhanced by deuteration, with values up to 10 % which is a remarkable result in view of molecular imaging or high resolution NMR spectroscopy, while the bottleneck effect affecting both ^{1}H and ^{13}C seems to be cancelled. In all the batches the high-temperature (5 - 340 K) nuclear relaxation rates have been found to be strongly influenced by the molecular motion and rotations inside the molecules, with broad peaks appearing in $1/T_{1n}$. ^{1}H relaxation times are shorter than 1 s at room temperatures, while deuteration of the compounds allow to increase ^{13}C ones from 3 - 6 s to 20 - 30 s at 300 K.

Chapter 4

Switching Electron Spin Polarization in Valence Tautomers

4.1 Introduction to Valence Tautomers

Valence tautomers (VT) are molecular compounds characterized by a transition involving an intramolecular electron transfer between a metal center (Vanadium, Manganese, Iron, Cobalt, Nickel, Copper, Ruthenium, Ytterbium) and a redox-active organic ligand (dioxolenes, diimines, amino-phenolates, phenoxyl, porphyrins, which should have a radical form accessible), leading to two stable magnetic states: a Low Spin (LS) and a High Spin (HS) one [151–159, 256, 257]. A transition between the two states might be induced by a series of external stimuli: temperature variation [156, 164, 256–260], pressure application [256, 261, 262], infrared/visible light [156, 164, 256, 257, 259, 260] and soft X-rays irradiation [263]. As shown in Fig. 4.1, the LS state is energetically favored and at low temperatures the molecules stay in this state. However, by increasing the temperature, there may be an entropy gain in promoting the system to the HS state (due to its higher density of vibrational states and to its larger degeneracy), which thus becomes the favored energy state thanks to the global thermodynamic balance [151, 159, 163, 164, 256, 261].

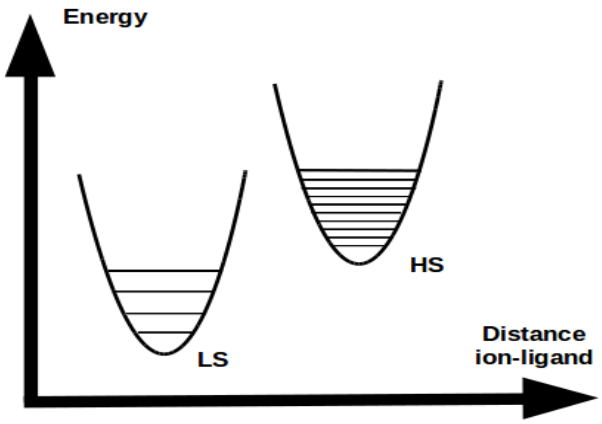

Figure 4.1: Schematic view of the fundamental energy levels HS and LS in valence tautomers.

The transition can be sharp or broad, depending on the phase of the sample (liquid or solid), on the cooperativity (i.e. on the intermolecular interaction) and on the choice of the solvent (and thus on the chemical pressure) used within the crystallization process [151, 159, 163]. The transition temperature, defined as the temperature at which half of the molecules are in the LS state and the other half in the HS state, may vary in the range 10 to 390 K, depending on the compound [163, 264, 265]. The pressure application has been demonstrated to induce the transition, mainly from HS to LS since the LS state has a lower volume (and a lower distance between the metal ion and the redox-active ligand [156, 159, 256, 262]) due to reduced population in the antibonding molecular orbitals. However, a striking role in inducing VT transitions is played by infrared/visible light irradiation that achieves the so-called photoinduced effect: light of appropriate wavelength may promote molecule from the LS state to an excited metastable state, with a subsequent fast relaxation to the HS state. At low temperatures, the molecules may be trapped in the HS state after light irradiation due to the light induced excited spin state trapping (LIESST): this trapping may last even for very long times (i.e. hours or days) [148, 149, 151, 159, 163, 164, 260]. Thermal relaxation back to the ground state may take place through tunneling processes, with decay times showing little or no temperature dependence, for T $<$ 20-25 K, or through phonon modes following the Arrhenius law for activated processes, with barrier around 100 to 400 K, for T $>$ 20-25 K [159, 164, 257, 259, 260]. However, it is also possible to induce the relaxation back to the LS state with external stimuli, either warming up the compound or irradiating again with a different wavelength this time. In the former case it is possible to define a temperature, called T_{LIESST}, at which the light-induced HS spin state has a very short lifetime. In the latter case, light promotes the molecules from the HS state to a metastable state, followed by a relaxation down to the LS state: this process in called reversed LIESST [164]. Furthermore, it has been shown that soft X-

rays can be used to stimulate the VT transition: even if the mechanism is still unclear it is likely that this process is due to the secondary electrons inelastic scattering [263].

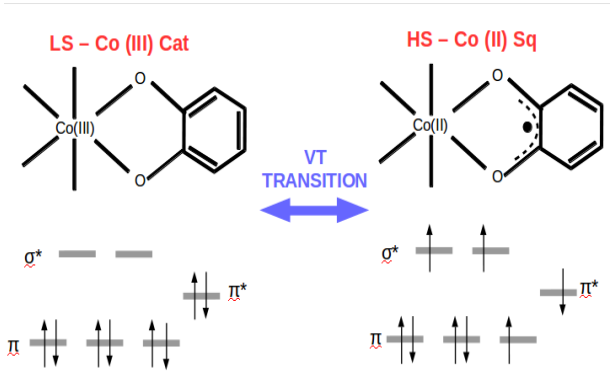

Figure 4.2: Schematic view of the charge distribution in the LS and HS state.

The magnetic bistability and the response to many external stimuli characterizing VT compounds make them suitable for a range of technological applications [151, 159, 256, 266]. Since the superparamagnetic limit prevents the miniaturization of magnetic data storage media, single VT molecules might be used to build "molecular" bits, where the fundamental information (0 or 1) is stored in the magnetic state of the molecule (LS or HS), while light irradiation might play the role of reading/writing. To implement this application it is necessary to address some questions, such as the lifetime of the HS state induced by LIESST and to analyze the spin dynamics characterizing molecules, in particular coherence times and magnetic fluctuations of the light-induced HS state. Another perspective is the realization of photo-switchable spintronics devices, where molecular material, like VTs, can mimic electronics behavior of circuits, since the miniaturization of electronic components gets more difficult and more expensive as nanoscopic sizes are approached. In this respect, molecules must be chemically stable, must mantain separate identity and, through photonics devices, should show good rate of logical operations. Other possible applications regard the use of VT as pressure sensor, exploiting the VT transition sensibility to the externally applied pressure, or as display devices fundamental units, since the VT transition is accompanied by a change of the optical properties, like color.

This thesis focuses on a particular VT compound, where the metal ion is Cobalt while the redox-active ligand belongs to the dioxolene group. The two ion spin states are a low spin LS-Co(III), that is coupled to the binegative diamagnetic (catecholate) state of the ligand (with two electrons in the π molecular orbital of the ligand), and an high spin HS-Co(II), that is coupled to the oxidized mononegative radical (semiquinonate) state of the ligand (with only one electrons in the π molecular orbital) [156, 159, 164, 166]. It is possible to switch between the two configurations by means of temperature variation (in

the range 100 to 200 K), light irradiation (at 910 nm) or pressure application [160–166, 259], thus providing different approaches to control the molecular spin state. The transition temperature is known to be $\simeq$ 160 K [156, 164] with a broad crossover due to two overlapping transitions which can be ascribed to two crystallographically inequivalent molecular sites in the lattice.

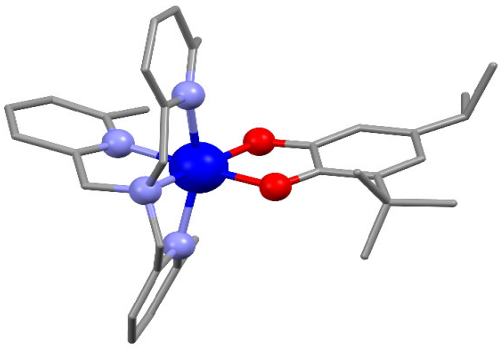

Figure 4.3: Molecular structure of the Cobalt:dioxolene complex. Color code: Cobalt (big blue ball), oxygen (red balls), nitrogen (violet balls), carbon (grey sticks). Hydrogen atoms are omitted for clarity

Since the technological applications mentioned above require the further addressing of VT magnetic properties, this chapter deals with a extensive physical study performed by using a macroscopic technique, SQUID magnetometry, and two local-probes techniques, NMR and μSR. First, SQUID experiments allow to analyze the magnetization of the compound in the LS and HS phase, as well as to study the effect of IR irradiation on the macroscopic magnetic properties, in particular to observe the magnetization growth under IR irradiation and the following relaxation: the former yields the conversion efficiency and the build-up time of the out-of-equilibrium light-induced state, the latter provides its lifetime. Then the NMR and the μSR experiments allow to get a deeper look at the microscopic environment, exploiting ^{1}H nuclei and muons as probes distributed quite homogeneously throughout the sample, and ^{59}Co, with their central positions in the molecules, to unravel the spin dynamics of the light-induced state and namely to probe the spin decoherence. These results are discussed in the framework of future data storage applications. Lastly, a brief discussion on SQUID and NMR measurement carried out in the presence of a variable external pressure is provided, related to pressure sensor applications.

The preparation method has been carried out following a previous article [164]. Even if the compound studied in this thesis is a powder, VT may be nanostructured on a solid substrate via wet chemistry strategies, while keeping the thermally- and optically-induced switchability at the nanoscale [166, 267].

4.2 Results

4.2.1 Effect of Light Irradiation on the Macroscopic Magnetization

To characterize the macroscopic magnetic properties in the LS and HS phases, SQUID experiments can be performed as a function of the temperature, yielding the magnetic susceptibility χ_M (technical details are given in Sec. A.2.2).

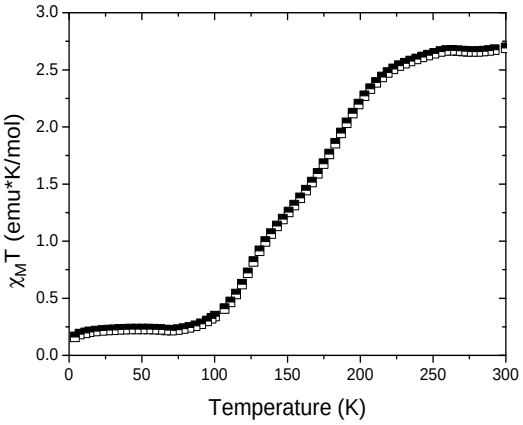

Figure 4.4: $\chi_M \cdot T$ temperature dependence for 0.1 T.

Fig. 4.4 shows the temperature dependence of $\chi_M \cdot T$ that allows a quantitative analysis of the the LS and the HS phases of the compound. As expected, a broad transition is observed, with $\chi_M \cdot T$ increasing when going from 100 K up to 200 K, in agreement with previous experimental results on the same compound [156, 164], with the two overlapping contributions. At high temperatures, i.e. above 200 K, a plateau at 2.67 emu·K/mol is found, corresponding to the phase where all molecules are in the HS configuration. The HS phase might be treated as a system of non-interacting paramagnets, whose magnetic susceptibility follows the Curie formula:

$$\chi_M \cdot T = \frac{g^2 \mu_B^2 S\,(S+1)\,N_A}{3K_B}, \tag{4.1}$$

where N_A is the Avogadro number and g $\simeq$ 2 the Landé factor. The Co(III) ion (S=$\frac{3}{2}$) and the radical species (S=$\frac{1}{2}$) can arrange into three possible configurations in the HS phase:

- a ferromagnetic coupling, yielding total spin S = 2 and $\chi_M \cdot T$ = 3.3 emu·K/mol;
- an uncoupled configuration, yielding $\chi_M \cdot T$ ranging from 2.7 to 3 emu·K/mol, that is the sum of the radical contribution (0.375 emu·K/mol) and of the metal ion (2.4 - 2.6 emu·K/mol, sum of the spin contribution equal to

1.875 emu·K/mol and of the orbital contribution, which depends on temperature [268]);

- an antiferromagnetic coupling, yielding total spin S = 1 and $\chi_M \cdot T = 1$ emu·K/mol.

Since the ferromagnetic and the antiferromagnetic contribution yields values much larger and much smaller, respectively, than the experimental one, it can be concluded that **the uncoupled configuration is the most likely for the HS state molecules**.

From Fig. 4.4 it is also evident that another plateau is found below 100 K, at 0.24 emu·K/mol, showing that in this phase most of the molecule are diamagnetic, since they are in the LS configuration (S = 0), but some still remain paramagnetic. The molecules in the LS phase, despite being diamagnetic, still yield a small contribution to $\chi_M \cdot T$, which is called $\chi_{LS} \cdot T$ and it is equal to 0.15 emu·K/mol. On the other hand it has been discovered that the contribution to $\chi_M \cdot T$ of the HS molecules (which is named $\chi_{PURE} \cdot T$) is not constant with temperature [268]. The HS molecules fraction which do not convert at low temperatures is then given by:

$$HS_{LT} = \frac{\chi_M - \chi_{LS}}{\chi_{PURE} - \chi_{LS}}. \tag{4.2}$$

It turns out that around 3 % of the molecules are in the HS phase at 5 K, in agreement with previous works [159, 164, 263, 269]. The presence of this remaining HS molecules will be probed by NMR and μSR, as discussed in the following paragraphs.

Examples of $\chi_M \cdot T$ growth under IR irradiation and decay after IR irradiation are given in Fig. 4.5 at 47 and 55 K, respectively.

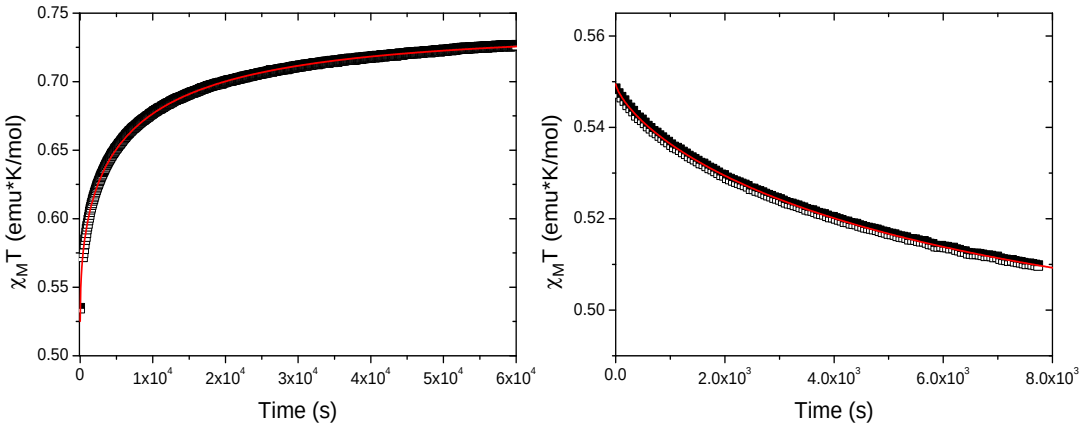

Figure 4.5: a) Growth of $\chi_M \cdot T$ as function of time passed after turning on IR irradiation at 47 K and for 0.1 T. Fit according to Eq. A.8. b) Decay of $\chi_M \cdot T$ as function of time passed after turning off IR irradiation at 55 K and for 0.1 T. Fit according to Eq. A.9.

The temperature dependences of the build-up rate and of the IR irradiation efficiency are shown in Fig. 4.6.

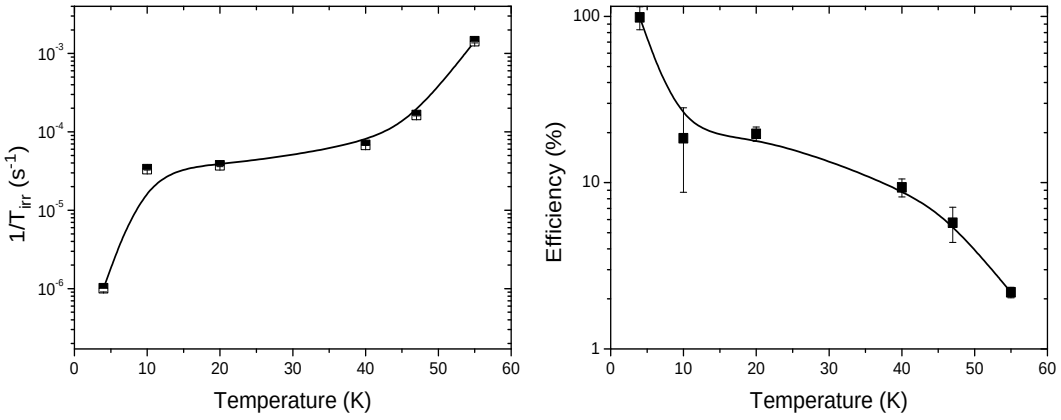

(a) (b)

Figure 4.6: a) Build-up rate temperature dependence for 0.1 T. The line is a guide to the eye. b) Irradiation efficiency temperature dependence for 0.1 T. The line is a guide to the eye.

Fig. 4.6a reports the relationship between IR irradiation efficiency and the related build-up time, while Fig. 4.6b shows the temperature dependence of the decay time.

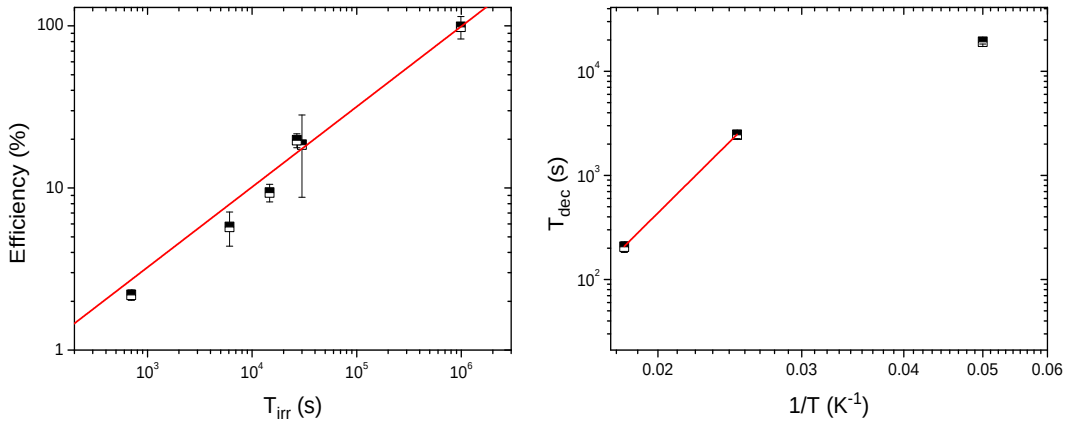

(a) (b)

Figure 4.7: a) Irradiation efficiency over build-up time for 0.1 T. Fit according to $y\,(T_{irr}) = aT_{irr}^{b}$. Fit parameters: a $= 0.11 \pm 0.03\ \mathrm{s}^{-1}$ and b $= 0.48 \pm 0.02$. b) Decay time temperature dependence for 0.1 T.

Fig. 4.5 shows that **IR irradiation can efficiently promote molecules from the LS to the HS state** [164, 260, 270–272], resulting into the magnetic susceptibility growth (up to a value $\chi_0 \cdot T$) which can be fit by Eq. A.8. The

build-up times can reach several hours at low temperatures (see Fig. 4.6a), which is not uncommon [260], while the low stretching coefficient value, around 0.5 - 0.6, accounts for a wide distribution of build-up times. The conversion efficiency is:

$$\epsilon = \frac{\chi_0 - \chi_M}{\chi_{PURE} - \chi_M} \tag{4.3}$$

and it is found to increase (approaching 100 %) as the temperature is decreased as shown in Fig. 4.6b. The incomplete conversion may be due either to opacity of the sample, to the non-perfect irradiation geometry or to the thermal relaxation. From Fig. 4.7 it is possible to state the **high conversion efficiency are associated with very long build-up times** in the bulk phase of the sample, following a power-law.

Thermal relaxation plays a fundamental role in the decay of the magnetic susceptibility back to the thermal equilibrium value, after IR irradiation is switched off. As reported elsewhere [164], this decay (Fig. 4.5b) is fit using a stretched exponential law, with a stretching exponent varying from 0.3 at 55- 40 K to 0.8 at 20 K. As previously mentioned, there are two main sources of relaxation: the tunneling processes and the phonon-driven processes. The latter is characterized by an activated law [259, 262] for T > 20 - 25 K:

$$T_{dec}(T) = T_0 \exp \frac{\Delta E}{K_B T}, \tag{4.4}$$

with ΔE the energy barrier, which in our case is equal to 350 K (Fig. 4.7b), in agreement with previous experimental results [164]: this is the energy barrier separating the LS and the HS state. For T < 20 K, on the other hand, tunneling processes are much slower: **the lifetime of the light-induced HS state is quite long and the molecules will stay out-of-equilibrium up to 7 hours**. Our results are in good agreement with previous studies based on the Density Functional Theory aimed at computing the energy barrier between the LS and the HS state in many Co-based VT's [273–276].

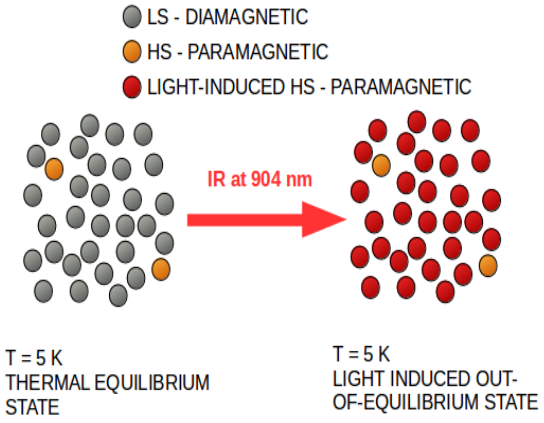

Figure 4.8: Schematic view of the IR-induced transition at low temperatures. Left: almost all molecules are diamagnetic (grey circles) in a thermal equilibrium condition at 5 K, while only few are paramagnetic (orange circles). Right: IR irradiation promotes the molecules to the HS paramagnetic state (red circles), generating an out-of-equilibrium state.

4.2.2 Probing the Local Spin Fluctuations

To get a deeper look on the spin dynamics characterizing the sample it is necessary to use local probes techniques. ^{1}H nuclear spin-lattice relaxation rate temperature dependence is shown in Fig. 4.9 at different magnetic fields and in the presence or in the absence of IR irradiation (technical details are given in Sec. A.1.2). The NMR results (Fig. 4.9a) show that in the range 100 to 200 K ^{1}H $1/T_{1n}$ doubles its magnitude (from 25 to 50 s^{-1}) at all the static fields used. This is clear evidence that protons, which can be found in the organic ligands surrounding the Cobalt ion, are quite sensitive to the hyperfine field generated by the HS state, whose mean square fluctuations amplitude are changed upon the VT transition. Above 200 K $1/T_{1n}$ is almost constant, as expected for weakly coupled spins [7]. Furthermore, the weak static field dependence observed in the high-temperature range is probably due to molecular motion or to low-frequency diffusive spin fluctuations, similar to those observed in low-dimensional paramagnets [277, 278].

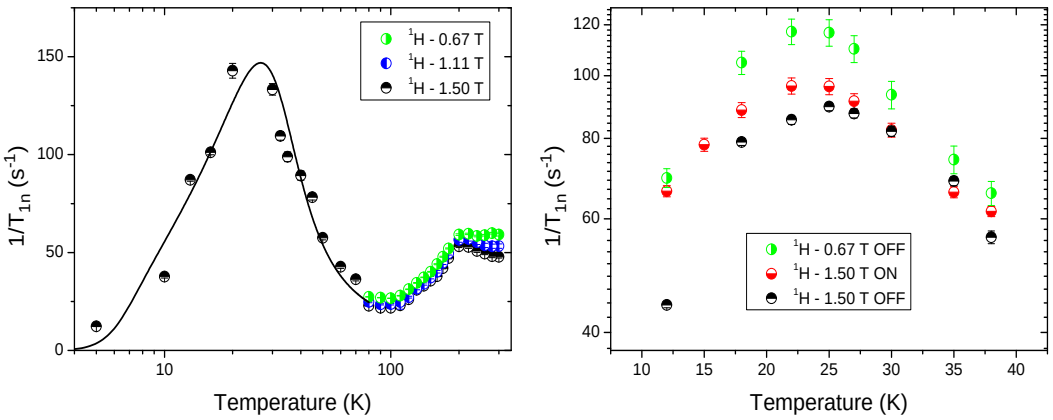

Figure 4.9: a) ^{1}H $1/T_{1n}$ temperature dependence at 1.50 T (black half up circles), 1.11 T (blue half left circles) and 0.67 T (green half right circles). Fit according to Eq. 3.82. Fit parameters are: $\langle \Delta h_\perp^2 \rangle = (2.8 \pm 0.4) \cdot 10^{-6}$ T^2, $\tau_1 = (3.5 \pm 0.8) \cdot 10^{-11}$s, $E_A = 90 \pm 12$ K, $\Delta = 60 \pm 10$ K. Cooling rate = 1 K/min. b) ^{1}H $\frac{1}{T_{1n}}$ temperature dependence at 1.50 T with light off (black half up circles), at 1.50 T with light on (red half down circles) and at 0.67 T with light off (green half right circles). Cooling rate = 6 K/min.

Below 100 K, $1/T_{1n}$ displays a very high peak centered around 20 - 25 K, due to the slowing down of the magnetic fluctuation of the molecules which are in the HS state despite the low temperatures (orange circles in Fig. 4.8), whose frequency approaches the proton Larmor frequency. The peak intensity increases by decreasing the static field, as observed in Fig. 4.9b. Thus **the HS molecules are still characterized by magnetic fluctuation with frequencies in the MHz range in the low temperature range**, due to the fact that the HS energy level is not sharp, but it is rather a band of

sublevels where the magnetic fluctuation of the HS state corresponds to transitions between these sublevels. If one uses the Boltzmann factors to describe the population distribution on these sublevels then the peak of Fig. 4.9a can be fit with Eq. 3.82, where E_A is the energy barrier involved in the HS magnetic fluctuation. The fit yields an energy barrier equal to 90 K with a width equal to 60 K. Fig. 4.9b also reports **the effect of the IR irradiation on the sample: $1/T_{1n}$ is found to slightly increase, due to the enhanced local fields probed by protons**. However, irradiation in NMR experiments is not trivial, since one has to irradiate a bulk sample with a non negligible opacity. Furthermore, ^{1}H $1/T_{1n}$ only doubles when all the molecules go from the LS to the HS state, thus the effect on $1/T_{1n}$ is expected to be small.

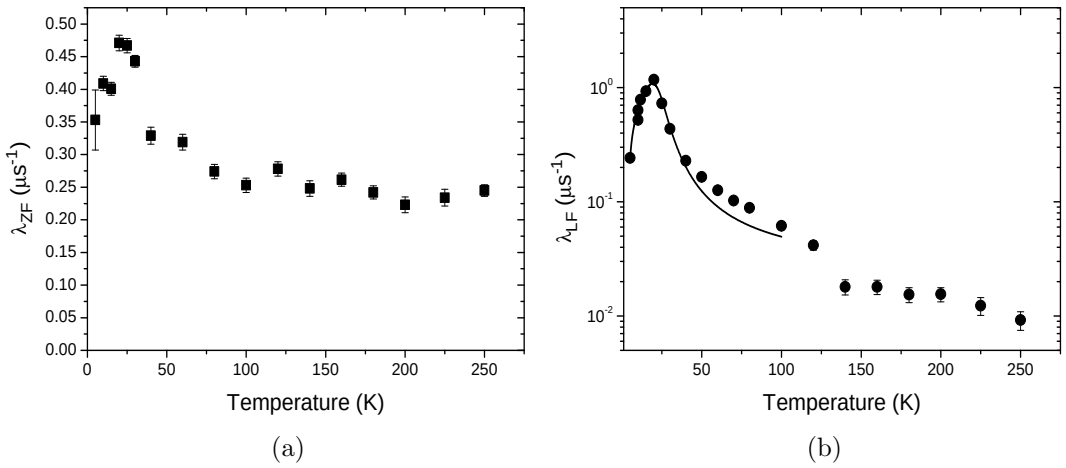

Figure 4.10: a) Muon λ_{ZF} temperature dependence in Zero Field experiments. b) Muon λ_{LF} temperature dependence in 200 Gauss longitudinal field experiments. Fit according to Eq. 3.82. Fit parameters are: $\langle \Delta h_\perp^2 \rangle = (3.2\pm0.1)\cdot10^{-10}$ T^2, $\tau_1 = (1.5\pm0.9)\cdot10^{-10}$s, $E_A = 77\pm5$ K, $\Delta = 54\pm4$ K.

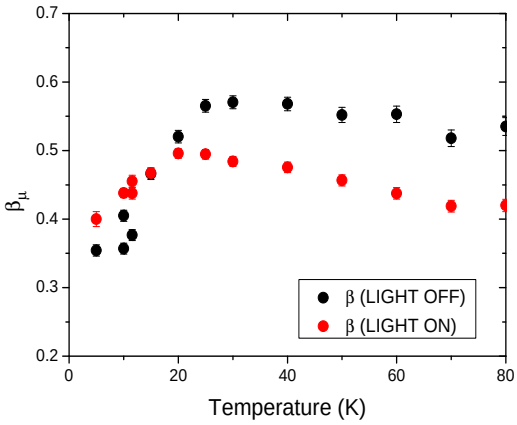

Figure 4.11: β_{LF} temperature dependence in 200 Gauss longitudinal field experiments in the presence (red circles) and in the absence (black circles) of IR irradiation.

Muon spin-lattice relaxation rate temperature dependence is given in Fig. 4.10 for ZF and LF experiments, while the effect of IR irradiation is shown in Fig. 4.11 for LF experiments (technical details are given in Sec. A.4.2).

A comparison with ^{1}H NMR results can be made by looking at the μSR experiments, since muons are implanted homogeneously in the sample, thus having a spatial distribution similar to those characterizing protons. The ZF experiments (Fig. 4.10a) is not sensitive to the VT transition in the range 100 to 200 K, because the spin dynamics is too fast with respect to the muon lifetime, while in the range 10 - 50 K a peak is observed. Both features are amplified in the LF experiments performed at 200 Gauss: the VT transition is characterized by and increase of the muon λ_{LF}, as opposed to ^{1}H $1/T_{1n}$, while the peak in the range 10 - 50 K is much more evident. By fitting this latter with Eq. 3.82, one obtains an energy barrier equal to 77 K and a width equal to 54 K, in good agreement with the ^{1}H NMR results, demonstrating **the muons are sensitive to the magnetic fluctuations of the HS molecules**.

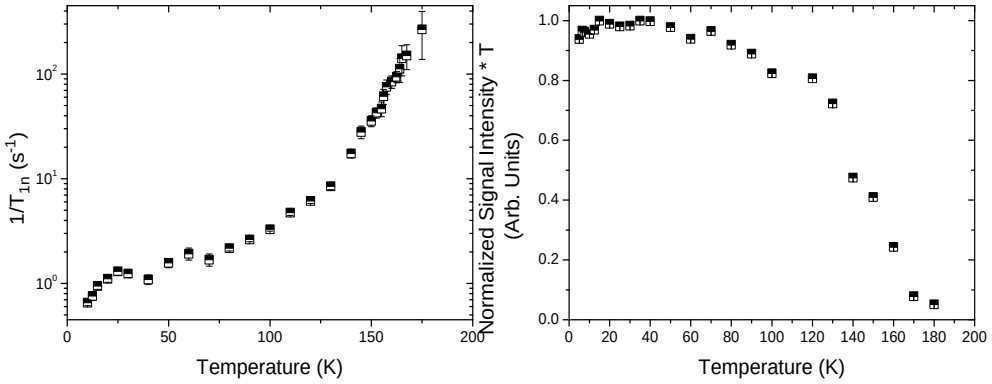

(a) (b)

Figure 4.12: a) ^{59}Co $1/T_{1n}$ temperature dependence at 6.95 T. b) ^{59}Co NMR signal intensity, multiplied by temperature, over temperature at 6.95 T.

The presence of this kind of peak is common to other systems like spin-crossover [279], samples characterized by spin freezing [280, 281] and molecular magnets [282–286]. The effect of IR irradiation in μSR experiments is only evident by looking at the temperature dependence of β_{LF}: the stretching coefficient is found to decrease upon IR irradiation.

A closer sight on the spin dynamics of the HS state may be obtained by looking at the ^{59}Co NMR results, since **the Cobalt ion has a central position in the molecule and it is more sensitive to the hyperfine coupling** (technical details are given in Sec. A.1.2). ^{59}Co nuclear spin-lattice relaxation rate temperature dependence is shown in Fig. 4.12a at 6.95 T and in the presence or in the absence of IR irradiation, while ^{59}Co signal intensity temperature dependence is given in Fig. 4.12b. The effect of IR irradiation is reported in Fig. 4.13a, while Fig. 4.13b depicts the difference between ^{59}Co

	$\delta h_{\perp}^2 (T^2)$	$\tau_0(s)$	$E_A(K)$	$\Delta(K)$
^{1}H OFF	$2.8 \pm 0.4 \cdot 10^{-6}$	$3.5 \pm 0.8 \cdot 10^{-11}$	90 ± 12	60 ± 10
LF μSR	$3.2 \pm 0.1 \cdot 10^{-10}$	$1.5 \pm 0.9 \cdot 10^{-10}$	77 ± 5	54 ± 4
^{59}Co OFF	$4.1 \pm 0.9 \cdot 10^{-7}$	$1.7 \pm 0.1 \cdot 10^{-10}$	53 ± 16	43 ± 17
^{59}Co ON	$1.8 \pm 0.3 \cdot 10^{-6}$	$1.1 \pm 0.5 \cdot 10^{-10}$	74 ± 17	60 ± 17
^{59}Co DIF.	$1.4 \pm 0.3 \cdot 10^{-6}$	$5.6 \pm 3.8 \cdot 10^{-11}$	88 ± 20	72 ± 18

Table 4.1: Fit results according to Eq. 3.82 for ^{1}H, muon and ^{59}Co relaxation data.

nuclear spin-lattice relaxation with and without IR irradiation.

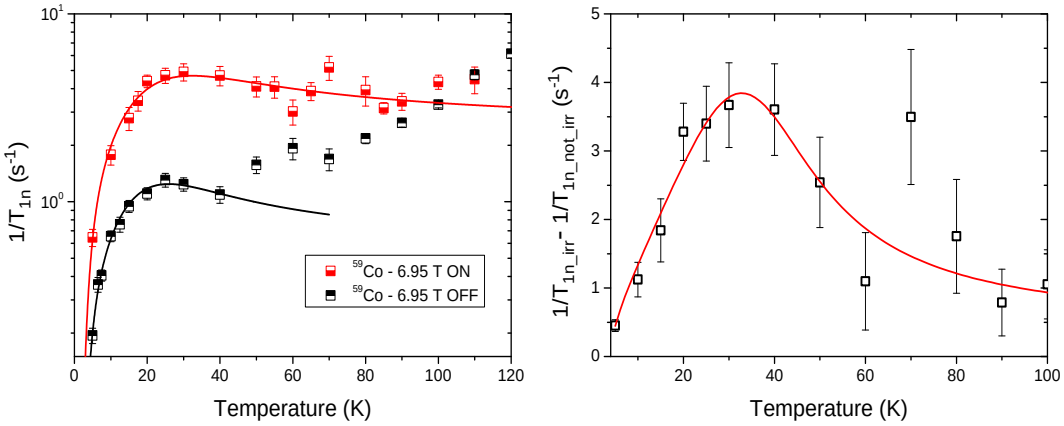

Figure 4.13: a) ^{59}Co $1/T_{1n}$ temperature dependence at 6.95 T in the presence (red half down squares) and in the absence (black half up squares) of IR irradiation. Fit according to Eq. 3.82. Fit parameters are: IR ON, $\langle \Delta h_{\perp}^2 \rangle = (1.8 \pm 0.3) \cdot 10^{-6}$ T^2, $\tau_1 = (1.1 \pm 0.5) \cdot 10^{-10}$s, $E_A = 74 \pm 17$ K, $\Delta = 60 \pm 17$ K ; IR OFF, $\langle \Delta h_{\perp}^2 \rangle = (4.1 \pm 0.9) \cdot 10^{-7}$ T^2, $\tau_1 = (1.7 \pm 0.1) \cdot 10^{-10}$s, $E_A = 53 \pm 16$ K, $\Delta = 43 \pm 17$ K. b) Difference between ^{59}Co $1/T_{1n}$ in the presence and in the absence of IR irradiation at 6.95 T. Fit according to Eq. 3.82. Fit parameters are: $\langle \Delta h_{\perp}^2 \rangle = (1.4 \pm 0.3) \cdot 10^{-6}$ T^2, $\tau_1 = (5.6 \pm 3.8) \cdot 10^{-11}$s, $E_A = 88 \pm 20$ K, $\Delta = 72 \pm 20$ K.

By looking at Fig. 4.12a it is found that $1/T_{1n}$ decreases by two orders of magnitude when warming the sample from 50 to 180 K, i.e. when inducing the transition from the LS to the HS state. Above 180 K the ^{59}Co disappears (Fig. 4.12b), due to the fact that **with NMR only the Cobalt nuclei belonging to the LS molecules can be detected because those in the HS molecules relax too fast**. Furthermore, ^{59}Co relaxation is unexpectedly faster than ^{1}H since the large difference in the gyromagnetic ratio would suggest the opposite. However, ^{59}Co relaxation in the LS molecules might be enhanced by ^{59}Co relaxation of the HS molecules through spin diffusion, leading to the high $1/T_{1n}$ values shown in Fig. 4.12a. On the other hand, in the low-temperature range a small peak in $1/T_{1n}$ temperature dependence is observed, which can be fit again using Eq. 3.82: the fit yields an energy barrier equal to 53 K and a width equal to 43 K, in agreement with the fit results on ^{1}H and muons. IR irradiation at low temperatures (Fig. 4.13a) enhances ^{59}Co

relaxation by a factor 4 to 5, while reducing at the same time ^{59}Co NMR signal intensity. **The increase in the number of HS molecules makes Cobalt nuclei in LS molecules relax faster through spin diffusion, while there are less LS molecules and thus the overall signal intensity is reduced**. However, the light-enhanced $1/T_{1n}$ is still smaller than the $1/T_{1n}$ at 180 K, underlining that the conversion efficiency is not high, due to the same problems affecting the irradiation setup in the ^{1}H NMR experiments. Even in the presence of IR irradiation, a small peak can be observed (Fig. 4.13a) and fit again using Eq. 3.82: the energy barrier turns out to be 74 K and the width 60 K, values similar to those obtained before. Now, to evaluate the spin dynamics of the HS states promoted by IR (red circles in Fig. 4.8), one can take the difference between the ^{59}Co $1/T_{1n}$ in the presence (orange plus red circles in Fig. 4.8) and in the absence (orange circles in Fig. 4.8) of IR: as reported in Fig. 4.13b this difference is still characterized by a small peak around 20 to 25 K, whose fit yields an energy barrier around 90 K and a width around 70 K. Thus **there is a persistent spin dynamics of the light-induced HS state in the MHz range at very low temperatures**, demonstrating the existence of magnetic fluctuations which will have to be removed in view of possible applications in magnetic data storage applications.

4.2.3 Pressure Effect

The effect of pressure application on $\chi_M \cdot T$ temperature dependence and on ^{1}H nuclear spin-lattice relaxation rate are reported in Fig. 4.14a and 4.14b, respectively.

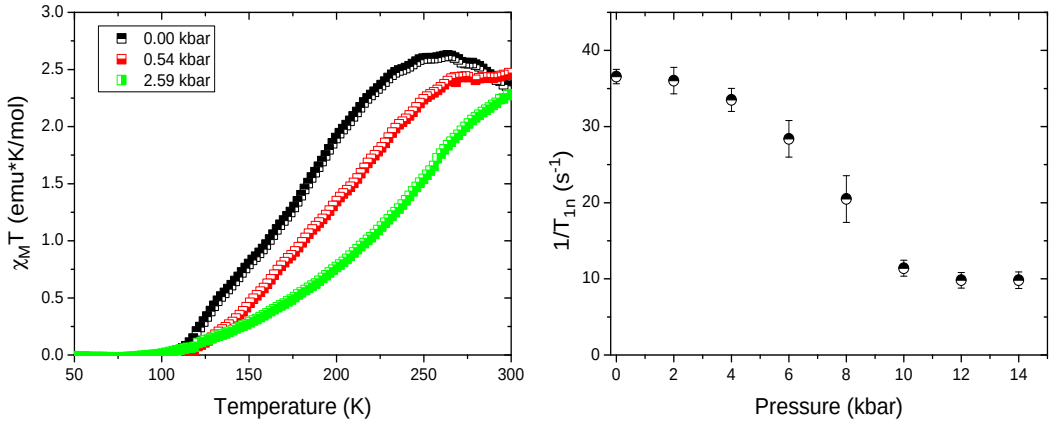

(a) (b)

Figure 4.14: a) $\chi_M \cdot T$ temperature dependence for different values of external applied pressure: 0.00 kbar, i.e. ambient pressure, black half up squares; 0.54 kbar, red half down squares; 2.59 kbar, green half right squares. The three measurement shown have been carried out inside the pressure cell and they are affected by its diamagnetic contribution. b) ^{1}H 1 T_{1n} pressure dependence at 300 K and for a 4.69 T.

It is worth mentioning the effect of pressure on VT compounds as they are good candidates for sensors. From Fig. 4.14a it is noticed that **a moderate application of pressure (few kbar) can shift the transition temperatures towards larger values (up to room temperature)**, mainly because the LS, being characterized by a smaller distance between the metal ion and the organic ligand, has a smaller volume and it is thus favored when external (but also chemical) pressure increases [156, 159, 256, 262]. Furthermore, the effect of pressure is much more marked in this compound with respect to the dinuclear cobalt-based VTs [262], which have two Cobalt ion per molecule. Fig. 4.14b shows the effect of pressure application to the ^{1}H $1/T_{1n}$ at 300 K: it is noticed that when external pressure increases to few kbar the proton relaxation gets slower, suggesting that an HS to LS transition has been induced, in agreement with the SQUID experiments.

4.2.4 Summarizing Results

This chapter has been devoted to the analysis of the macroscopic and microscopic magnetic properties of a Cobalt-based valence tautomer compound, in particular to focus on an out-of-equilibrium state induced by external stimuli. The SQUID magnetometry experiments have demonstrated that the paramagnetic HS phase of the molecules (above 200 K) is due to an uncoupled configuration between the spin of the metal ion and the one of the radical species. On the other hand, the diamagnetic LS phase (below 100 K) is characterized an incomplete conversion and a small fraction (3 to 5 %) of the molecules still remain paramagnetic. This feature has been confirmed by the μSR and NMR experiments where the muons, ^{1}H and ^{59}Co relaxation rates display a peak around 20 - 25 K due to the slowing down of the magnetic fluctuations (in the MHz range) of the abovementioned remaining HS molecules. These fluctuations have an energy barrier around 60 - 90 K and a width around 40 - 60 K. The SQUID experiments carried out in the presence of IR irradiation in the low-temperature range (4 - 60 K) have shown that IR light stimulates the LS to HS state transition and the magnetization grows asymptotically to a plateau value that represents the light-induced out-of-equilibrium state. High conversion efficiencies, close to 100 % at 4 K, are obtained but at the same time they need very long build up times (up to 20 hours). The lifetime of this out-of-equilibrium state can reach several hours. IR irradiation effects have been studied also within NMR experiments, where both ^{1}H and ^{59}Co relaxation rates are found to increase upon irradiation between 4 and 60 K. In particular, ^{59}Co have demonstrated that the light-induced HS states are still characterized by magnetic fluctuations in the MHz range. Finally the effect of pressure has been studied by means of SQUID and ^{1}H NMR experiments, showing that application of moderate pressure (2 - 14 kbar) at room temperature promotes the system from the LS to the HS state.

Chapter 5

Conclusions

In this thesis the magnetic properties of nuclear and electron spin systems brought out-of-equilibrium by external electromagnetic wave irradiation have been studied. The first part of the thesis has been devoted to the nuclear hyperpolarization of βCyclodextrins molecules doped with a nitroxide free radical under microwave irradiation, while the second part has treated the light-induced pressure-induced magnetic transition in a Cobalt-based valence tautomer.

The exact EPR spectrum simulations have underlined the key role played by the electron concentration in determining the DNP regime and how they behave when brought to an out-of-equilibrium state. For low concentrations, 1.5 mM, the EPR spectrum displays a localized hole burning that becomes broader as MW power is increased, in agreement with the solid effect. On the other hand, at high concentrations, around 15 mM, the EPR spectrum shows a complete reorganization: for low MW power it displays a huge depolarization while for high MW power the sign inversion predicted by thermal mixing theory appears. It has been thus demonstrated that in case of high free radical concentrations sign inversion can be obtained only through an efficient MW saturation. In addition, EPR spectrum can be well reproduced in the spin temperature approach only in the high concentration limit, where both the sign inversion and the huge depolarization are found. This study has thus clarified some unclear features from DNP experiments (the huge depolarization was used as an argument to invalidate the spin-temperature approach) and some incomplete aspects of DNP theory (the phenomenological electron spectral diffusion can be implemented exactly with the microscopic electron dipolar interaction). Furthermore, the EPR spectrum simulations has shown that low spin temperatures (i.e. high levels of hyperpolarization) can be achieved arranging the electrons in a ordered cubic lattice. This apparently contradicts the evidence that in some experiments only amorphous samples are efficiently polarized in DNP, while crystalline samples not (though there are examples of crystalline compounds efficiently polarized [287]). The conclusion is that DNP success is granted if the distribution of free radical is sufficiently homogeneous,

no matter if the free electrons are arranged randomly or on an ordered lattice. However, in crystalline samples, the radical are forced to accumulate between the different crystal grains and thus cannot arrange on a perfect ordered lattice: the sample is thus divided in radical rich (grains boundaries) and radical poor (grains) zones and the free radical distribution is far from being homogeneous.

The NMR - DNP experiments have demonstrated the possibility to efficiently hyperpolarize ^{1}H and ^{13}C in βCyclodextrins macromolecules, paveing the way for future research in order to optimize the DNP performances and to use these compounds for in vivo MRI. In particular ^{13}C polarization has been raised up to 10 % in the best case, which is quite an impressive value considering the novelty of this work and comparing it to previous DNP works on other substrates. An interesting technique which could be used to increase ^{13}C DNP polarization is the cross polarization, which is a transfer of polarization from hyperpolarized ^{1}H to ^{13}C spins by means of a train of RF pulses, since its power has already been proven [116, 119, 255]. The room temperature ^{13}C spin-lattice relaxation time, which has reached up to 30 s, represents a good starting point for in vivo studies, even if longer relaxation times would be desirable. In this regard a possible perspective could be the study of DNP hyperpolarization in βCD's labelled with carbonyl groups containing ^{13}C atoms: in this chemical configuration ^{13}C usually has longer relaxation times (over 60 s) at 300 K [75] thus allowing to exploit the hyperpolarized out-of-equilibrium state for a broader range of physiological processes within dissolution DNP experiments [59]. However, due to the huge number of βCD's application in chemistry and pharmacology, the experimental results presented here could represents a first step towards combined DNP/high resolution NMR experiments to study chemical reactions involving βCD's. In this sector a key role could be played by ^{1}H which is suitably hyperpolarized as well (P $\simeq$ 10 %) but whose short room temperature relaxation times prevent from exploiting it for MI applications. This feature could be useful in the investigation of the diffusion and the release of drugs which are stored in hydrogels of CD based polymers, using high resolution magic angle spinning NMR spectroscopy [288–290]. In particular, NMR sensitivity in these low concentration systems could be enhanced by adding small amounts of βCD's linked with a TEMPO unit and by irradiating with MW at a proper frequency. A striking feature, regardless of the specific applications, is represented by the short polarization times (around tens of seconds) which are needed to hyperpolarize ^{1}H and ^{13}C.

From a fundamental point of view, ^{1}H and ^{13}C hyperpolarizations look consistent with the thermal mixing framework since the linear relation between $1/T_{1n}$ and ^{1}H $1/T_{POL}\,(1 - P_S^2)$ is found in all samples. This was expected since TEMPO is a broad EPR spectrum free radical, belonging to the nitroxides family, and its linewidth is larger than the nuclear Larmor frequencies involved. However, clear deviations which shift the experimental points far below the TM prediction are observed and explained resorting to the bottleneck effect affecting the nuclear spin-lattice relaxation: nuclear relaxation is caused by the

hyperfine interaction and thus the nuclei can exchange energy with the lattice only via the electron spins. When one increases the degree of methylation at fixed free radical concentration (from CD9R to CD21R) the number of nuclei increases while the number of electrons keep constant and the ratio N_I/N_S strongly decreases. Since the nuclear spin-lattice relaxation rate is proportional to this ratio, it is clear that the increase in the number of nuclei causes a bottleneck effect slowing down the relaxation process. This aspect underlines the complexity of the DNP process and how it depends on several parameters. Finally, the effect of deuteration of the methyl groups increased the ^{13}C DNP polarization and allowed to reach longer relaxation times at room temperature, as expected [75, 89, 110, 255]. Remarkably, a striking feature is the disappearance of the bottleneck effect in sample CD21Rd, suggesting that deuterium nuclei are involved in some kind of interaction which make both ^{1}H and ^{13}C relax faster than in sample CD21R. A possible perspective could be the study of deuterium spin dynamics as well as its possible DNP hyperpolarization to get further information about the microscopic environment. Another point that has to be remarked is that the thesis has clearly demonstrated changes in the chemical environment of βCD's molecules can positively or negatively affect the DNP process and performance. In this respect it could be stimulating to study hyperpolarization also in α and γ CD's to check any effect of the molecular size on $1/T_{1n}$ and $1/T_{POL}$, as well as to observe the maximum ^{1}H and ^{13}C DNP polarization levels.

In the second part of the thesis the light-induced or pressure-induced out-of-equilibrium state in a Cobalt based valence tautomer compound has been studied using macroscopic (SQUID magnetometry) and microscopic (μSR and NMR) techniques to investigate its magnetic properties for technological applications, namely data storage and pressure sensors. A first set of SQUID experiments has demonstrated the all VT molecules are in the paramagnetic HS phase above 200 K, with Cobalt ion spin decoupled from the radical spin. Cooling below 200 K one observes a broad transition, centered around 160 K, with most molecules turning into a diamagnetic LS phase and the magnetic susceptibility clearly dropping to a lower value. The transition is also confirmed by the μSR and NMR results, in particular by ^{59}Co relaxation rate, that drops by two orders of magnitudes between 180 and 100 K, highlighting the high sensitivity of this nuclear species in detecting the local magnetic fields. Below 100 K, the magnetic susceptibility is still positive, demonstrating that a tiny fraction of the molecules remains in the HS state, probably due to the presence of local defects. The slowing down of the frequency of the magnetic fluctuations results in a high peak observed in the muons as well as in the ^{1}H ^{59}Co relaxation rates. The characterization of the thermal equilibrium magnetic properties of this compound underlines that quite fast spin dynamics is persistent despite the low temperatures. SQUID experiments have been carried out in the presence of the IR light irradiation to study the spin dynamics of the molecules once they are converted to HS out-of-equilibrium state. This conversion in-

volves a high efficiency, close to 100 %, and the corresponding build-up time is large, reaching even several hours. The lifetime of this out-of-equilibrium state has been measured by following the decay of the light-induced magnetization after switching off the IR irradiation and it is long as well, around 7 to 8 hours. To get a closer look at the spin dynamics in the presence of IR irradiation, μSR and NMR have been carried out while irradiating the sample with IR irradiation. Even if muons are not very sensitive to the light-induced transitions, ^{1}H ^{59}Co relaxation rates are found to increase, due to the fact that the nuclei probe larger amplitudes local magnetic fields since the number of HS molecules is now increased. ^{59}Co data have also showed that the light-induced HS state at 20 K is still characterized by magnetic fluctuations in the MHz range with coherence times shorter than 1 s. These results demonstrate that the application of these molecules as logic units in magnetic memories already presents some advantages (high conversion efficiency and long lifetimes of the out-of-equilibrium state) but still has to deal with important problems related to the short spin coherence which badly affects the storage of the information. A first solution could be working on the molecular design and changing the energy levels structure of the HS state in order to increase the energy barrier characterizing the HS state, possibly with the support of numerical simulations of the energy diagram of the system. Furthermore, it must be remarked that this study has been performed on a bulk sample, while any logic units application needs molecules arranged on particular 3D architectures. In this regards a similar study could be performed on a thin film of VT molecules to evaluate their mutual interactions and the interaction with the substrate as well as the spin dynamics under IR irradiation. Finally, the effect of pressure has been studied both by SQUID magnetometry and ^{1}H NMR: application of moderate pressures shifts the transition curves to higher temperatures, since the LS state has a smaller volume and it is thus energetically favored in this condition. Accordingly, the ^{1}H is found to decrease. These results show that VT molecules are promising candidates for everyday life pressure sensors.

Appendix A

Experimental Techniques

In this appendix the experimental techniques and sequences employed in the thesis will be described.

A.1 Nuclear Magnetic Resonance

A.1.1 Instrumentation

All the NMR experiments have been performed in the NMR laboratory of the Department of Physics at the University of Pavia (Pavia, Italy), except for the high pressure NMR measurements, that have been carried out at the Jožef Stefan Institute (Ljubljana, Slovenia). The following equipment has been employed:

- a superconducting magnet and an electromagnet, which can produce magnetic fields up to 9 and 2 T, respectively;
- an Apollo (Tecmag) spectrometer 5 - 450 MHz;
- homemade NMR probes with solenoidal coils (for the ordinary NMR experiments);
- a MW source (Gunn diode, irradiation range 95-98 GHz) (for the DNP measurements);
- two IR LED's (Thorlabs LED910E-AlGaAs: wavelength = 910 ± 10 nm, power = 12 mW, AC current = 16 mA) (for the IR light irradiation NMR measurements);
- flux cryostat, cooled with liquid nitrogen or helium, for the 5 - 340 K temperature range, while a bath cryostat and an adiabatic helium pump for the range 1.60 - 4.20 K.

NMR-DNP MW irradiation experiments

The NMR-DNP experiments have been carried out using a special homemade probe, with a MW sourced integrated and a saddle coil, to allow the complete MW irradiation of the sample. The cooling procedure was a flash freezing into liquid nitrogen (77 K), followed by a quick cooling down to 4.20 K with liquid helium. A slower cooling procedure (from 300 to 4.20 K) has been found to badly affect the DNP performances. The magnetic field used has been 3.41 to 3.45 T, with ^{1}H and ^{13}C Larmor frequencies equal to 147 and 37 MHz, respectively.

NMR Light irradiation experiments

The NMR irradiation has been performed as ordinary NMR experiments, with the addition of two LED's irradiating the sample. Concerning ^{59}Co, a rectangular single spire coil has been used, with the sample inside a rectangular and thin sample holder to allow maximum irradiation. Two LED's have been mounted perpendicular to the coil and powered with 15 mA each. In the case of ^{1}H, a similar setup has not been employed due to very high background signal: thus, a simple solenoidal coil has been used, together with a transparent glass cuvette and two LED's pointing towards one end of the coil. To ensure the maximum IR confinement, the end of the NMR probe has been wrapped with an aluminum tape. The magnetic fields in ^{1}H NMR measures have been 0.67, 1.11, 1.50 T corresponding to 28, 47, 64 MHz Larmor frequencies, while in ^{59}Co NMR measures 6.95 T corresponding to 70 MHz. The cooling procedure has been performed with different cooling rates (1 K/min and 6 K/min) and ^{1}H T_{1n} has been found to depend on it.

High pressure NMR experiments

The high pressure ^{1}H NMR experiments have been performed using an NMR pressure cell, with pressure range from 0 to 14 kbar, with 2 kbar steps. The sample has been placed into a teflon sampleholder and mixed with a fluorinated oil, to ensure homogeneous distribution of the external pressure and to suppress ^{1}H background signal as much as possible. A simple solenoidal coil, wrapped around the sample holder, has been used to detect the NMR signal. The magnetic field used has been 4.69 T corresponding to 200 MHz ^{1}H Larmor frequency.

A.1.2 Sequences and fits

The NMR experiments have allowed to measure the following physical quantities: the nuclear spin-lattice relaxation time T_{1n}, the NMR spectrum, the nuclear spin-spin relaxation time T_{2n}, the nuclear polarization time T_{POL} and the DNP signal enhancement ϵ and DNP enhanced polarization P_{DNP}.

T_{1n} measurements

To measure T_{1n} three different sequences have been employed to follow the recovery of the nuclear longitudinal magnetization M_n. All sequences have an initial train of RF saturation pulses which destroy M_n, a variable waiting time, to allow a partial recovery of M_n, and a reading sequence (free induction decay (FID), simple echo, solid echo). In the cases of ^{1}H and ^{13}C, which are both $S = \frac{1}{2}$ the recovery has been fit with a stretched exponential curve:

$$M_n(t) = M_0 \cdot (1 - \exp -(\frac{t}{T_{1n}})^{\beta_n}), \tag{A.1}$$

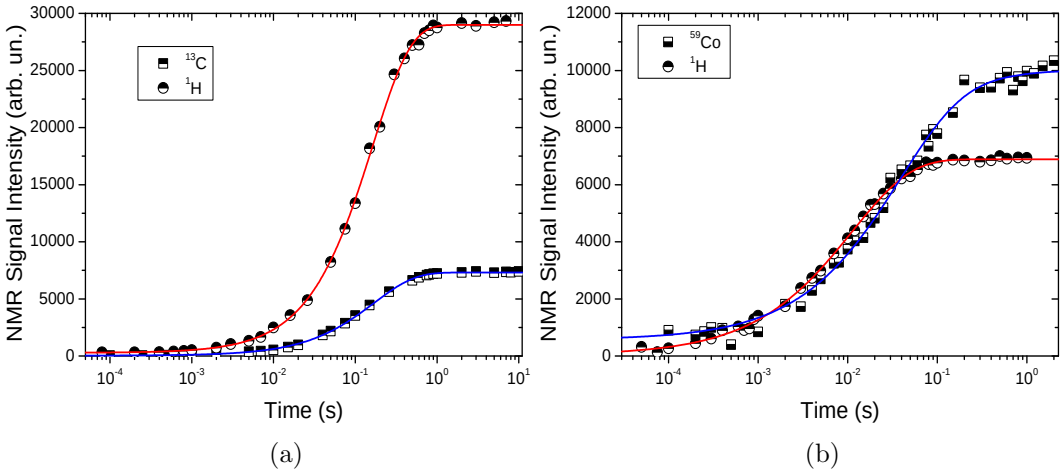

Figure A.1: a) Recovery of ^{1}H (black half up circles) and ^{13}C (black half up squares) magnetization in CD100 at 180 K in a 1.5 T and in CD9 at 80 K at 6.95 T, respectively. Lines are fit according to Eq. A.1. b) Recovery of ^{1}H (black half up circles) and ^{59}Co (black half down squares) magnetization at 100 K in 1.5 T and at 20 K in 6.95 T, respectively. Lines are fit according to Eq. A.1 and A.2, respectively.

where M_0 is the thermal nuclear magnetization and β_n a stretching coefficient accounting for a distribution of relaxation times. In the βCyclodextrins samples β_n ranges from 0.6 to 0.95, due to the amorphous structure of the compounds which make different nuclei probe slightly different microscopic environments. In the valence tautomer sample β_n ranges from 0.6 to 0.95, since ^{1}H occupies different sites in the organic ligands. In case of ^{59}Co the recovery has been fit with the recovery law for $S = \frac{7}{2}$ for magnetic relaxation:

$$M_n(t) = M_0 \cdot \left[1 - \left(\frac{75}{364}\exp(-\frac{15t}{T_{1n}}) + \right.\right.$$
$$\left.\left.\frac{1225}{1716}\exp(-\frac{28t}{T_{1n}}) + \frac{3}{44}\exp(-\frac{6t}{T_{1n}}) + \frac{1}{84}\exp(-\frac{t}{T_{1n}})\right)\right], \tag{A.2}$$

where RF irradiation has been performed on the central line of ^{59}Co, associated with the $m_I = +1/2 \leftrightarrow -1/2$ transition.

T_{2n} measurements

To measure T_{2n} a Hahn echo sequence ($\pi/2$ - τ - π) have been employed, with a variable echo time to follow the decay of the echo amplitude. This decay ha been fit either with a single exponential decay:

$$S(t) = S_0 \cdot \exp -\frac{t}{T_{2n}}, \tag{A.3}$$

where S_0 is the initial amplitude, or with a gaussian decay:

$$S(t) = S_0 \cdot \exp -\frac{t}{T_{2n}^2}. \tag{A.4}$$

The gaussian decay has been observed at low temperatures while the lorentzian decay at high temperatures.

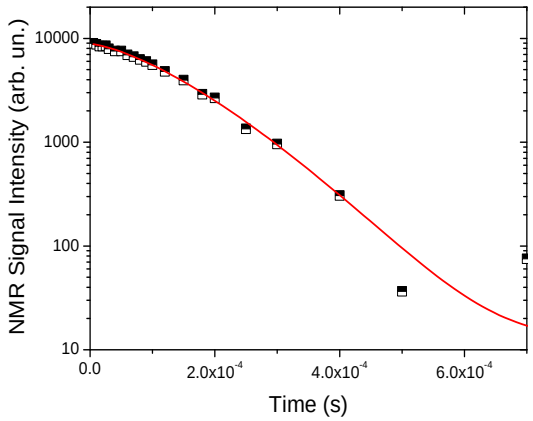

Figure A.2: ^{13}C NMR echo intensity decay over time in CD21d at 70 K in 3.45 T. Fit according to Eq. A.3.

NMR spectrum

In the cases of ^{1}H and ^{13}C, the NMR spectrum has been derived from by the Fourier transform of half of the echo or of the FID of the T_{1n}. Subsequently, the spectra have been fit with an appropriate function, a gaussian or a lorentzian, to evaluate the NMR linewidth, i.e. the full width at half maximum (FWHM). The gaussian shape is more appropriate at low temperatures where the motion is frozen and the spectrum is broadened by the nuclear magnetic dipolar interaction. The lorentzian shape is more likely to fit at higher temperatures, where the motional narrowing occurs. Regarding ^{59}Co, the huge quadrupolar moment of the nucleus makes the spectrum very broad. Thus, only small slices of the spectrum could be excited at one time and the ^{59}Co spectrum has been measured by scanning the simple echo amplitude over a range of nuclear Larmor frequencies. The central line reported Fig. A.4 is associated with the $m_I = +1/2 \leftrightarrow -1/2$ transition, while the broad left and right shoulders are

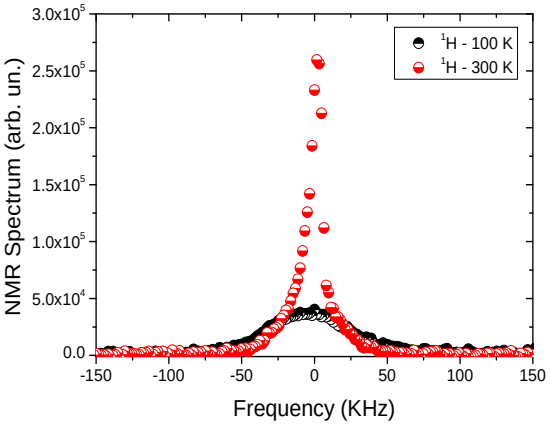

Figure A.3: ^{1}H NMR spectrum at 100 K (black half up circles) and 300 K (red half down circles) in CD100 in 1.50 T. Lines are fit according to a gaussian and a lorentzian curve, respectively.

associated with overlapping satellites transitions between the other Zeeman energy levels.

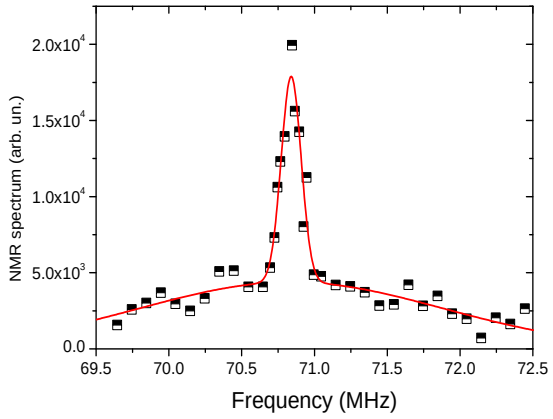

Figure A.4: ^{59}Co NMR spectrum at 5 K for a 6.95 T. The line is the fit of the sum of two gaussian curves.

DNP experiments

The DNP experiments have been performed in 3.41-3.45 T in the 1.60 - 4.20 K temperature range. The process of magnetization recovery has been observed, using the same T_{1n} sequence, in the absence and in the presence of MW irradiation. In the former case the recovery yields the ordinary T_{1n} and the thermal magnetization M_{0FF}, while in the latter the recovery has been fit with the following law:

$$M_n(t) = M_{0N} \cdot (1 - \exp -(\frac{t}{T_{POL}})^{\beta_n}), \tag{A.5}$$

yielding the nuclear polarization time T_{POL}, i.e. the time needed to build the hyperpolarizated out-of-equilibrium state, and M_{0N},+ the DNP enhanced magnetization. The DNP enhancement factor ϵ has been calculated using:

$$\epsilon = \frac{M_{0N} \cdot G_{OFF}}{M_{0FF} \cdot G_{ON}}, \tag{A.6}$$

where G_{OFF} and G_{ON} are the receiver gains in the absence and in the presence of MW irradiation, respectively.

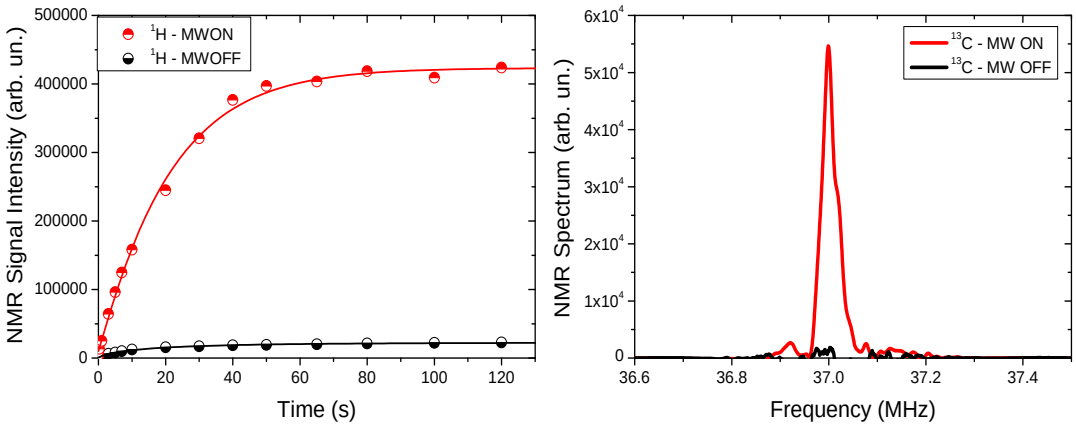

(a) (b)

Figure A.5: a) Recovery of ^{1}H magnetization in the presence (red half up circles) and in the absence (black half down circles) of MW irradiation in CD100 at 2.19 K in 3.45 T. Lines are fit according to Eq. A.1. b) ^{13}C NMR spectrum in the presence (red line) and in the absence (black line) of MW irradiation in CD21R at 1.60 K in 3.45 T.

The MW frequency has been swept in the range 96 - 98 GHz to find the optimal value prior to any DNP session. The final DNP enhanced polarization is then:

$$P_{DNP} = \epsilon \cdot \tanh \frac{\hbar \omega_I}{2K_B} T, \tag{A.7}$$

where the second factor in the right side is the thermal polarization and ω_I is the nuclear Larmor frequency.

A.2 SQUID Magnetometry

A.2.1 Instrumentation

The SQUID experiments have been performed in the SQUID laboratory of the Department of Physics at the University of Pavia (Pavia, Italy). An MPMS-XL7 SQUID magnetometer has been employed. All the measurement have been performed in a 0.1 T magnetic field. The irradiation of the sample has been achieved by placing an optical fiber, along the SQUID stick, externally

coupled with an IR laser diode (Thorlabs M940F1 Fiber-coupled LED: wavelength = 940 ± 15 nm, power = 6.5 mW). On the other side, the high pressure SQUID experiments have been performed using a CuBe pressure cell (Easy-Lab, Mcell 10), which allows to reach up to 20 kbar and which contains a Sn manometer to precisely measure the pressure achieved.

A.2.2 Sequences and fits

The magnetization temperature dependence has been measured upon cooling the sample from 300 K to 4 K, with a fixed cooling rate equal to 4 K/min, both at ambient and at high pressure. The light irradiation experiments have been performed in the range 4 - 55 K and the build-up of the magnetic susceptibility upon time has been fit with a stretched recovery law plus a constant term (χ_1) corresponding to the magnetic susceptibility value prior to irradiation:

$$\chi_M \cdot T(t) = \chi_0 \cdot T \cdot (1 - \exp -(\frac{t}{T_{irr}})^{\alpha_M}) + \chi_1 \cdot T, \tag{A.8}$$

where χ_0 is the value of the light-enhanced magnetic susceptibility, T_{irr} is the build-up time and α_M is the stretching exponent.

The magnetic susceptibility decay has been measured in the range 20 - 55 K after turning off light irradiation and it has been fit with a stretched decay law:

$$\chi_M \cdot T(t) = \chi_0 \cdot T \cdot \exp -(\frac{t}{T_{dec}})^{\alpha_d}, \tag{A.9}$$

where T_{dec} is the decay time and α_d is the stretching exponent.

A.3 Electron Paramagnetic Resonance

A.3.1 Instrumentation

The EPR experiments have been carried out at the Jožef Stefan Institute (Ljubljana, Slovenia). The following equipment has been used:

- an electromagnet, able to generate magnetic fields up to 2 T;
- an EPR spectrometer;
- a MW source and a cavity, which allow to generate and amplify MW in the X-band (9.7 GHz);
- an homemade software for sequence control and data analysis;
- a flux cryostat, for the temperature range 2 - 300 K, and an adiabatic helium pump in the range 2 - 4.2 K.

A.3.2 Sequences and fits

In the EPR experiments the following quantities have been measured: the electron spin-lattice relaxation time T_{1e}, the electron spin-spin relaxation time T_{2e} and the EPR spectrum, in pulse experiments, or its first derivative, in continuous wave (CW) experiments.

T_{1e} measurements

T_{1e} has been measured in pulsed experiments by means of an inversion simple echo recovery sequence and the recovery has been fit by the sum of a fast and a slow component:

$$M_e(t) = M_{0e} \cdot (1 - A_f \exp -(\frac{t}{T_{1ef}}) - A_s \exp -(\frac{t}{T_{1es}})), \tag{A.10}$$

where T_{1ef} and T_{1es} are the fast and slow electron spin-lattice relaxation times components, A_f and A_s are the related amplitudes and M_{0e} is the electron thermal magnetization.

T_{2e} measurements

T_{2e} has been measured in pulsed experiments by mean of an simple echo sequence and the decay has been fit by a stretched exponential law:

$$M_e(t) = M_{0e} \cdot (\exp -(\frac{t}{T_{2e}})^{\beta}_{e}), \tag{A.11}$$

where βe is the stretching exponent.

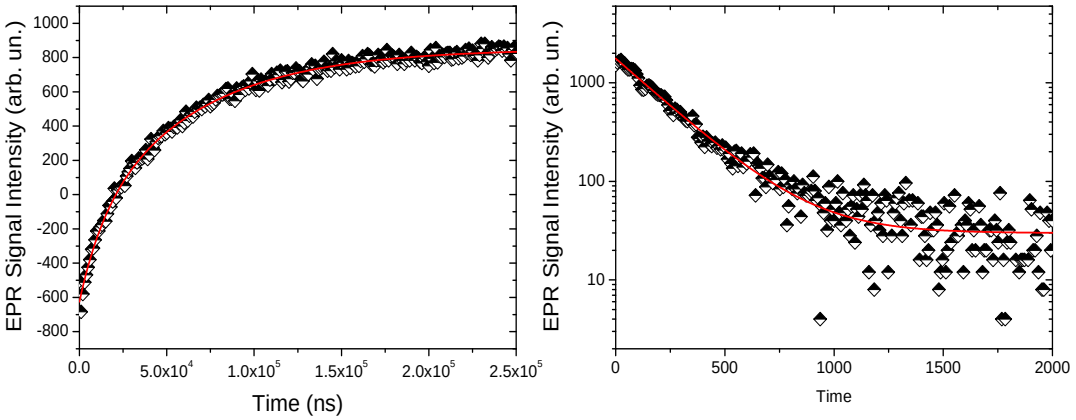

(a) (b)

Figure A.6: a) Recovery of electron magnetization in CD100 at 5 K in X-band. Fit according to Eq. A.10. b) Decay of electron spin echo intensity in CD100 at 5 K in X-band. Fit according to Eq. A.11.

The EPR spectrum

The EPR spectrum has been measured in two different ways, either as the FT of the longest time echo point of the T_{1e} sequence or using the CW techniques, this latter when the electronic relaxation times were too short to allow any pulse experiment.

A.4 Muon Spin Rotation

A.4.1 Instrumentation

The μSR experiments have been carried out at the ISIS facility (Oxford, UK) on the HIFI beam line. A flux cryostat has been used to explore the 5 -300 K temperature range. The powder has been pressed on a silver sample holder and covered with mylar foils to slow down muons and to allow them to stop inside the sample. The muon energy has been set to 29 MeV/c. The first round of experiments has been carried out in zero field (ZF) to check if muonium was present and the second round has been performed in longitudinal field (LF) to remove the nuclear dipolar contribution to muon relaxation. Irradiation of the sample was achieved by using four IR LED's (Thorlabs LED910E-AlGaAs: wavelength = 910 $\pm$ 10 nm, power = 12 mW, AC current = 16 mA) mounted on the four sides of the sample holder and with an irradiation angle close to 30°.

A.4.2 Sequences and fits

The measurements have been performed both in zero field and in a 200 Gauss longitudinal magnetic field. In the former case the muon's asymmetry has been fit, after background correction, with a simple exponential decay:

$$A(t) = A0 \cdot \exp -(\lambda_{ZF} t), \tag{A.12}$$

where λ_{ZF} is the ZF decay rate. In the latter case muon's asymmetry has been fit with a stretched exponential decay:

$$A(t) = A0 \cdot \exp -(\lambda_{LF} t)^{\beta_{LF}}, \tag{A.13}$$

where λ_{LF} is the LF relaxation rate and β_{LF} the stretching coefficient.

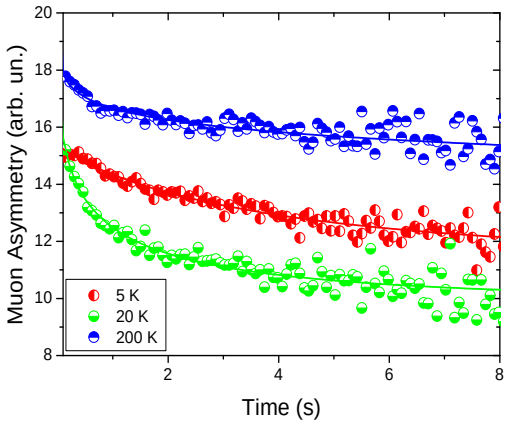

Figure A.7: Muon's asymmetry time dependence in 200 Gauss LF experiments: 200 K (blue half up circles), 20 K (green half down circles) and 5 K (red half left circles).

The initial amplitude in ZF condition was roughly equal to half of the amplitude in LF condition, probably due to a non negligible fraction of muonium in the sample. In both cases, an high background was observed, due to muons stopping in the silver sample holder.

Bibliography

[1] A. Tiwari, K.P. Iyer, V. Kumar, and H. Swart. *Advanced Magnetic and Optical Materials*. Scrivener Publishing LLC and John Wiley and Sons, Beverly, US, 2017.

[2] S. Zhang and D. Zhao. *Advances in Magnetic Materials Processing, Properties, and Performance*. CRC Press, Taylor and Francis Group, Boca Raton, US, 2017.

[3] N.A. Spaldin. *Magnetic Materials: Fundamentals and Applications*. Cambridge University Press, Cambridge, UK, 2 nd edition, 2011.

[4] S.H. Bossmann and H. Wang. *Magnetic Nanomaterials: Applications in Catalysis and Life Sciences*. The Royal Society of Chemistry, Croydon, UK, 2017.

[5] B. Sieklucka and D. Pinkowicz. *Molecular Magnetic Materials*. Wiley-VCH, Weinheim, Germany, 2017.

[6] A. Abragam. *The Principles of Nuclear Magnetism*. Oxford University Press, London, Great Britain, 1^{st} edition, 1961.

[7] C.P. Slichter. *Principles of Magnetic Resonance*. Springer Verlag, Berlin, Germany, 3^{rd} edition, 1990.

[8] H. Günther. *NMR Spectroscopy: Basic Principles, Concepts and Applications in Chemistry*. Wiley-VCH, Weinheim, Germany, 3 rd edition, 2013.

[9] U. Holzgrabe, I. Waver, and B. Diehl. *NMR Spectroscopy in Pharmaceutical Analysis*. Elvesier, Hungary, 2008.

[10] G. Nielsen, M. Stadler, H. Jonker, M. Betz, and H. Schwalbe. *NMR: Applications in Chemical Biology*. Wiley Online Library, 2008.

[11] E.M. Haacke, R.W. Brown, M.R. Thompson, and R. Venkatesan. *Magnetic Resonance Imaging Physical Principles and Sequence Design*. John Wiley and Sons, USA, 1999.

[12] W.E. Kenyon. *Petrophysical Principles of Applications of NMR Logging.* Society of Petrophysicists and Well-Log Analysts, 1997.

[13] M.F. Marcone, S. Wang, W. Albabish, S. Nie, D. Somnarain, and A. Hill. Diverse Food-based Applications of Nuclear Magnetic Resonance (NMR) Technology. *Food Res. Int.*, 51:729–747, 2013.

[14] A. Abragam and M. Goldman. *Nuclear Order and Disorder.* Clarendon Press, Oxford, Great Britain, 1^{st} edition, 1982.

[15] T Wenckebach. *Essentials of Dynamic Nuclear Polarization.* Spindrift Publications, Burgh-Haamstede, The Netherlands, 1^{st} edition, 2016.

[16] K. Golman, L.E. Olsson, O. Axelsson, S. Mansson, M. Karlsson, and J.S. Petersson. Molecular Imaging using Hyperpolarized ^{13}C. *Brit. J. Radiol.*, 76:S118–S127, 2003.

[17] A. Viale and S. Aime. Current Concepts on Hyperpolarized Molecules in MRI. *Curr. Opin. Chem. Biol.*, 14:90–96, 2010.

[18] U.L. Günther. Dynamic Nuclear Hyperpolarization in Liquids. *Top. Curr. Chem.*, 335:23–70, 2013.

[19] J.H. Lee, Y. Okuno, and S. Cavagnero. Sensitivity Enhancement in Solution NMR: Emerging Ideas and new Frontiers. *J. Magn. Reson.*, 241:18–31, 2014.

[20] P. Nikolaou, B.M. Goodson, and E.Y. Checkmenev. NMR Hyperpolarization Techniques for Biomedicine. *Chem. Eur. J.*, 21:3156–3166, 2015.

[21] A.H. Emwas, M. Saunders, C. Ludwig, and U.L. Günther. Determinants for Optimal Enhancement in Ex Situ DNP Experiments. *Appl. Magn. Reson.*, 34:483–494, 2008.

[22] K.N. Hu. Polarizing Agents and Mechanisms for High-Field Dynamic Nuclear Polarization of Frozen Dielectric Solids. *Solid State Nucl. Magn. Reson.*, 40:31–41, 2011.

[23] A.S.L. Thankamony, J.J. Wittmann, M. Kaushik, and B. Corzilius. Dynamic Nuclear Polarization for Sensitivity Enhancement in Modern Solid-State NMR. *Progr. Nucl. Magn. Reson. Spectrosc.*, 102-103:120–195, 2017.

[24] M. Kaushik, M. Qi, A. Godt, and B. Corzilius. Bis-Gadolinium Complexes for Solid Effect and Cross Effect Dynamic Nuclear Polarization. *Angew. Chem. Int. Ed.*, 56:4295–4299, 2017.

[25] T.R. Eichhorn, N. Takado, Y. Salameh, A. Capozzi, T. Cheng, J.N. Hyacinthe, M. Mishkovsky, C. Roussel, and A. Comment. Hyperpolarization without Persistent Radicals for in vivo Real-Time Metabolic Imaging. *Proc. Natl. Acad. Sci.*, 110:18064–18069, 2013.

[26] C.P. Slichter. The Discovery and Renaissance of Dynamic Nuclear Polarization. *Rep. Prog. Phys.*, 77:072501–072515, 2014.

[27] W. de Boer, M. Borghini, K. Morimoto, T.O. Niinikoski, and F. Udo. Dynamic Polarization of Protons, Deuterons, and Carbon-13 Nuclei: Thermal Contact Between Nuclear Spins and an Electron Spin-Spin Interaction Reservoir. *J. Low. Temp. Phys.*, 15:249–267, 1974.

[28] R.B. van Heeswijk, K. Uffmann, A. Comment, F. Kurdzesau, C. Perazzolo, C. Cudalbu, S. Jannin, J.A. Konter, P. Hautle, and B. et Al. van den Brandt. Hyperpolarized Lithium-6 as a Sensor of Nanomolar Contrast Agents. *Magn. Reson. Med.*, 61:1489–1493, 2009.

[29] J.H. Ardenkjaer-Larsen, B. Fridlund, A. Gram, G. Hansson, L. Hansson, M.H. Lerche, R. Servin, M. Thaning, and K. Golman. Increase in Signal-to-Noise Ratio of >10,000 Times in Liquid-State NMR. *Proc. Natl. Acad. Sci.*, 100:10158–10163, 2003.

[30] F. Blanc, L. Sperrin, D.A. Jefferson, S. Pawsey, M. Rosay, and C.P. Grey. Dynamic Nuclear Polarization Enhanced Natural Abundance ^{17}O Spectroscopy. *J. Am. Chem. Soc.*, 135:2975–2978, 2013.

[31] A. Peksoz. DNP Sensitivity of ^{19}F-NMR Signals in Hexafluorobenzene Ddepending on Polarizing Agent Type. *Magn. Reson. Chem.*, 54:748–752, 2016.

[32] R.K. Harris and G.J. Nesbitt. Cross Polarization for Quadrupolar Nuclei-Proton to Sodium-23. *J. Magn. Reson.*, 78:245–256, 1988.

[33] B. Derighetti, S. Hafner, H. Marxer, and H. Rager. NMR of ^{29}Si and ^{25}Mg In Mg_2SiO_4 with Dynamic Polarization Technique. *Phys. Lett. A*, 66:150–152, 1978.

[34] A.J. Rossini, A. Zagdoun, M. Lelli, A. Lesage, C. Copéret, and L. Emsley. Dynamic Nuclear Polarization Surface Enhanced NMR Spectroscopy. *Acc. Chem. Res.*, 46:1942–1951, 2013.

[35] U. Akbey, B. Altin, A. Linden, S. Özçelik, M. Gradzieski, and H. Oschkinat. Dynamic Nuclear Polarization of Spherical Nanoparticles. *Phys. Chem. Chem. Phys.*, 15:20706–20716, 2013.

[36] K. Suzuki, S. Kubo, F. Aussenac, F. Engelke, T. Fukushima, and H. Kaji. Analysis of Molecular Orientation in Organic Semiconducting Thin Films

Using Static Dynamic Nuclear Polarization Enhanced Solid-State NMR Spectroscopy. *Angew. Chem. Int. Ed.*, 56:14842–14846, 2017.

[37] D.A. Hirsh, A.J. Rossini, L. Emsley, and R.W. Schurko. ^{35}Cl Dynamic Nuclear Polarization Solid-state NMR of Active Pharmaceutical Ingredients. *Phys. Chem. Chem. Phys.*, 18:25893–25904, 2016.

[38] D. Lee, C. Leroy, C. Crevant, L. Bonhomme-Coury, F. Babonneau, D. Laurencin, C. Bonhomme, and G. De Paëper. Interfacial $Ca2^{+}$ Environments in Nanocrystalline Apatites Revealed by Dynamic Nuclear Polarization Enhanced ^{43}Ca NMR Spectroscopy. *Nat. Commun.*, 8:14104–14110, 2017.

[39] B. Corzilius, V.K. Michaelis, S.A. Penzel, E. Ravera, A.A. Smith, C. Luchinat, and R.G. Griffin. Dynamic Nuclear Polarization of ^{1}H, ^{13}C, and ^{59}Co in a Tris(ethylenediamine)cobalt(III) Crystalline Lattice Doped with Cr(III). *J. Am. Chem. Soc.*, 136:11716–11727, 2014.

[40] S.B. Orlinskii, J. Schmidt, P. Baranov, C.D. Donegá, and A. Meijerink. Dynamic Nuclear Polarization of ^{67}Zn and ^{1}H Spins by means of Shallow Donors in ZnO Nanoparticles. *Phys. Rev. B*, 79:165316, 2009.

[41] L. Piveteau, T. Ong, A.J. Rossini, L. Emsley, C. Copéret, and V.K. Maksym. Structure of Colloidal Quantum Dots from Dynamic Nuclear Polarization Surface Enhanced NMR Spectroscopy. *J. Am. Chem. Soc.*, 137:13964–13971, 2015.

[42] L. Lumata, A.K. Jindal, M.E. Merritt, C.R. Malloy, A.D. Sherry, and Z. Kovacs. DNP by Thermal Mixing under Optimized Conditions Yields $>$ 60000-fold Enhancement of ^{89}Y NMR Signal. *J. Am. Chem. Soc.*, 133:8673–8680, 2011.

[43] L. Lumata, M.E. Merritt, Z. Hashami, S.J. Ratnakar, and Z. Kovacs. Production and NMR Characterization of Hyperpolarized ^{107,109}Ag Complexes. *Angew. Chem. Int. Ed.*, 51:280–280, 2012.

[44] B. Gotschy, G. Denninger, H. Obloh, W. Wilkening, and J. Schneider. Overhauser Shift and Dynamic Nuclear Polarization in InP. *Solid State Comm.*, 71:629–632, 1989.

[45] W.R. Gunther, V.K. Michaelis, M.A. Caporini, R.G. Griffin, and Y. Róman-Leshkov. Dynamic Nuclear Polarization NMR Enables the Analysis of Sn-Beta Zeolite Prepared with Natural Abundance ^{119}Sn Precursors. *J. Am. Chem. Soc.*, 136:6219–6222, 2014.

[46] G. Denninger and H. Pascher. Dynamic nuclear spin polarization by coherent spin flip Raman scattering in InSb. *Solid State Comm.*, 70:399–402, 1989.

[47] A. Comment, S. Jannin, J.N. Hyacinthe, P. Miéville, R. Sarkar, P. Ahuja, P.R. Vasos, X. Montet, F. Lazeyras, and J.P. et Al. Vallée. Hyperpolarizing Gases via Dynamic Nuclear Polarization and Sublimation. *Phys. Rev. Lett.*, 105:018804–1–4, 2010.

[48] M. Karlsson, J.H. Ardenkjaer-Larsen, and M.H. Lerche. Hyperpolarized ^{133}Cs is a Sensitive Probe for Real-time monitoring of Biophysical Environments. *Chem. Commun.*, 53:6625–6628, 2017.

[49] D.G. Crabb and W. Meyer. Solid Polarized Targets fot Nuclear and Particle Physics Experiments. *Annu. Rev. Nucl. Part. Sci.*, 109:47–67, 1997.

[50] P.J. Cassidy and G.K. Radda. Molecular Imaging Perspectives. *J. R. Soc. Interface*, 2:133–144, 2005.

[51] M.L. James and S.S. Gambhir. A Molecular Imaging Primer: Modalities, Imaging Agents and Applications. *Physiol. Rev.*, 92:897–965, 2012.

[52] S. Kunjachan, J. Ehling, G. Storm, F. Kiessling, and T. Lammers. Noninvasive Imaging of Nanomedicines and Nanotheranostics: Principles, Progress, and Prospects. *Chem. Rev.*, 115:10907–10937, 2015.

[53] Z. Chen, P. Zhao, Z. Luo, M. Zheng, H. Tian, P. Gong, G. Gao, H. Pan, L. Liu, and A. et Al. Ma. Cancer Cell Membrane-Biomimetic Nanoparticles for Homologous-Targeting Dual-Modal Imaging and Photothermal Therapy. *ACS Nano*, 10:10049–10057, 2016.

[54] A. Comment, B. van den Brandt, K. Uffmann, F. Kurdzesau, S. Jannin, J.A. Konter, P. Hautle, W.T. Wenckebach, R. Gruetter, and J.J. van den Klink. Design and Performance of a DNP Prepolarizer Coupled to a Rodent MRI Scanner. *Concepts Magn. Reson. B*, 31:255–269, 2007.

[55] J. Milani, B. Vuichoud, A. Bornet, P. Miéville, R. Mottier, S. Jannin, and G. Bodenhausen. A Magnetic Tunnel to Shelter Hyperpolarized Fluids. *Rev. Sci. Instrum.*, 86:024101–1–9, 2015.

[56] A. Flori, M. Liserani, S. Bowen, J.H. Ardenkjaer-Larsen, and L. Menichetti. Dissolution Dynamic Nuclear Polarization of Non-Self-Glassing Agents: Spectroscopy and Relaxation of Hyperpolarized [1-^{13}C]Acetate. *J. Phys. Chem. A*, 119:1885–1893, 2015.

[57] R.M. Malinowski, K.W. Lipsø, M.H. Lerche, and J.H. Ardenkjaer-Larsen. Dissolution Dynamic Nuclear Polarization Capability Study with Fluid Path. *J. Magn. Reson.*, 272:141–146, 2016.

[58] A. Bornet and S. Jannin. Optimizing Dissolution Dynamic Nuclear Polarization. *J. Magn. Reson.*, 264:13–21, 2016.

[59] J.H. Ardenkjaer-Larsen. On the Present and Future of Dissolution-DNP. *J. Magn. Reson.*, 264:3–12, 2016.

[60] A. Comment. Dissolution DNP for in vivo Preclinical Studies. *J. Magn. Reson.*, 264:39–48, 2016.

[61] X. Ji, A. Bornet, B. Vuichoud, J. Milani, D. Gajan, A.J. Rossini, L. Emsley, G. Bodenhausen, and S. Jannin. Transportable Hyperpolarized Metabolites. *Nat. Commun.*, 8:13975–13980, 2017.

[62] K.R. Keshari and D.M. Wilson. Chemistry and Biochemistry of ^{13}C Hyperpolarized Magnetic Resonance using Dynamic Nuclear Polarization. *Chem. Soc. Rev.*, 14:1627–1659, 2014.

[63] S. Mansson, E. Johansson, P. Magnusson, C.M. Chai, G. Hansson, J.S. Petersson, F. Stahlberg, and K. Golman. ^{13}C Imaging - a New Diagnostic Platform. *Eur. Radiol.*, 16:57–67, 2006.

[64] E. Milshteyn, C. von Morze, G.D. Reed, H. Shang, P.J. Shin, Z. Zhu, H.Y. Chen, R. Bok, A. Goga, and J. et Al. Kurhanewicz. Development of High Resolution 3D Hyperpolarized Carbon-13 MR Molecular Imaging Techniques. *Magn. Reson., Imaging*, 38:152–162, 2017.

[65] K. Golman, R. in 't Zandt, and M. Thaning. Real-Time Metabolic Imaging. *Proc. Natl. Acad. Sci. U.S.A.*, 103:11270–11275, 2006.

[66] K. Golman, R. in't Zandt, M. Lerche, R. Pehrson, and J.H. Ardenkjaer-Larsen. Metabolic Imaging by Hyperpolarized ^{13}C Magnetic Resonance Imaging for In vivo Tumor Diagnosis. *Cancer. Res.*, 66:10855–10860, 2006.

[67] M.J. Albers, R. Bok, A.P. Chen, C.H. Cunningham, M.L. Zierhut, V.Y. Zhang, S.J. Kohler, J. Tropp, R.E. Hurd, and Y.F. et Al. Yen. Hyperpolarized 13 C Lactate, Pyruvate, and Alanine: Noninvasive Biomarkers for Prostate Cancer Detection and Grading. *Cancer Res.*, 68:8607–8615, 2008.

[68] F.A. Gallagher, M.I. Kettunen, S.E. Day, M. Lerche, and K.M. Brindle. ^{13}C MR Spectroscopy Measurements of Glutaminase Activity in Human Hepatocellular Carcinoma Cells Using Hyperpolarized ^{13}C-Labeled Glutamine. *Magn. Reson. Med.*, 60:253–257, 2008.

[69] F.A. Gallagher, M.I. Kettunen, D.E. Hu, P.R. Jensen, R. in't Zandt, M. Karlsson, A. Gisselson, S.K. Nelson, T.H. Witney, and S.E. Bohndiek. Production of Hyperpolarized [1,4- $^{13}C_2$]Malate from [1,4-$^{13}C_2$]Fumarate is a Marker of Cell Necrosis and Treatment response in tumors. *Proc. Natl. Acad. Sci. U.S.A.*, 106:19801–19806, 2009.

[70] K.R. Keshari, D.M. Wilson, A.P. Chen, R. Bok, P.E.Z. Larson, S. Hu, M. Van Criekinge, J.M. Macdonald, D.B. Vigneron, and J. Kurhanewicz. Hyperpolarized [2^{13}C]-Fructose: A Hemiketal DNP Substrate for In Vivo Metabolic Imaging. *J. Am. Chem. Soc.*, 131:17591–17596, 2009.

[71] K.M. Brindle, S.E. Bohndiek, F.A. Gallagher, and M.I. Kettunen. Tumor Imaging Using Hyperpolarized ^{13}C Magnetic Resonance Spectroscopy. *Magn. Reson. Med.*, 66:505–519, 2011.

[72] J. Kurzhanewicz, D.B. Vigneron, K. Brindle, E.Y. Chekmenev, A. Comment, C.H. Cunningham, R.J. DeBerardinis, G.G. Green, O.M. Leach, and S.S. et Al. Rajan. Analysis of Cancer Metabolism by Imaging Hyperpolarized Nuclei: Prospects for Translation to Clinical Research. *Neoplasia*, 13:81–97, 2011.

[73] R.E. Hurd, Y.F. Yen, A. Chen, and J.H. Ardenkjaer-Larsen. Hyperpolarized ^{13}C Metabolic Imaging Using Dissolution Dynamic Nuclear Polarization. *J. Magn. Reson. Imaging*, 36:1314–1328, 2012.

[74] S.J. Nelson, J. Kurhanewicz, D.B. Vigneron, P.E.Z. Larson, A.L. Harzstark, M. Ferrone, M. van Criekinge, J.W. Chang, R. Bok, and I. et Al. Park. Metabolic Imaging of Patients with Prostate Cancer Using Hyperpolarized [1- ^{13}C] Pyruvate. *Sci. Transl. Med.*, 5:1–12, 2103.

[75] K. Kumagai, M. Akakabe, M. Tsuda, M. Tsuda, E. Fukushi, J. Kawabata, T. Abe, and K. Ichikawa. Observation of Glycolytic Metabolites in Tumor Cell Lysate by Using Hyperpolarization of Deuterated Glucose. *Biol. Pharm. Bull.*, 37:1416–1421, 2014.

[76] A. Comment and M.E. Merritt. Hyperpolarized Magnetic Resonance as a Sensitive Detector of Metabolic Function. *Biochem.*, 53:7333–7357, 2014.

[77] T.B. Rodrigues, E.M. Serrao, B.W.C. Kennedy, D.E. Hu, M.I. Kettunen, and K.M. Brindle. Magnetic Resonance Imaging of Tumor Glycolysis using Hyperpolarized ^{13}C-Labeled Glucose. *Nat. Med.*, 20:93–98, 2014.

[78] K.M. Brindle. Imaging Metabolism with Hyperpolarized ^{13}C-Labeled Cell Substrates. *J. Am. Chem. Soc.*, 137:6418–6427, 2015.

[79] L.S. Cardona and K.R. Keshari. ^{13}C-Labeled Biochemical Probes for the Study of Cancer Metabolism with Dynamic Nuclear Polarization-Enhanced Magnetic Resonance Imaging. *Cancer Metab.*, 3:1–11, 2015.

[80] M. Mishkovsky and A. Comment. Hyperpolarized MRS: New Tool to Study Real-Time Brain Function and Metabolism. *Anal. Biochem.*, 529:270–277, 2017.

[81] A.M. Serrao and K.M. Brindle. Dynamic Nuclear Polarisation: The Future of Imaging in Oncology? *Porto Biomed.*, 2:71–75, 2017.

[82] M. Schroeder and C. Lautsen. Imaging Oxygen Metabolism with Hyperpolarized Magnetic Resonance: a Novel Approach for the Examination of Cardiac and Renal Function. *Biosci. Rep.*, 37:1–18, 2017.

[83] K. Golman, J.H. Ardenkjaer-Larsen, J.S. Petersson, S. Mansson, and I. Leunbach. Molecular Imaging with Endogenous Substances. *Proc. Natl. Acad. Sci. U.S.A.*, 100:10435–10439, 2003.

[84] D.J. Tyler. Cardiovascular Applications of Hyperpolarized MRI. *Curr. Cardiovasc. Imaging Rep.*, 4:108–115, 2011.

[85] M.E. Merritt, C. Harrison, A.D. Sherry, C.R. Malloy, and S.C. Burgess. Flux through Hepatic Pyruvate Carboxylase and Phosphoenolpyruvate Carboxykinase Detected by Hyperpolarized ^{13}C Magnetic Resonance. *Proc. Natl. Acad. Sci. U.S.A.*, 108:19084–19089, 2011.

[86] T. Kawano, M. Murata, F. Hyodo, H. Eto, N. Kosem, R. Nakata, N. Hamano, J.S. Piao, S. Narahara, and T. et Al. Akahoshi. Noninvasive Mapping of the Redox Status of Dimethylnitrosamine - Induced Hepatic Fibrosis using in vivo Dynamic Nuclear Polarization - Magnetic Resonance Imaging. *Sci. Rep.*, 6:32604–32612, 2016.

[87] D.A. Hall, D.C. Maus, G.J. Gerfen, S.J. Inati, L.R. Becerra, F.W. Dahlquist, and R.G. Griffin. Polarization-Enhanced NMR Spectroscopy of Biomolecules in Frozen Solution. *Science*, 276:930–931, 1997.

[88] T. Maly, L.B. Andreas, A.A. Smith, and R.G. Griffin. ^{2}H-DNP-enhanced ^{2}H-^{13}C Solid-State NMR Correlation Spectroscopy. *Phys. Chem. Chem. Phys.*, 12:5872–5878, 2010.

[89] U. Akbey, W.T. Franks, A. Linden, S. Lange, R.G. Griffin, B.J. van Rossum, and H. Oschkinat. Dynamic Nuclear Polarization of Deuterated Proteins. *Angew. Chem. Int. Ed.*, 49:7803–7806, 2010.

[90] T. Viennet, A. Viegas, A. Kuepper, S. Arens, V. Gelev, O. Petrov, T.N. Grossmann, H. Heise, and M. Etzkorn. Selective Protein Hyperpolarization in Cell Lysates Using Targeted Dynamic Nuclear Polarization. *Angew. Chem. Int. Ed.*, 55:10746–10750, 2016.

[91] D. Stöppler, C. Song, B.J. van Rossum, M.A. Geiger, C. Lang, M.A. Mroginski, A.P. Jagtap, S.T. Sigurdsson, J. Matysik, and J. et Al. Hughes. Dynamic Nuclear Polarization Provides New Insights into Chromophore Structure in Phytochrome Photoreceptors. *Angew. Chem. Int. Ed.*, 55:16017–16020, 2016.

[92] R. Rogawski and A.E. McDermott. New NMR Tools for Protein Structure and Function: Spin Tags for Dynamic Nuclear Polarization Solid State NMR. *Arch. Biochem. Biophys.*, 628:102–113, 2017.

[93] B. Vuichoud, E. Canet, J. Milani, A. Bornet, D. Baudouin, L. Veyre, D. Gajan, L. Emsley, A. Lesage, and C. Copéret. Hyperpolarization of Frozen Hydrocarbon Gases by Dynamic Nuclear Polarization at 1.2 K. *J. Phys. Chem. Lett.*, 7:3235–3239, 2016.

[94] D.A. Barskiy, A.M. Coffey, P. Nikolaou, D.M. Mikhaylov, B.M. Goodson, R.T. Branca, G.J. Lu, M.G. Shapiro, V. Telkki, and V.V. Zhivonitko. NMR Hyperpolarization Techniques of Gases. *Chem. Eur. J.*, 23:725–751, 2017.

[95] A.S.L. Thankamony, O. Lafon, X. Lu, F. Aussenca, M. Rosay, J. Trébosc, H. Vezin, and J.P. Amoureux. Solvent-Free High-Field Dynamic Nuclear Polarization of Mesoporous Silica Functionalized with TEMPO. *Appl. Magn. Reson.*, 43:237–250, 2012.

[96] D. Gajan, M. Schwarzwälder, M.P. Conley, W.R. Grüning, A.J. Rossini, A. Zagdoun, M. Lelli, M. Yulikov, G. Jeschke, and C. Sauveé. Solid-Phase Polarization Matrixes for Dynamic Nuclear Polarization from Homogeneously Distributed Radicals in Mesostructured Hybrid Silica Materials. *J. Am. Chem. Soc.*, 135:15459–15466, 2013.

[97] O. Ouari, T. Phan, G. Ziarelli, F. Casano, F. Aussenac, P. Thureau, D. Gigmes, P. Tordo, and S. Viel. Improved Structural Elucidation of Synthetic Polymers by Dynamic Nuclear Polarization Solid-State NMR Spectroscopy. *ACS Macro Lett.*, 2:715–719, 2013.

[98] D. Le, G. Casano, T.N.T. Phan, F. Ziarelli, O. Ouari, F. Aussenac, P. Thureau, G. Mollica, D. Gigmes, and P. et Al. Tordo. Optimizing Sample Preparation Methods for Dynamic Nuclear Polarization Solid-state NMR of Synthetic Polymers. *Macromol.*, 47:3909.3916, 2014.

[99] P. Serna and C. Corma. Transforming Nano Metal Nonselective Particulates into Chemoselective Catalysts for Hydrogenation of Substituted Nitrobenzenes. *ACS Catal.*, 5:7114–7121, 2015.

[100] D. Lee, S. Hediger, and G. De Paëpe. Is Solid-State NMR Enhanced by Dynamic Nuclear Polarization? *Solid State Nucl. Magn. Reson.*, 66:6–20, 2015.

[101] S. Kaźmierski, T. Pawlak, A. Jeziorna, and M.J. Potrzebowski. Modern Solid State NMR Techniques and Concepts in Structural Studies of Synthetic Polymers. *Polym. Adv. Technol.*, 27:1143–1155, 2016.

[102] W.R. Grüniger, H. Bieringer, M. Schwarzwälder, D. Gajan, A. Bornet, B. Vuichoud, J. Milani, D. Baudouin, L. Veyre, and A. et Al. Lesage. Phenylazide Hybrid-Silica - Polarization Platform for Dynamic Nuclear Polarization at Cryogenic Temperatures. *Helv. Chim. Acta*, 100:e1600122–1–9, 2017.

[103] M.A. Sani, P.A. Martin, R. Yunis, F. Chen, M. Forsyth, M. Deschamps, and L.A. O'Dell. Probing Ionic Liquid Electrolyte Structure via the Glassy State by Dynamic Nuclear Polarization NMR Spectroscopy. *J. Phys. Chem. Lett.*, 9:1007–1011, 2018.

[104] J.W. Aptekar, M.C. Cassidy, A.C. Johnson, R.A. Barton, M. Lee, A.C. Ogier, C. Vo, M.N. Anahtar, Y. Ren, and S.N. Bahtia. Silicon Nanoparticles as Hyperpolarized Magnetic Resonance Imaging Agents. *ACS Nano*, 3:4003–4008, 2009.

[105] M.H. Lerche, S. Meier, P.R. Jensen, S.O. Hustvedt, M. Karlsson, J. Duus, and J.H. Ardenkjaer-Larsen. Quantitative Dynamic Nuclear Polarization-NMR on Blood Plasma for Assays of Drug Metabolism. *NMR Biomed.*, 24:96–103, 2011.

[106] T.M. Atkins, M.C. Cassidy, M. Lee, S. Ganguly, C.M. Marcus, and S.M. Kauzlarich. Synthesis of Long T_1 Silicon Nanoparticles for Hyperpolarized ^{29}Si Magnetic Resonance Imaging. *ACS Nano*, 7:1609–1617, 2013.

[107] D.E. Korenchan, R.R. Flavell, C. Baligand, R. Siriam, K. Neumann, S. Sukumar, H. Van Brocklin, D.B. Vigneron, D.M. Wilson, and J. Kurhanewicz. Dynamic Nuclear Polarization of Biocompatible ^{13}C-Enriched Carbonates for in vivo pH Imaging. *Chem. Commun.*, 52:3030–3033, 2016.

[108] H. Eto, G. Tsuji, T. Chiba, M. Furue, and F. Hyodo. Non-Invasive Evaluation of Atopic Dermatitis Based on Redox Status Using in vivo Dynamic Nuclear Polarization Magnetic Resonance Imaging. *Free Radical Biol. Med.*, 103:209–215, 2017.

[109] B. van den Brandt, E.I. Bunyatova, P. Hautle, and J.A. Konter. DNP with the Free Radicals Deuterated TEMPO and Deuterated Oxo-TEMPO. *Nucl. Instrum. Methods Phys. Res., Sect. A*, 526:53–55, 2004.

[110] F. Kurdzesau, B. van der Brandt, A. Comment, P. Hautle, S. Jannin, J.J. van der Klink, and J.A. Konter. Dynamic Nuclear Polarization of Small Labelled Molecules in Frozen Water-Alcohol Solutions. *J. Phys. D: Appl. Phys.*, 41:155506–1–10, 2008.

[111] J.H. Ardenkjaer-Larsen, S. Macholl, and H. Jóhannesson. Dynamic Nuclear Polarization with Trityls at 1.2 K. *Appl. Magn. Reson.*, 34:509–522, 2008.

[112] P. Höfer, P. Carl, G. Guthausen, T. Prisner, M. Reese, T. Carlomagno, C. Griesinger, and M. Bennati. Studies of Dynamic Nuclear Polarization with Nitroxides in Aqueous Solution. *Appl. Magn. Reson.*, 34:393–398, 2008.

[113] H. Jóhannesson, S. Macholl, and J.H. Ardenkjaer-Larsen. Dynamic Nuclear Polarization of [1-^{13}C]Pyruvic Acid at 4.6 Tesla. *Appl. Magn. Reson.*, 197:167–175, 2009.

[114] S. Macholl, H. Jóhannesson, and J.H. Ardenkjaer-Larsen. Trityl Biradicals and ^{13}C Dynamic Nuclear Polarization. *Phys. Chem. Chem. Phys.*, 12:5804–5817, 2010.

[115] W. Meyer, J. Heckmann, C. Hess, E. Radtke, G. Reichenz, L. Triebwasser, and L. Wang. Dynamic Polarization of ^{13}C Nuclei in Solid ^{13}C Labeled Pyruvic Acid. *Nucl. Instrum. Methods Phys. Res., Sect. A*, 631:1–5, 2011.

[116] A. Bornet, R. Melzi, S. Jannin, and G. Bodenhausen. Cross Polarization for Dissolution Dynamic Nuclear Polarization Experiments at Readily Accessible Temperatures $1.2 < T < 4.2$ K. *Appl. Magn. Reson.*, 43:107–117, 2012.

[117] T.C. Ong, M.L. Mak-Jurkauskas, J.J. Walish, V.K. Michaelis, B. Corzilius, A.A. Smith, A.M. Clausen, J.C. Cheetham, T.M. Swager, and R.G. Griffin. Solvent-Free Dynamic Nuclear Polarization of Amorphous and Crystalline ortho-Terphenyl. *J. Phys. Chem. B*, 117:3040–3046, 2013.

[118] E. Ravera, B. Corzilius, V.K. Michaelis, C. Rosa, R.G. Griffin, C. Luchinat, and I. Bertini. Dynamic Nuclear Polarization of Sedimented Solutes. *J. Am. Chem. Soc.*, 135:1641–1644, 2013.

[119] A. Bornet, R. Melzi, A.J.P. Linde, P. Hautle, B. van den Brandt, S. Jannin, and G. Bodenhausen. Boosting Dissolution Dynamic Nuclear Polarization by Cross Polarization. *J. Phys. Chem. Lett.*, 4:111–114, 2013.

[120] M. Filibian, S.C. Serra, M. Moscardini, A. Rosso, F. Tedoldi, and P. Carretta. The Role of the Glassy Dynamics and Thermal Mixing in the Dynamic Nuclear Polarization and Relaxation Mechanisms of Pyruvic Acid. *Phys. Chem. Chem. Phys.*, 16:27025–27036, 2014.

[121] E. Elisei, M. Filibian, P. Carretta, S.C. Serra, F. Tedoldi, J.F. Willart, M. Descamps, and A. Cesáro. Dynamic Nuclear Polarization of a Glassy Matrix Prepared by Solid State Mechanochemical Amorphization of Crystalline Substances. *Chem. Commun.*, 51:2080–2083, 2015.

[122] F. Filibian, E. Elisei, S.C. Serra, A. Rosso, F. Tedoldi, A. Cesáro, and P. Carretta. Nuclear Magnetic Resonance Studies of DNP-Ready Trehalose Obtained by Solid State Mechanochemical Amorphization. *Phys. Chem. Chem. Phys.*, 18:16912–16920, 2016.

[123] E. Boisselier and D. Astruc. Gold Nanoparticles in Nanomedicine: Preparations, Imaging, Diagnostics, Therapies and Toxicity. *Chem. Soc. Rev.*, 38:1759–1782, 2009.

[124] D. Bobo, K.J. Robinson, J. Islam, K.J. Thurecht, and S.R. Corrie. Nanoparticles-Based Medicines: a Review of FDA-Approved Materials and Clinical Trials to Date. *Pharm. Res.*, 33:2373–2387, 2016.

[125] J. Szejtli. Introduction and General Overview of Cyclodextrin Chemistry. *Chem. Rev.*, 98:1743–1753, 1998.

[126] E.M.M. Del Valle. Cyclodextrins and Their Uses: a Review. *Process Biochem.*, 39:1033–1046, 2004.

[127] S. V. Kurkov and T. Loftsson. Cyclodextrins. *Int. J. Pharm.*, 453:167–180, 2013.

[128] H. Dodziuk. *Cyclodextrins and Their Complexes*. WILEY-VCH, Weinheim, Germany, 1^{st} edition, 2006.

[129] R. Singh, N. Bharti, J. Madan, and S.N. Hiremath. Characterization of Cyclodextrin Inclusion Complexes - A Review. *J. Pharm. Sci. Technol.*, 2:171–183, 2010.

[130] T. Loftsson and D. Duchêne. Cyclodextrins and their Pharmaceutical Applications. *Int. J. Pharm.*, 329:1–11, 2007.

[131] A. Rasheed, A.C.K. Kumar, and V.V.N.S.S. Sravanthi. Cyclodextrins as Drug Carrier Molecule: A Review. *Sci. Pharm.*, 76:567–598, 2008.

[132] W.F. Lai. Cyclodextrins in Non-Viral Gene Delivery. *Biomat.*, 35:401–411, 2014.

[133] Z. Kotková, J. Kotek, D. Jirák, P. Jendelová, V. Herynek, Z. Berková, P. Hermann, and I. Lukeš. Cyclodextrin-Based Bimodal Fluorescence/MRI Contrast Agents: an Efficient Approach to Cellular Imaging. *Chem. Eur. J.*, 16:10094–10102, 2010.

[134] F. Caglieris, L. Melone, F. Canepa, G. Lamura, F. Castiglione, M. Ferro, L. Malpezzi, A. Mele, C. Punta, and P. et Al. Franchi. Effective Magnetic Moment in Cyclodextrin-Polynitroxides: Potential Supramolecular Vectors for Magnetic Resonance Imaging. *RCS Adv.*, 5:76133–76140, 2015.

[135] Z. Zhou, Z. Han, and Z.R. Lu. A Targeted Nanoglobular Contrast Agent from Host-Guest Self-assembly for MR Cancer Molecular Imaging. *Biomat.*, 85:168–179, 2016.

[136] R.L. White. The Physical Boundaries to High-Density Magnetic Recording. *J. Magn. Magn. Mater.*, 209:1–5, 2000.

[137] H.J. Richter. Density Limits Imposed by the Microstructure of Magnetic Recording Media. *J. Magn. Magn. Mater.*, 321:467–476, 2009.

[138] A. Moser, K. Takano, D.T. Margulies, M. Albrecht, Y. Sonobe, Y. Ikeda, S. Sun, and E.E. Fullerton. Magnetic Recording: Advancing into the Future. *J. Phys. D: Appl. Phys.*, 35:R157–R167, 2002.

[139] R.F.L. Evans, R.W. Chantrell, U. Nowak, A. Lyberatos, and H.J. Richter. Thermally Induced Error: Density Limit for Magnetic Data Storage. *Appl. Phys. Lett.*, 100:102402,1–3, 2012.

[140] A.D. Kent and D.C. Worledge. A New Spin on Magnetic Memories. *Nat. Nanotechnol.*, 10:187–191, 2015.

[141] A.S. Dvornikov, E.P. Walker, and P.M. Rentzepis. Two Photon Three - Dimensional Optical Storage Memory. *J. Phys. Chem. A*, 113:13633–13644, 2009.

[142] U. Pischel. Digital Operations with Molecules - Advances, Challenges and Perspectives. *Aust. J. Chem.*, 63:148–164, 2010.

[143] J. Andreásson and U. Pischel. Molecules with a Sense of Logic: a Progress Report. *Chem. Soc. Rev.*, 44:1053–1059, 2015.

[144] N. Weibel, S. Grunder, and M. Mayor. Functional Molecules in Electronic Circuits. *Org. Biomol. Chem.*, 5:2343–2353, 2007.

[145] L. Bogani and W. Wernsdorfer. Molecular Spintronics using Single-molecule Magnets. *Nat. Mat,*, 7:179–186, 2008.

[146] M. Mannini, F. Pineider, P. Sainctavit, C. Danieli, E. Otero, C. Sciancalepore, A.M. Talarico, A.M. Arrio, A. Cornia, D. Gatteschi, and R. Sessoli. Magnetic Memory of a Single-molecule Quantum Magnet wired to a Gold Surface. *Nat. Mat.*, 8:194–197, 2009.

[147] H. Song, M.A. Reed, and T. Lee. Single Molecule Electronic Device. *Adv. Mat.*, 23:1583–1608, 2011.

[148] S. Decurtins, P. Gütlich, C.P. Köhler, H. Spiering, and A. Hauser. Light-Induced Excited Spin State Trapping in a Transition-Metal Complex: The Hexa-1-Propyltetrazole-Iron (II) Tetrafluoroborate Spin-Crossover System. *Chem. Phys. Lett.*, 105:1–4, 1984.

[149] S. Decurtins, P. Gütlich, K.M. Hasselbach, A. Hauser, and H. Spiering. Light-Induced Excited-Spin-State Trapping in Iron(II) Spin-Crossover Systems. Optical Spectroscopic and Magnetic Susceptibility Study. *Inorg. Chem.*, 24:2174–2178, 1985.

[150] P. Gütlich, V. Ksenofontov, and A.B. Gaspar. Pressure Effect Studies on Spin Crossover Systems. *Coord. Chem. Rev.*, 249:1811–1829, 2005.

[151] M. Halcrow. *Spin Crossover Materials: Properties and Applications.* Wiley and Sons, 2013.

[152] T. Tezgerevska, K.G. Alley, and C. Boskovic. Valence Tautomerism in Metal Complexes: Stimulated and Reversible Intramolecular Electron Transfer between Metal Centers and Organic Ligands. *Coord. Chem. Rev.*, 268:23–40, 2014.

[153] P. Gütlich and A. Dei. Valence Tautomeric Interconversion in Transition Metal 1,2-Benzoquinone Complexes. *Angew. Chem. Int. Ed.*, 36:2734–2736, 1997.

[154] C.G. Pierpont. Studies on Charge Distribution and Valence Tautomerism in Transition Metal Complexes of Catecholate and Semiquinonate Ligands. *Coord. Chem. Rev.*, 216-217:99–125, 2001.

[155] D.M. Adams, A. Dei, A.L. Rheingold, and D.N. Hendrickson. Controlling Valence Tautomerism of Cobalt Complexes Containing the Benzosemiquinone Anion as Ligand. *Angew. Chem. Int. Ed.*, 32:880–882, 1993.

[156] C. Carbonera, A. Dei, J.F. Létard, C. Sangregorio, and L. Sorace. Thermally and Light-Induced Valence Tautomeric Transition in a Dinuclear Cobalt-Tetraoxolene Complex. *Angew. Chem. Int. Ed.*, 43:3136–3138, 2004.

[157] J. Tao, H. Maruyama, and O. Sato. Valence Tautomeric Transitions with Thermal Hysteresis around Room Temperature and Photoinduced Effects Observed in a Cobalt-Tetraoxolene Complex. *J. Am. Chem. Soc.*, 128:1790–1791, 2006.

[158] A. Caneschi, A. Cornia, and A. Dei. Valence Tautomerism in a Cobalt Complex of a Schiff Base Diquinone Ligand. *Inorg. Chem.*, 37:3419–3421, 1998.

[159] A. Dei and L. Sorace. Cobalt-Dioxolene Redox Isomers: Potential Spintronic Devices. *Appl. Mag. Reson.*, 38:139–153, 2010.

[160] D.M. Adams, B. Li, J.D. Simon, and D.N. Hendrickson. Photoinduced Valence Tautomerism in Cobalt Complexes Containing Semiquinone Anion as Ligand: Dynamics of the High-Spin [CoII(3,5-dtbsq)$_2$] to Low-Spin

[CoIII(3,5-dtbsq)(3,5-dtbcat)] Interconversion. *Angew. Chem. Int. Ed.*, 34:1481–1483, 1995.

[161] O. Sato, S. Hayami, Z. Gu, K. Takahashi, R. Nakajima, K. Seki, and A. Fujishima. Photo-Induced Valence Tautomerism in a Co Compound. *J. Photochem. Photobiol. A:Chem.*, 149:111–114, 2002.

[162] A. Cui, K. Takahashi, A. Fujishima, and O. Sato. Mechanism and Relaxation Kinetics of Photo-Induced Valence Tautomerism of [Co(phen)(3,5-DBSQ)$_2$]·C_6H_5Cl. *J. Photochem. Photobiol. A: Chem.*, 167:69–73, 2004.

[163] O. Sato, A. Cui, R. Matsuda, J. Tao, and S. Hayami. Photo-Induced Valence Tautomerism in Co Complexes. *Acc. Chem. Res.*, 40:361–369, 2007.

[164] P. Dapporto, A. Dei, G. Poneti, and L. Sorace. Complete Direct and Reverse Optically Induced Valence Tautomeric Interconversion in a Cobalt–Dioxolene Complex. *Chem. Eur. J.*, 14:10915–10918, 2008.

[165] J. Dai, S. Kanegawa, Z. Li, S. Kang, and O. Sato. A Switchable Complex Ligand Exhibiting Photoinduced Valence Tautomerism. *Eur. J. Inorg. Chem.*, 2013:4150–4153, 2013.

[166] G. Poneti, L. Poggini, M. Mannini, B. Cortigiani, L. Sorace, E. Otero, P. Sainctavit, A. Magnani, R. Sessoli, and A. Dei. Thermal and Optical Control of Electronic States in a Single Layer of Switchable Paramagnetic Molecules. *Chem. Sci.*, 6:2268–2274, 2015.

[167] M. Goldman. Overview of Spin Temperature, Thermal Mixing and Dynamic Nuclear Polarization. *Appl. Magn. Reson.*, 34:219–226, 2008.

[168] J.P. King, P.J. Coles, and J.A. Reimer. Optical Polarization of ^{13}C Nuclei in Diamond through Nitrogen Vacancy Centers. *Phys. Rev. B*, 81:073201, 2010.

[169] A.B. Barnes, G. De Paëpe, P.C.A. van der Wel, K.N. Hu, C.G. Joo, V.S. Bajaj, M.L. Mak-Jurkauskas, J.R. Sirigiri, J. Henzfeld, R.J. Temkin, and R.J. Griffin. High-Field Dynamic Nuclear Polarization for Solid and Solution Biological NMR. *Appl. Magn. Reson.*, 34:237–263, 2008.

[170] R.G. Griffin and T.F. Prisner. High Field Dynamic Nuclear Polarization-the Renaissance. *Phys. Chem. Chem. Phys.*, 12:5737–5740, 2010.

[171] T.R. Carver and C.P. Slichter. Polarization of Nuclear Spins in Metals. *Phys. Rev.*, 92:212–214, 1953.

[172] A. Abragam and W.G. Proctor. *C.R. Acad. Sci.*, 246:2253–2256, 1958.

[173] M. Goldman and A. Landesman. Dynamic Polarization by Thermal Mixing between Two Spin Systems. *Phys. Rev.*, 132:610–620, 1963.

[174] D. Banerjee, D. Shimon, A. Feintuch, S. Vega, and D. Goldfarb. The Interplay between the Solid Effect and the Cross Effect Mechanisms in Solid State ^{13}C DNP at 95 GHz using Trityl Radicals. *J. Magn. Reson.*, 230:212–219, 2013.

[175] F. Jähnig, G. Kwiatkowski, and M. Ernst. Conceptual and Instrumental Progress in Dissolution DNP. *J. Magn. Reson.*, 264:22–29, 2016.

[176] S.E. Day, M.I. Kettunen, F.A. Gallagher, D.E. Hu, M. Lerche, J. Wolber, K. Golman, J.H. Ardenkjaer-Larsen, and K.M. Brindle. Detecting Tumor Response to Treatment using Hyperpolarized ^{13}C Magnetic Resonance Imaging and Spectroscopy. *Nat. Med.*, 11:1382–1387, 2007.

[177] S. Siddiqui, S. Kadlecek, M. Pourfathi, Y. Xin, W. Mannherz, H. Hamedani, N. Drachman, K. Ruppert, J. Clapp, and R. Rizi. The Use of Hyperpolarized Carbon-13 Magnetic Resonance for Molecular Imaging. *Adv. Drug Delivery*, 113:3–23, 2017.

[178] A.J. Rossini, A. Zagdoun, F. Hegner, M. Schwarzwälder, D. Gajan, C. Copéret, A. Lesage, and L. Emsley. Dynamic Nuclear Polarization NMR Spectroscopy of Microcrystalline Solids. *J. Am. Chem. Soc.*, 134:16899–16908, 2012.

[179] Ü Akbey and H. Oschkinat. Structural Biology Applications of Solid State MAS DNP NMR. *J. Magn. Reson.*, 269:213–224, 2016.

[180] D. Lee, E. Bouleau, P. Saint-Bonnet, S. Hediger, and G. De Paëpe. Ultra-low Temperature MAS-DNP. *J. Magn. Reson.*, 264:116–124, 2016.

[181] W.Th. Wenckebach. The Solid Effect. *Appl. Magn. Reson.*, 34:227–235, 2008.

[182] J. Wolber, F. Ellner, B. Fridlund, A. Gram, H. Jóhannesson, G. Hansson, L.H. Hansson, M.H. Lerche, S. Mansson, and R. et Al. Servin. Generating Highly Polarized Nuclear Spins in Solution Using Dynamic Nuclear Polarization. *Nucl. Instrum. Methods Phys. Res., Sect. A*, 526:173–181, 2004.

[183] D. Shimon, Y. Hovav, I. Kaminker, A. Feintuch, D. Goldfarb, and S. Vega. Simultaneous DNP Enhancements of ^{1}H and ^{13}C Nuclei: Theory and Experiments. *Phys. Chem. Chem. Phys.*, 17:11868–11883, 2015.

[184] T.J. Schmugge and C.D. Jeffries. High Dynamic Polarization of Protons. *Phys. Rev.*, 138:A1785–A1801, 1965.

[185] K. Ley, E. Müller, and K. Scheffler. Zur Unterscheidung möglicher mesomerer Grenzzustände bei Aroxylen. *Angew. Chem.*, 70:74–75, 1958.

[186] M. Abraham, M.A.H. McCausland, and F.N.H. Robinson. Dynamic Nuclear Polarization. *Phys. Rev. Lett.*, 2:449–451, 1959.

[187] B. Corzilius, L.B. Andreas, A.A. Smith, Q.Z. Ni, and R.G. Griffin. Paramagnet Induced Signal Quenching in MAS–DNP Experiments in Frozen Homogeneous Solutions. *J. Magn. Reson.*, 240:113–123, 2014.

[188] V.A. Atsarkin and A.V. Kessenikh. Dynamic Nuclear Polarization in Solids: the Birth and Development of the Many-Particle Concept. *Appl. Magn. Reson.*, 43:7–19, 2012.

[189] V.A. Atsarkin. Dynamic Nuclear Polarization: Yesterday, Today, and Tomorrow. *J. Phys.: Conf. Series*, 324:012003–012012, 2011.

[190] B.N. Provotorov. Magnetic Resonance Saturation in Crystals. *Sov. Phys.*, 14:1126–1131, 1962.

[191] M. Borghini. Spin-Temperature Model of Nuclear Dynamic Polarization using Free Radicals. *Phys. Rev. Lett.*, 20:419–421, 1968.

[192] A. Kiswandhi, B. Lama, P. Niedbalski, M. Goderya, J. Long, and L. Lumata. The Effect of Glassing Solvent Deuteration and Gd^{3+} Doping on ^{13}C DNP at 5 T. *RCS Adv.*, 6:38855–38860, 2016.

[193] W.Th. Wenckebach. Dynamic Nuclear Polarization via Thermal Mixing: Beyond the High Temperature Approximation. *J. Magn. Reson.*, 277:68–78, 2017.

[194] W.Th. Wenckebach. Spectral Diffusion and Dynamic Nuclear Polarization: Beyond the High Temperature Approximation. *J. Magn. Reson.*, 284:104–114, 2017.

[195] R.A. Wind, M.J. Duijvestijn, C. van der Lugt, A. Manenschijn, and J. Vriend. Applications of dynamic nuclear polarization in 13 C NMR in solids. *Prog. Nucl. Magn. Reson. Spectrosc.*, 17:33–67, 1985.

[196] M. Afeworki, R.A. McKay, and J. Schaefer. Selective Observation of the Interface of Heterogeneous Polycarbonate/Polystyrene Blends by Dynamic Nuclear Polarization Carbon-13 NMR Spectroscopy. *Macromolecules*, 25:4084–4091, 1992.

[197] T.V. Can, M.A. Caporini, F. Mentink-Vigier, B. Corzilius, J.J. Walish, M. Rosay, W.E. Maas, M. Baldus, S. Vega, T.M. Swager, and R.G. Griffin. Overhauser Effect in Insulating Solids. *J. Chem. Phys.*, 141:064202, 2014.

[198] J.H. Ardenkjaer-Larsen, I. Laursen, I. Leunbach, Ehnholm.G., L.G. Wistrand, J.S. Petersson, and K. Golman. EPR and DNP Properties of Certain Novel Single Electron Contrast Agents Intended for Oximetric Imaging. *J. Magn. Reson.*, 133:1–12, 1998.

[199] B. Corzilius, A.A. Smith, and R.G. Griffin. Solid Effect in Magic Angle Spinning Dynamic Nuclear Polarization. *J. Chem. Phys.*, 137:054201, 2012.

[200] A.A. Smith, B. Corzilius, A.B. Barnes, T. Maly, and R.G. Griffin. Solid Effect Dynamic Nuclear Polarization and Polarization Pathways. *J. Chem. Phys.*, 136:015201, 2012.

[201] V.K. Michaelis, B. Corzilius, A.A. Smith, and R.G. Griffin. Dynamic Nuclear Polarization of ^{17}O: Direct Polarization. *J. Phys. Chem. B*, 117:14894–14906, 2013.

[202] G.J. Gerfen, L.R. Becerra, D.A. Hall, and R.G. Griffin. High Frequency (140 GHz) Dynamic Nuclear Polarization: Polarization Transfer to a Solute in Frozen Aqueous Solution. *J. Chem. Phys.*, 102:9494, 1995.

[203] C. Song, K.N. Hu, C.G. Joo, T.M. Swager, and R.G. Griffin. TOTAPOL: A Biradical Polarizing Agent for Dynamic Nuclear Polarization Experiments in Aqueous Media. *J. Am. Chem. Soc.*, 128:11385–11390, 2006.

[204] D. Shimon, A. Feintuch, D. Goldfarb, and S. Vega. Static ^{1}H Dynamic Nuclear Polarization with the Biradical TOTAPOL: a Transition between the Solid Effect and the Cross Effect. *Phys. Chem. Chem. Phys.*, 16:6687–6699, 2014.

[205] M. Kaushik, T. Bahrenberg, V.T. Can, M.A. Caporini, R. Silvers, J. Heiliger, A.A. Smith, H. Schwalbe, R.G. Griffin, and B. Corzilius. Gd(III) and Mn(II) Complexes for Dynamic Nuclear Polarization: Small Molecular Chelate Polarizing Agents and Applications with Site-directed Spin Labeling of Proteins. *Phys. Chem. Chem. Phys.*, 18:27205–27218, 2016.

[206] S. Jannin, A. Comment, and J.J. van der Klink. Dynamic Nuclear Polarization by Thermal Mixing Under Partial Saturation. *Appl. Magn. Reson.*, 43:59–68, 2012.

[207] V.A. Atsarkin. Verification of the Spin-Spin Temperature Concept in Experiments on Saturation of Electron Paramagnetic Resonance. *Soviet. Phys.-JETP*, 1970:1012–1018, 1970.

[208] P. Schosseler, Th. Wacker, and A. Schweiger. Pulsed ELDOR Detected NMR. *Chem. Phys. Lett.*, 224:319–324, 1994.

[209] J. Granwehr and W. Köckenberger. Multidimensional Low-Power Pulse EPR under DNP Conditions. *Appl. Magn. Reson.*, 34:355–378, 2008.

[210] Y. Hovav, I. Kaminker, D. Shimon, A. Feintuch, D. Goldfarb, and S. Vega. The Electron Depolarization during Dynamic Nuclear Polarization: Measurements and Simulations. *Chem. Phys. Phys. Chem.*, 17:226–244, 2015.

[211] A. Rosso and A. De Luca. Dynamic Nuclear Polarization and the Paradox of Quantum Thermalization. *Phys. Rev. Lett.*, 115:080401–080405, 2015.

[212] Y. Hovav, A. Feintuch, and S. Vega. Theoretical Aspects of Dynamic Nuclear Polarization in the Solid State:the Solid Effect. *J. Magn. Reson.*, 207:176–189, 2010.

[213] Y. Hovav, A. Feintuch, and S. Vega. Theoretical Aspects of Dynamic Nuclear Polarization in the Solid State: The cross effect. *J. Magn. Reson.*, 214:29–41, 2012.

[214] Y. Hovav, A. Feintuch, and S. Vega. Theoretical Aspects of Dynamic Nuclear Polarization in the Solid State - Spin Temperature and Thermal Mixing. *Phys. Chem. Chem. Phys.*, 15:188–203, 2013.

[215] S.C: Serra, M. Filibian, P. Carretta, A. Rosso, and F. Tedoldi. Relevance of Electron Spin Dissipative Processes to Dynamic Nuclear Polarization via Thermal Mixing. *Phys. Chem. Chem. Phys.*, 16:753–764, 2014.

[216] C. Ramanathan. Dynamic Nuclear Polarization and Spin Diffusion in Nonconducting Solids. *Appl. Magn. Reson.*, 34:409–412, 2008.

[217] N. Bloembergen, E.M. Purcell, and R.V. Pound. Relaxation Effects in Nuclear Magnetic Resonance Absorption. *Phys. Rev. B*, 73:679–715, 1948.

[218] P.W. Anderson, B.I. Halperin, and C.M. Varma. Anomalous Low-temperature Thermal Properties of Glasses and Spin Glasses. *Philos. Magn.*, 25:1–9, 1972.

[219] W.A. Phillips. Tunneling States in Amorphous Solids. *J. Low Temp. Phys.*, 7:351–360, 1972.

[220] L.R. Narasimhan, D.W. Pack, Y.S. Bai, A. Elschner, and M.D. Fayer. Probing Organic Glasses at Low Temperature with Variable Time Scale Optical Dephasing Measurements. *Chem. Rev.*, 90:439–457, 1990.

[221] H. Maier, B.M. Kharlamov, and D. Haarer. Two-Level System Dynamics in the Long-Time Limit: A Power-Law Time Dependence. *Phys. Rev. Lett.*, 76:2085–2088, 1996.

[222] J.C. Dyre. The Glass Transition and Elastic Models of Glass-Forming Liquids. *Rev. Mod. Phys.*, 78:953–972, 2006.

[223] R. Jankowiak, G.J. Small, and K.B. Athreya. Derivation of the Density of States and Distribution Functions for Two-Level Systems in Glasses. *J. Phys. Chem.*, 90:3896–3898, 1972.

[224] W. Köhler and J. Friedrich. Distribution of Barrier Heights in Amorphous Organic Materials. *Phys. Rev. Lett.*, 59:2199–2202, 1987.

[225] S. Estalji, O. Kanert, J. Steinert, H. Jain, and K.L. Ngai. Uncommon Nuclear-Spin Relaxation in Auorozirconate Glasses at Low Temperatures. *Phys. Rev. B*, 43:7481–7486, 1991.

[226] S.K. Misra. Spin-Lattice Relaxation Times in Amorphous Materials as Effected by Exchange Interactions, Tunneling Level States (TLS) Centres, and Fractons. *Spectrochim. Acta, Part A*, 54:2257–2267, 1998.

[227] R.M. Achey, P.L. Kuhns, A.P. Reyes, W.G. Moulton, and N.S. Dalal. ^{13}C NMR and Relaxation Studies of the Nanomagnet Mn_{12}-acetate. *Phys. Rev. B*, 64:064420, 2001.

[228] P. Carretta, M. Corti, and A. Rigamonti. Spin dynamics in Cuo and $Cu_{1-x}Li_xO$ from ^{63}Cu and ^{7}Li nuclear relaxation. *Phys. Rev. B*, 48:3433–3444, 1993.

[229] M. Corti, S. Marini, A. Rigamonti, F. Tedoldi, and V. Capsoni, D. Massarotti. Spin Dynamics in Hole-Doped NiO from ^{7}Li NMR in $Ni_{1-x}Li_xO$. *Phys. Rev. B*, 56:11056–11064, 1997.

[230] M. Filibian, P. Carretta, T. Miyake, Y. Taguchi, and Y. Iwasa. Low-Energy Excitations in the Electron-Doped Metal Phthalocyanine $Li_{0.5}$MnPc from ^{7}Li and ^{1}H NMR. *Phys. Rev. B*, 75:085107–1–7, 2007.

[231] H.J. Schneider, F. Hacket, and V. Rüdiger. NMR Studies of Cyclodextrins and Cyclodextrin Complexes. *Chem. Rev.*, 98:1755–1785, 1998.

[232] S. Swaminathan, R. Cavalli, and F. Trotta. Cyclodextrin-Based Nanosponges: a Versatile Platform for Cancer Nanotherapeutics Development. *Wiley Interdiscip. Rev.: Nanomed. Nanobiotechnol.*, 8:579–601, 2016.

[233] E. Redenti, C. Pietra, A. Gerloczy, and L. Szente. Cyclodextrins in Oligonucleotide Delivery. *Adv. Drug Delivery Rev.*, 53:235–244, 2001.

[234] N. Nonaka, S.A. Farr, H. Kageyama, S. Shioda, and W.A. Banks. Delivery of Galanin-Like Peptide to the Brain: Targeting with Intranasal Delivery and Cyclodextrins. *J. Pharmac. Exp. Therapeutics*, 325:513–519, 2008.

[235] T. Yang, A. Hussain, J. Paulson, T.J. Abbruscato, and F. Ahsan. Cyclodextrins in Nasal Delivery of Low-Molecular-Weight Heparins: In Vivo and in Vitro Studies. *Pharm. Res.*, 21:1127–1136, 2004.

[236] G. Wenz, B.H. Hanh, and A. Müller. Cyclodextrin Rotaxanes and Polyrotaxanes. *Chem. Rev.*, 2006:782–817, 106.

[237] A. Harada, Y. Takashima, and H. Yamaguchi. Cyclodextrin-Based Supramolecular Polymers. *Chem. Soc. Rev.*, 38:875–882, 2009.

[238] A. Tamura and N. Yui. Threaded Macromolecules as a Versatile Framework for Biomaterials. *Chem. Commun.*, 50:13433–13446, 2014.

[239] J. Wang, Y.M. Zang, X.J. Zhang, X.J. Zhao, and Y. Liu. Light-Controlled [3]Pseudorotaxane based on Tetrasulfonated 1,5-dinaphtho-32-crown- 8 and α-Cyclodextrin. *Asian J. Org. Chem.*, 4:244–250, 2015.

[240] L. Melone, M. Petroselli, N. Pastori, and C. Punta. Functionalization of Cyclodextrins with N-Hydroxyphthalimide Moiety: A New Class of Supramolecular Pro-Oxidant Organocatalysts. *Molecules*, 20:15881–15892, 2015.

[241] X. Hou, C. Ke, and J.S. Fraser. Cooperative Capture Synthesis: yet another Playground for Copper-free Click Chemistry. *Chem. Soc. Rev*, 45:3766–3780, 2016.

[242] A. Hashidzume, H. Yamaguchi, and A. Harada. Cyclodextrin-Based Molecular Machines. *Top. Curr. Chem.*, 354:71–110, 2014.

[243] R. Namgung, M.Y. Lee, J. Kim, Y. Jang, B.H. Lee, I.S. Kim, P. Sokkar, Y.M. Rhee, A.S. Hoffman, and W.J. Kim. Poly-Cyclodextrin and Poly-Paclitaxel Nano-assembly for Anticancer Therapy. *Nat. Commun.*, 5:3702–3711, 2014.

[244] M. Sun, H.Y. Zhang, Q. Zhao, X.Y. Hu, L.H. Wang, B.W. Liu, and Y. Liu. A Supramolecular Brush Polymer via the Self-assembly of Bridged Tris(β-Cyclodextrin) with a Porphyrin Derivative and its Magnetic Resonance Imaging. *J. Mater. Chem. B*, 3:8170–8179, 2015.

[245] S. Aime, E. Gianolio, F. Uggeri, S. Tagliapietra, A. Barge, and G. Cravotto. New Paramagnetic Supramolecular Adducts for MRI Applications based on Non-Covalent Interactions Between Gd(III)-Complexes and β- or γ-Cyclodextrin Units Anchored to Chitosan. *J. Inorg. Chem.*, 100:931–938, 2006.

[246] Z. Zhou, Y. Mondjinou, S.H. Hyun, A. Kulkarni, Z.R. Lu, and D.H. Thompson. Gd^{3+} -1,4,7,10-Tetraazacyclododecane-1,4,7-triacetic-2-hydroxypropyl-β-Cyclodextrin/Pluronic Polyrotaxane as a Long Cir-

culating High Relaxivity MRI Contrast Agent. *ACS Appl. Mater. Interfaces*, 7:22272–22276, 2015.

[247] M.M. Nociari, G.L. Lehmann, A.E. Perez Bay, R.A. Radu, Z. Jiang, S. Goicochea, R. Schreiner, J.D. Warren, J. Shan, and S.A. de Beaumais et Al. Beta Cyclodextrins Bind, Stabilize, and Remove Lipofuscin Bisretinoids from Retinal Pigment Epithelium. *Proc. Natl. Acad. Sci. Early Edition*, 2014.

[248] T.S. Anirudhan, A.S. Nair, and S.S. Nair. Enzyme Coated beta-cyclodextrin for Effective Adsorption and Glucose-responsive Closed-loop Insulin Delivery. *Int. J. Biol. Macromol.*, 91:818–827, 2016.

[249] T.J. Maarup, A.H. Chen, D. Porter, N.Y. Farhat, D.S.Ory, R. Sidhud, X. Jiang, and P.I.Dickson. Intrathecal 2-hydroxypropyl-beta-cyclodextrin in a Single Patient with Niemann-Pick C1. *Mol. Gen. Metabol.*, 116:75–79, 2015.

[250] F. Masood, T. Yasin, H. Bukhari, and M. Mujahid. Characterization and Application of Roxithromycin loaded Cyclodextrin based Nanoparticles for Treatment of Multidrug Resistant Bacteria. *Mat. Sci. Eng.*, 61:1–7, 2016.

[251] F. Caracciolo, P. Carretta, M. Filibian, and L. Melone. Dynamic Nuclear Polarization of βCyclodextrin Macromolecules. *J. Phys. Chem. B*, 121:2584–2593, 2017.

[252] F. Caracciolo, A. Lucini-Paioni, M. Filibian, L. Melone, and P. Carretta. Proton and Carbon-13 Dynamic Nuclear Polarization of Methylated βCyclodextrins. *J. Phys. Chem. B*, 122:1836–1845, 2018.

[253] E. Ravera, B. Corzilius, V.K. Michaelis, C. Luchinat, R.G. Griffin, and I. Bertini. DNP-Enhanced MAS NMR of Bovine Serum Albumin Sediments and Solutions. *J. Phys. Chem. B*, 118:2957–2965, 2014.

[254] S.C. Serra, A. Rosso, and F. Tedoldi. On the Role of Electron-Nucleus Contact and Microwave Saturation in Thermal Mixing DNP. *Phys. Chem. Chem. Phys.*, 15:8416–8428, 2013.

[255] B. Vuichoud, J. Milani, A. Bornet, R. Melzi, S. Jannin, and G. Bodenhausen. Hyperpolarization of Deuterated Metabolites via Remote Cross-Polarization and Dissolution Dynamic Nuclear Polarization. *J. Phys. Chem. B*, 118:1411–1415, 2014.

[256] E. Evangelio and D.R. Molina. Valence Tautomerism: New Challenges for Electroactive Ligands. *Eur. J. Inorg. Chem.*, 0:2957–2971, 2005.

[257] B. Li, J. Tao, H.L. Sun, O. Sato, R.B. Huang, and L.S. Zheng. Side-Effect of Ancillary Ligand on Electron Transfer and Photodynamics of a Dinuclear Valence Tautomeric Complex. *Chem. Comm.*, 0:2269–2271, 2008.

[258] R.M. Buchanan and C.G. Pierpont. Tautomeric Catecholate-Semiquinone Interconversion via Metal-Ligand Electron Transfer. Structural, Spectral, and Magnetic Properties of(3,5-Di-tert-butylcatecholato)-(3,5-di-tert-butylsemiquinone)(bipyridyl)cobalt(111), a Complex Containing Mixed-Valence Organic Ligands. *Am. Chem. Soc.*, 102:4951–4957, 1980.

[259] A. Beni, A. Dei, D.A. Schultz, and L. Sorace. Ligand Design Modulates Photoinduced Properties of Cobalt-Dioxolene Valence Tautomers. *Chem. Phys. Lett.*, 428:400–404, 2006.

[260] R.D. Schmidt, D.A. Shultz, and J.A. Martin. Magnetic Bistability in a Cobalt Bis(dioxolene) Complex: Long-Lived Photoinduced Valence Tautomerism. *Inorg. Chem.*, 49:3162–3168, 2010.

[261] C. Roux, D.M. Adams, J.P. Itié, A. Polian, and D.N. Hendrickson. Pressure-Induced Valence Tautomerism in Cobalt o-Quinone Complexes: an X-ray Absorption Study of the Low-Spin [CoIII(3,5-DTBSQ)(3,5-DTBCat)(phen)] to High-Spin [CoII(3,5-DTBSQ)$_2$(phen)] Interconversion. *Inorg. Chem.*, 35:2846–2852, 1996.

[262] B. Li, F. Yang, J. Tao, O. Sato, R. Huang, and L. Zheng. The Effects of Pressure on Valence Tautomeric Transitions of Dinuclear Cobalt Complexes. *Chem. Commun.*, pages 6019–6021, 2008.

[263] G. Poneti, M. Mannini, L. Sorace, P. Sainctavit, M.A. Arrio, E. Otero, C.J. Cezar, and A. Dei. Soft-X-ray-Induced Redox Isomerism in a Cobalt Dioxolene Complex. *Angew. Chem. Int. Ed.*, 49:1954–1957, 2010.

[264] O. Jung, D.H. Jo, Y.A. Lee, B.J. Conklin, and C.G. Pierpont. Bistability and Molecular Switching for Semiquinone and Catechol Complexes of Cobalt. Studies on Redox Isomerism for the Bis(pyridine) Ether Series Co(py$_2$X)(3,6-DBQ)$_2$, X = O, S, Se, and Te. *Inorg. Chem.*, 36:19–24, 1997.

[265] S. Bin-Salamon, S. Brewer, S. Franzen, D.L. Feldheim, S. Lappi, and D.A. Shultz. Supramolecular Control of Valence-Tautomeric Equilibrium on Nanometer-Scale Gold Clusters. *J. Am. Chem. Soc.*, 127:5328–5329, 2005.

[266] J.F. Létard, P. Guionneau, and L. Goux-Capes. Towards Spin Crossover Applications. *Top. Curr. Chem.*, 235:221–249, 2004.

[267] N.A. Vazquez-Mera, F. Novio, C. Roscini, C. Bellacanzone, M. Guardingo, J. Hernando, and D. Ruiz-Molina. Switchable Colloids, Thin-Films and Interphases based on Metal Complexes with non-Innocent Ligands: the Case of Valence Tautomerism and their Applications. *J. Mater. Chem. C*, 4:5879–5889, 2016.

[268] A. Beni, A. Dei, R. Laschi, M. Rizzitano, and L. Sorace. Tuning the Charge Distribution and Photoswitchable Properties of Cobalt–Dioxolene Complexes by Using Molecular Techniques. *Chem. Eur. J.*, 14:1804–1813, 2008.

[269] T. Tayagaki, A. Galet, G. Molnár, M.C. Mũnoz, A. Zwick, K. Tanaka, J.A. Real, and A. Bousseksou. Metal Dilution Effects on the Spin-Crossover Properties of the Three-Dimensional Coordination Polymer Fe(pyrazine)[$Pt(CN)_4$]. *J. Phys. Chem. B*, 109:14859–14867, 2005.

[270] F.V.R. Neuwahl, R. Righini, and A. Dei. Femtosecond Spectroscopic Characterisation of the Two-step Valence Tautomeric Interconversion occurring in a Cobalt-dioxolene Complex. *Chem. Phys. Let.*, 6:408–414, 2002.

[271] P.L. Gentili, L. Bussotti, R. Righini, A. Beni, L. Bogani, and A. Dei. Time-resolved Spectroscopic Characterization of Photo-induced Valence Tautomerism in a Cobalt-dioxolene Complex. *Chem. Phys.*, 314:9–17, 2005.

[272] A. Beni, A. Dei, M. Rizzitano, and L. Sorace. Unprecedented Optically Induced Long-lived Intramolecular Electron Transfer in Cobalt-dioxolene Complexes. *Chem. Commun.*, pages 2160–2162, 2007.

[273] D.M. Adams, L Noodleman, and D.N. Hendrickson. Density Functional Study of the Valence-Tautomeric Interconversion Low-Spin [Co^{III}(SQ)(Cat)(phen)] - High-Spin [$Co^{II}(SQ)_2$(phen)]. *Inorg. Chem.*, 36:3966–3984, 2011.

[274] A.G. Starikov, R.M. Minyaev, A.A. Starikova, and V.I. Minkin. Valence Tautomeric Complexes of Cobalt Diketonates with Diimines: A Quantum-Chemical Study. *Doklady Chem.*, 440:289–293, 2011.

[275] D. Sato, Y. Shiota, G. Juhász, and K. Yoshizawa. Theoretical Study of the Mechanism of Valence Tautomerism in Cobalt Complexes. *J. Phys. Chem.*, 114:12928–12935, 2010.

[276] A. Bencini, A. Caneschi, C. Carbonera, A. Dei, D. Gatteschi, R. Righini, C. Sangregorio, and J. Van Slagerov. Tuning the Physical Properties of a Metal Complex by Molecular Techniques: the Design and the Synthesis of the simplest Cobalt-o-dioxolene Complex undergoing Valence Tautomerism. *J. Mol. Struct.*, 656:141–154, 2003.

[277] P. Carretta, N. Papinutto, R. Melzi, P. Millet, S. Gonthier, P. Mendels, and P. Wzietek. Magnetic Properties of Frustrated Two-dimensional S=$\frac{1}{2}$ Antiferromagnets on a Square Lattice. *J. Phys.: Condens. Matter*, 16:S849–S856, 2004.

[278] F. Branzoli, M. Filibian, P. Carretta, S. Klyatskaya, and M. Ruben. Spin Dynamics in the Neutral Rare-earth Single-molecule Magnets $[TbPc_2]^0$ and $[DyPc_2]^0$ from μSR and NMR Spectroscopies. *Phys. Rev. B*, 79:220404–1–4, 2009.

[279] S.J. Blundell, F.L. Pratt, C.A. Steer, I.M. Marshall, and J.F. Létard. A μSR Study of the Spin-Crossover. *J. Phys. Chem. Sol.*, 65:25–28, 2004.

[280] D. E. Murnick, A. T. Fiory, and W. J. Kossler. Muon-Spin Depolarization in Spin-Glasses. *Phys. Rev. Lett.*, 36:100–104, 1976.

[281] I.A. Campbell, A. Amato, F.N. Gygax, D. Herlach, A. Schenck, R. Cywinski, and S.H. Kilcoyne. Dynamics in Canonical Spin Glasses Observed by Muon Spin Depolarization. *Phys. Rev. Lett.*, 72:1291–1294, 1994.

[282] J. Kishine, T. Watanabe, H. Deguchi, M. Mito, T. Sakai, T. Tajiri, M. Yamashita, and H. Miyasaka. Spin Correlation and Relaxational Dynamics in Molecular-based Single-chain Magnets. *Phys. Rev. B*, 74:224419, 2006.

[283] F. Borsa, Y. Furukawa, and A. Lascialfari. Review of NMR and μSR Studies in the Molecular Nanomagnet Mn12-ac. *Inorg. Chim. Acta*, 361:3777–3784, 2008.

[284] Z. Salman, R.F. Kiefl, K.H. Chow, W.A. MacFarlane, T.A. Keeler, T.J. Parolin, S. Tabbara, and D. Wang. Persistent Spin Dynamics in the S=1/2 V_{15} Molecular Nanomagnet. *Phys. Rev. B*, 77:214415, 2008.

[285] B.Z. Malkin, M.V. Vanyunin, M.J. Graf, J. Lago, F. Borsa, A. Lascialfari, A.M. Tkachuk, and B. Barbara. ^{19}F Nuclear Spin Relaxation and Spin Diffusion Effects in the Single-ion Magnet $LiYF_4$: Ho^{3+}. *Eur. Phys. J. B*, 66:155–163, 2008.

[286] R. Nath, A.A. Tsirlin, P. Kunthia, O. Janson, T. Förster, M. Padmanabhan, J. Li, Yu. Skourski, M. Baenitz, and H. Rosner. Magnetization and Spin Dynamics of the Spin S=1/2 hourglass nanomagnet $Cu_5(OH)_2(NIPA)_4{\cdot}10H_2O$. *Phys. Rev. B*, 87:214417, 2013.

[287] A. Henstra, L.J. Schmidt, and W.T. Wenckebach. High Dynamic Nuclear Polarization at Room Temperature. *Chem. Phys. Lett.*, 165:6–10, 1990.

[288] A. Mele, F. Castiglione, L. Malpezzi, F. Ganazzoli, G. Raffaini, F. Trotta, B. Rossi, A. Fontana, and G. Giunchi. HR MAS NMR, Powder

XRD and Raman Spectroscopy Study of Inclusion Phenomena in βCD Nanosponges. *J. Incl. Phenom. Macrocycl. Chem.*, 69:403–409, 2011.

[289] M. Ferro, F. Castiglione, C. Punta, L. Melone, W. Panzeri, B. Rossi, F. Trotta, and A. Mele. Anomalous Diffusion of Ibuprofen in Cyclodextrin Nanosponge Hydrogels: an HRMAS NMR Study. *Beilstein J. Org. Chem.*, 10:2715–2723, 2014.

[290] M. Ferro, F. Castiglione, C. Punta, L. Melone, W. Panzeri, and B. Rossi. Transport Properties of Ibuprofen Encapsulated in Cyclodextrin Nanosponge Hydrogels: A Proton HR-MAS NMR Spectroscopy Study. *J. Vis. Exp.*, 114:53769, 2016.

List of publications

- Filippo Caracciolo, Marta Filibian, Pietro Carretta, Alberto Rosso, Andrea De Luca, "Evidence of Spin-Temperature in Dynamic Nuclear Polarization: an exact Computation of the EPR Spectrum", Phys. Chem. Chem. Phys., **18**, 2016, 25655-25662

- Filippo Caracciolo, Pietro Carretta, Marta Filibian, Lucio Melone, "Dynamic Nuclear Polarization of β-Cyclodextrin Macromolecules", J. Phys. Chem. B, **121**, 2017, 2584-2593

- Filippo Caracciolo, Alessandra Lucini Paioni, Marta Filibian, Lucio Melone, Pietro Carretta, "Proton and Carbon-13 Dynamic Nuclear Polarization of Methylated β-Cyclodextrins", J. Phys. Chem. B, **122**, 2018, 1836-1845

- Filippo Caracciolo, Matteo Mannini, Giordano Poneti, Matej Pregelj, Nejc Janša, Denis Arčon, and Pietro Carretta, "Spin Fluctuations in the Light-induced High-spin State of Cobalt Valence Tautomers", Phys. Rev. B, **98**, 2018, 054416

Acknowledgements

I would like to thank my supervisor Professor Pietro Carretta who gave me the opportunity to explore the interesting and stimulating world of magnetism under light irradiation and who guided me with precious suggestions. Special thanks go to my colleagues of the NMR group at the Department of Physics at the University of Pavia, Matteo Moroni, Manuel Mariani, Maurizio Corti, Giacomo Prando, Alessandro Lascialfari, Marta Filibian and Marco Moscardini. I am also grateful to Professor Alberto Rosso and Andrea De Luca and to Professor Denis Arčon and Matej Pregelj for helping and guiding me during my stay in Paris and Ljubljana, respectively. Also thanks to Professor Arnaud Comment and Professor Fabrice Bert for carefully reading the thesis. Last, but not the least, I would like to thank my family, all my friends and my girlfriend who all supported me during the PhD in Pavia.